The International Journal of Advanced Manufacturing Technology (2021) 116:2045–2092
https://doi.org/10.1007/s00170-021-07558-6

CRITICAL REVIEW

Cutting edge microgeometries in metal cutting: a review

Kejia Zhuang[1] · Changni Fu[1] · Jian Weng[1] · Cheng Hu[1]

Received: 23 March 2021 / Accepted: 27 June 2021 / Published online: 8 July 2021

Abstract
For decades, attentions have been paid to metal cutting processes, especially for the critical components in aerospace, marine, medical industries, etc. Scholars investigated the influence of cutting parameters, tool geometry, lubricant, pursuing a deeper understanding of process signatures, better tool performance, and more superior surface integrity. Edge microgeometry is proved to be an essential factor that significantly influences the tool-workpiece-chip contact, plastic deformation, and heat generation, which in turn affects the cutting phenomena.

This paper aims to provide an insight and scientific overview of the role of edge microgeometries in metal cutting, with special attention on material flow state, cutting mechanics, tool performance, as well as the surface integrity. The characterization of edge microgeometries includes edge types (honed, chamfered, mixed), size parameters (edge radius, form-factor *K*, chamfer angle, chamfer length), and edge preparation techniques (grinding, drag finishing, brushing, micro-blasting, etc.). The researches on the influence of edge microgeometries on material flow state and cutting mechanics are reviewed, mainly focusing on analytical modeling and finite element method to explain how the edge microgeometries affect cutting processes. Then, the researches on the influence of edge microgeometries on tool performance and surface integrity are well organized to present the various findings in these topics. From the current perspective, many scholars have noticed the importance of edge microgeometries in metal cutting and have done numerous researches on this topic. Summary and future suggestions are given based on their state-of-the-art contributions in the last section.

Keyword Edge microgeometries · Material flow · Cutting mechanics · Tool performance · Surface integrity

1 Introduction

1.1 Researches on metal cutting

The machining methods (e.g., turning, milling, drilling, tapping, etc.) still take an important role in the material removal process. The machining parameters as well as the tool path directly depend on the cutting tool which also have an influence on the functional performance of the machined surface. Most of the literature in this research area focused on three aspects, shown in Fig. 1.

From the first aspect, super hard materials are often chosen for tool production, including carbide, CBN, PCBN, etc. Recently, ceramic tools also become more and more popular for its superior resistance to wear, high temperature, and oxidation. Tool design represents the basic shape, cutting angels, nose radius, chip breaker, etc., which can be concluded as macrogeometry of tools. Grinding, drag finishing, brushing, and magneto abrasive machining are the edge preparation techniques depending on the friction between the abrasive particles and the tool edge surface. Abrasive particles with high speed are used to form the edge geometry, i.e. abrasive jet machining, abrasive flow machining, wide peening cleaning, and vibration machining. Moreover, electronic-chemical, electronic discharge, and laser are corrosion treatment for edge preparation. Coating is the last step in tool production, which can improve the wear resistance of cutting tool and prolong the tool life in service. The material, hardness, layers, properties, and thickness of coatings are the key features that affect the tool performance. At the beginning, the coating method used in cutting tools was used to reduce the abrasion and adhesion wear and improve tool life [1]. With the rapid development of cutting technology, the

✉ Jian Weng
weng_jian@outlook.com

[1] Hubei Digital Manufacturing Key Laboratory, School of Mechanical and Electronic Engineering, Wuhan University of Technology, Wuhan 430070, China

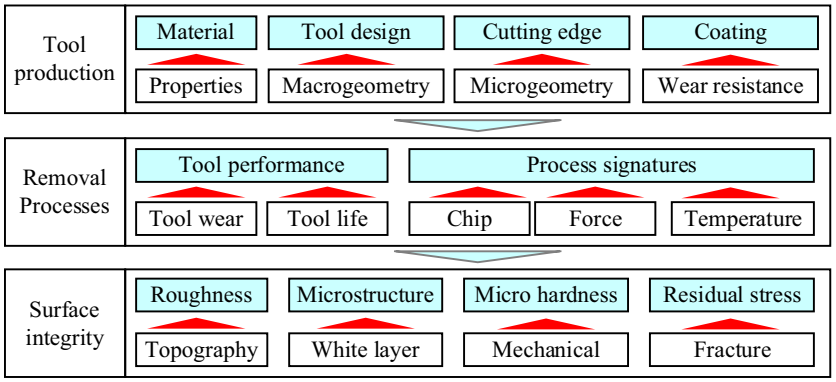

Fig. 1 Main research fields on the cutting tool

thermal-mechanical loads on tool is getting larger and larger. Then, the high temperature coatings which can withstand mechanical and thermal loads are used to protect the tool from the cycle loads in cutting operations.

The second aspect associated with cutting tool is material removal processes where tool performance and process signatures are two important indicators. Tool performance can be determined by the tool wear mechanism and tool life in the cutting process. The tool wear mechanism can be determined by the tool material, coatings, tool macrogeometries and microgeometries, as well as the cutting conditions. The tool life is an essential indicator when evaluating tool performance of cutting tool and machinability of workpiece. Another characteristic in this aspect is the process signature that can be considered as the intermediate process variable that connects the input parameters and the generated machined surface during metal cutting operations [2]. The chip formation, cutting force, and cutting temperature are the typical process signatures and should be described by more physical-based approaches [3]. The missing link between the materials reacts and the process signatures should be detailed analyzed based on the predicted method.

The third aspect that should be mentioned is the surface integrity of the machined surface. The machining-induced surface integrity is a critical field that affects the functional performance of components [4]. The surface layer of component suffers from cycle thermal-mechanical loads and serve plastic deformation, leading to the modifications of properties and microstructure in near-surface area.

Among all the features of tool production, the shape and quality of cutting edge microgeometries make significant difference to the metal cutting processes because it is the major tool-workpiece contact area. The thermal-mechanical loads in contact area generated from deformation zones have obvious effects on tool performance, chip formation, and surface integrity. In recent years, cutting tools with different micro edge geometries get more and more attentions from scholars and industries.

1.2 Types of cutting edge

Usually, there are eight types of edge design, specified in Fig.2. The sharp edge (Fig. 2a) is the original design mostly used in early times. However, the ensuing edge chipping problem stops it from extensive use on hard materials, such as Nickel-based alloys or stainless steel. Therefore, the chamfered edge (Fig. 2b) prevails for its superior impact resistance. This is because some workpiece material is stably trapped

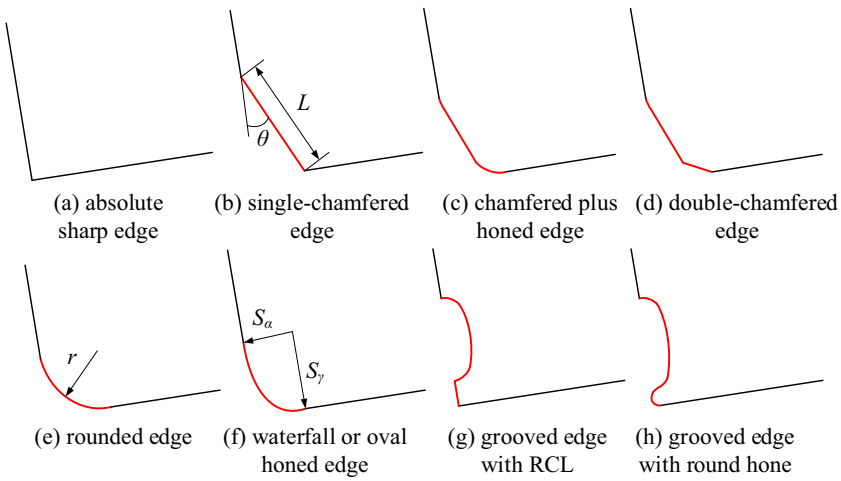

Fig. 2 Schematics of the eight available types of tool edge. **a** Absolute sharp edge. **b** Single-chamfered edge. **c** Chamfered plus honed edge. **d** Double-chamfered edge. **e** Rounded edge. **f** Waterfall or oval honed edge. **g** Grooved edge with RCL. **h** Grooved edge with round hone

adjacent to the chamfer region, protecting the tool tip by acting as a new cutting edge affront. Such a region is recognized as dead metal zone (DMZ) or stagnation zone. Meanwhile, the formed DMZ accounts for the certain increase of resultant cutting force, especially the thrust force component. The chamfer plus honed edge in Fig. 2c and double-chamfered edge in Fig. 2d are two the improved versions of the single-chamfered edge. The additionally introduced round or chamfered hone aims at enhancing the ploughing effect of the material flowing underneath. What is more, there have been studies confirming that larger compressive residual stress and better surface integrity can be obtained [5]. This could be explained by the finding that larger honed edge radius promotes stronger ploughing effect. However, the compressive stress can transform into tensile residual stress if the hone radius is improperly chosen, i.e., too large. In addition, the side-spread effect would be exacerbated and cause server burr formation. The double-chamfered edge in Fig. 2d is used to reduce the flank wear because high temperature is always found at the interface between round-hone and machined surface [6]. To facilitate the chip flow upon rake face, the round honed edge in Fig. 2e is sometimes diverted into waterfall honed edge (or oval honed edge) as illustrated in Fig. 2f. The grooved edge in Fig. 2g is usually seen on RCL tool, which makes it easier to produce segment chip due to the presence of groove. This is because the chip will hit the groove vertex due to the chip back-flow effect. Besides, the cutting temperature will decrease since the chip-contact length is substantially shortened. Nowadays, the restricted contact interface has been modified into honed edge, aiming to obtain better surface quality and lower cutting temperature. Hence, such RCL grooved edge tool has found extensive application in high-performance machining of difficult-to-cut alloys.

Figure 3 illustrates the macro and micro geometries, with the rounded and chamfered edge scanned by optical 3D microscope. The cutting edge microgeometry and parameters is defined as the edge characteristics, whereas the macrogeometry and parameters of tools illustrate the tool shape as shown in Fig. 3a. The macrogeometry of the cutting inserts can be treated as constant in manufacturing process while the microgeometry of the cutting edge is the contact area that remove the material from the bulk. The microgeometry connects the rake face and the flank face of the tool, which is the main area that leads to the plastic deformation of the material. Thus, the microgeometry of cutting edge can be considered as the decisive factor that influence the cutting performance in cutting operations [10, 11]. Research on the geometric features of tool micro edges has great significance in the development of high-performance cutting. Although there are numerous types of edge microgeometries, honed and chamfered edge are two most popular microgeometries of cutting edge, widely investigated by analytical modeling, simulations, and experiments [12–14].

The sharped edge is an ideal shape of cutting edge, which cannot be produced in actual production [16]. Also, this kind of geometry has low performance in cutting operations for it is vulnerable to tool wear and its short tool life [15, 17]. As shown in Fig. 4a, the honed edge geometry is a typical microgeometry that can enhance the tool performance, whereas some parameters are needed to constrain the complex geometry. S_α and S_γ are the cutting edge segment on flank face and rake face, respectively, which can be used to characterize the edge rounding. K is the form factor, which can be used to give a detailed analysis of the cutting edge geometry. The rounded edge can be considered as symmetrical with K = 1; otherwise, the cutting edge is asymmetrical honed edge. Δr is the profile flattening and φ is the apex angle. In some cutting conditions, the asymmetrical edge geometry has been proved to be superior to the symmetrical edge geometry [18]. However, the production of irregular

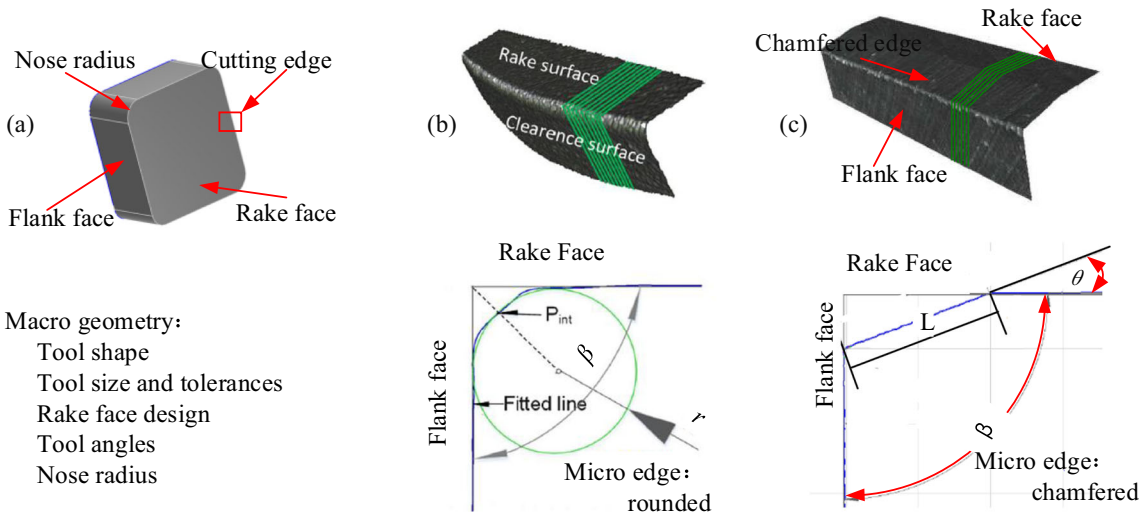

Fig. 3 Macro and micro geometries of cutting inserts, **a** macrogeometry of cutting inserts, **b** rounded edge, and **c** chamfered edge [7–9]

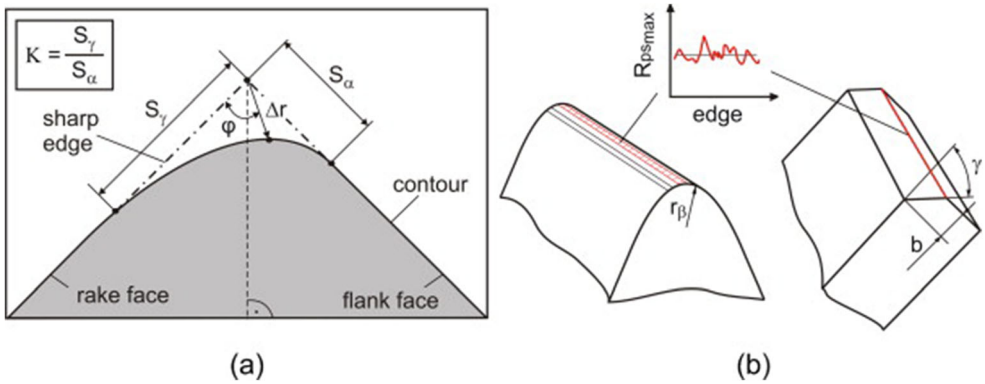

Fig. 4 Edge preparations: **a** general honed edge; **b** edge chipping [15]

edge geometry always causes a large value of $Rps_{\max}$ (an indicator of edge chipping), limiting the reliability and consistency of the tools in manufacturing process. The curvilinear edge including round and oval-like edge uses the separation point to control the edge shape. The number of those discrete control points directly determines the accuracy of the regression line, which limits the stabilization of the edge. Thus, the suitable edge shape for metal cutting with low thermal-mechanical loads and high surface integrity is still a complicated topic for academia and industries.

The other typical shape used in edge preparation is chamfered edge. The shape of a chamfered edge is relatively simple compared with honed edge. For single chamfered edge, chamfer length L and chamfer angle θ can be used to characterize the shape of this geometry. Tools with negative chamfered edge are widely used when machining difficult-to-cut materials because this kind of edge can strengthen the cutting tools [19–21]. This kind of cutting tool is often applied for rough machining due to its high mechanical properties and good wear resistance [22]. In manufacturing industry, the combination of various forms of micro cutting edge geometry has often been used to improve the tool performance and enhance the surface integrity of machined components.

1.3 Review objective

This paper aims to understand the role of edge microgeometries in metal cutting. Different machining processes pursue different goals. The rough and semi-finishing machining methods pursue longer tool life, while finish machining methods require higher machining-induced part quality. Thus, this review chooses tool performance and surface quality (the industry-relevant indicators) as the objective and tries to give an overview of how the edge microgeometries influence these two indicators. Already, it is widely recognized that the influence of edge microgeometries on tool wear and surface integrity is very significant. In order to give an in-depth understanding of this phenomenon, a discussion on cutting force and temperature caused by various edge microgeometries is required. Moreover, how the edge microgeometries affect cutting force and temperature depends on revealing the material flow state induced by edge microgeometries. Thus, the content of this review is determined, covering material flow state, cutting mechanics, tool performance, and surface integrity. The arrangement of this review is concluded in Fig. 5.

2 Material flow state

Detailed knowledge of the material deformation mechanism in machining operation is required to illustrate the generation of thermal-mechanical loads on tool and workpiece, which could give an in-depth and comprehensive view of material removal process. The material flow state is deeply affected by the tool edge microgeometries because uncut chip thickness (UCT) is in the same magnitude as the edge microgeometry, especially in finishing and micromachining. From this point of view, effective rake angle plays a dominant role in metal cutting processes. For honed edge, effective rake angle can be different at arbitrary positions along cutting edge. While for chamfered edge, effective rake angle is a sum of the edge chamfer rake angle and insert inclination in the tool holder. Slip-line field is widely accepted to be the most prevailing method to reveal the material flow state in machining, giving an in-depth understanding of shearing deformation, DMZ, and minimum uncut chip thickness (MUCT). In slip-line theory, the workpiece is considered as ideal rigid-plastic material, i.e., strain hardening, creep behavior, velocity, inertia force, and thermal stress are all neglected. Thus the stable continuous plastic deformation can be simplified as a static problem. Numerous solutions of slip-line field have been proposed over the past decades considering different types of edge microgeometries. Here, this review pays special attention to the slip-line modeling for sharp, honed, and chamfered tools and give a development path for each kind of the models.

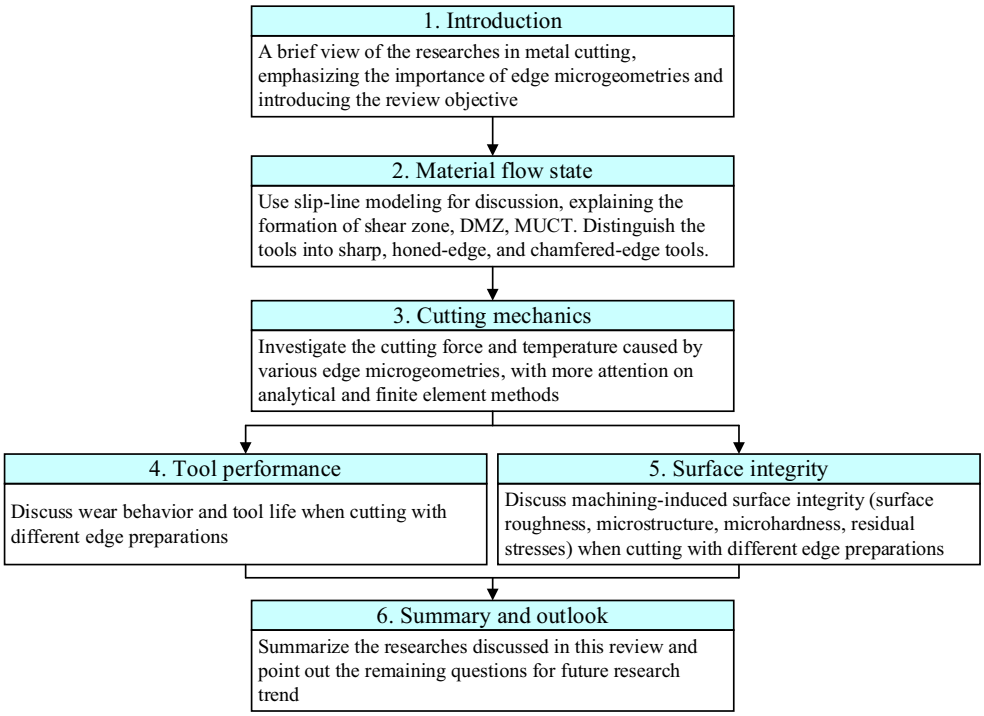

Fig. 5 The framework of this review

2.1 Sharp tool

Slip-line field models for tool sharp edge are the fundamentals for later work on the tool with complex edge geometries, like honed edge and chamfered edge. And among these, the part of uniform slip-line field models is the original inspiration. As collected in Fig. 6, the uniform slip-line field models focus on simplified characterizations of primary and secondary deformation zones. Various expressions of shear angle were developed following the single-shear-plane slip-line field model (in Fig. 6a) proposed by Merchant [23]. In their model, shear angle φ was defined to achieve minimum cutting energy consumption. The variables β and γ stand for the friction angle and rake angle, respectively. In 1951, Lee [24] extended the single-shear-plane model by adding the secondary deformation zone as shown in Fig. 6b. Later, they took into account the formation of built-up edge (BUE) on tool rake face, and developed a new one by introducing a fan area *ACD* as shown in Fig. 6c. The triangular shape region *CDB* is treated as BUE. However, results from high-speed machining (HSM) experiments reveal that no BUE is formed. This

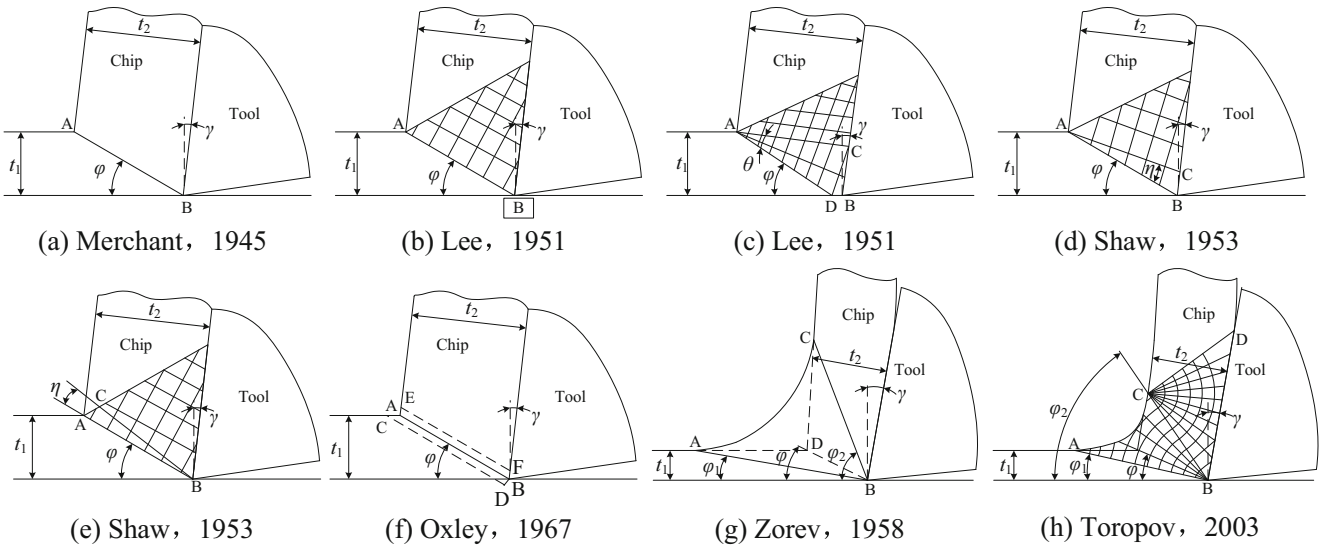

Fig. 6 Uniform slip-line field models for sharp edge tool. **a** Merchant 1945. **b** Lee 1951. **c** Lee 1951. **d** Shaw 1953. **e** Shaw 1953. **f** Oxley 1967. **g** Zorev 1958. **h** Toropov 2003

phenomenon indicates that the assumption of persistence of BUE in all cutting conditions seems inappropriate.

Then in 1953, Shaw et al. [25] brought forward the view that β slip-lines in secondary deformation zone should not be parallel with the shear plane, considering the resulted constraint from tool rake face and rigid area ahead of the shear plane. As a result, the direction of maximum shear stress and maximum shear strain may not coincide with each other. Therefore, a deflection angle (η) should exist between the actual shear plane (primary deformation zone) and theoretical shear plane (β slip-lines). The deflection of this angle is anti-clock-wise and clock-wise in Fig. 6 d and e, respectively. However, the formulation to compute this deflection angle is not specified in the study.

The slip-line field model illustrated in Fig. 6f was proposed by Oxley and Welsh [26] in 1967. With the strain hardening effect, the shear deformation is believed to take place within a shear band with certain thickness. This model is recognized as an improved version of Merchant's single-shear-plane model. In addition, they developed a new expression (see Fig. 6f) for shear angle, which was believed applicable in both low and high speed cutting conditions. Nevertheless, the expression turns out to be less convenient since unknown shear angle appears on both sides of the equation. Though Oxley's theory seems defective, one shall still admit that the concept of shear band concerning strain hardening was proposed for the first time. And it has inspired successors' researches.

It can be noticed from Fig. 6a–f that the intersection between workpiece with chip flow is simplified as a single point. Such assumption differs from the observations from both cutting experiments and FE simulations. In fact, there exists a transition zone, which is named as pre-flow region or material pile-up region by researchers. In 1958, Zorev [27] attempted to rebuild the primary deformation zone with this region concerned. Thus in Fig. 6g, the external boundary of the primary deformation zone is revised into a curvilinear line. An imaginary point of intersection (point D), defined by the extension of those two related boundaries, is introduced to determine the shear angle. Different from Oxley's parallel-sided shear band model, here the primary shear zone is supposed to narrow down to the tool tip in the end.

Inspired by Zorev's work [27], Toropov and Ko [28] extended it in 2003 by incorporating the secondary deformation zone. As depicted in Fig. 6h, a double-sector slip-line field model is developed to calculate the chip-tool contact length. However, the secondary deformation zone is simplified as an isosceles right triangle and the predicted results did not match well with the experimental observations.

In addition to the uniform slip-line fields, some non-uniform slip-line field models have also been proposed for sharp edge tool. This might be related to the finding that distributions of stress and stains during cutting process are extremely non-linear, especially in the primary deformation zone. Among them, some representative models are selected as exhibited in Fig. 7.

Based on previous work, Kudo [29] announced some possible slip-line field geometries by analyzing the movements and displacements in orthogonal cutting. As given in Fig. 7a–c, he first developed three slip-line field models for cutting with zero rake angle.

In Fig. 7a, the primary deformation zone is treated as the single curved surface with a convex one upside and concave

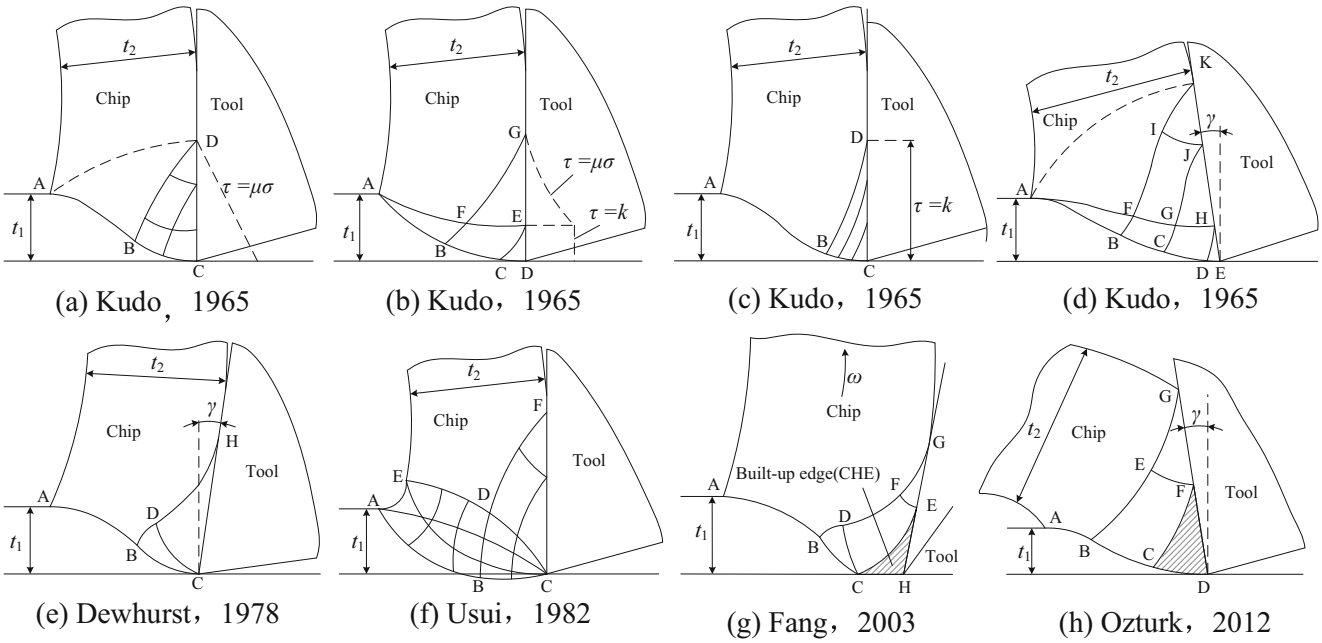

Fig. 7 Non-uniform slip-line field for sharp edge tool. **a** Kudo 1965. **b** Kudo 1965. **c** Kudo 1965. **d** Kudo 1965. **e** Dewhurst 1978. **f** Usui 1982. **g** Fang 2003. **h** Oztur 2012

one downside. Shear stress τ is assumed maximum at tool tip and then decreases linearly to zero at the detaching point (*D*).

In Fig. 7b, a triangular region *EDC* is introduced as the BUE. Besides, primary shear zone was revised as a triangular region enclosed by two intersected concave sides (*AC* and *AE*). The secondary deformation zone (*GFE*) is enclosed by a concave side (*GF*) and tool rake face. The shear stress along the chip-tool contact length is assumed constant at the BUE and decreasing at the left part (*GE*). This pattern is later adopted by many other researchers as the dual-zone contact pattern, i.e., sticking and sling contact. Considering the fact that BUE may disappear in HSM while DMZ permanently exists, Kudo [29] revised it with the formation of DMZ as given in Fig. 7c. And the sticking contact stress is still assumed uniformly distributed at the DMZ-tool interface.

Later Kudo [29] applied the slip-line field model in negative-rake-angle cutting as suggested in Fig. 7d. The model for rake-angle-cutting is not included in the figure for it is very similar to that shown in Fig. 7a. However, the model for cutting with a negative rake angle (in Fig. 7e) is much more different. It can be observed that the pattern of combined convex surface and concave surface is applied to the secondary deformation zone. The shape of primary deformation zone remains the same as that in Fig. 7b. The formed BUE marked by *HDE* is included as well.

In 1978, Dewhurst [30] developed a new slip-line field model as shown in Fig. 7e. The primary deformation zone in this model is the same as Kudo's in Fig. 7a, but two main differences can be found. One is that the boundary of secondary deformation zone is estimated in concave form in Dewhurst's model while convex form in Kudo's model. The other is the tool tip is recognized as a point of stress singularity. Therefore, an additional fan-shaped transition region *CBD* is introduced in the new model. Both Kudo and Dewhurst's models are built on the hypothesis of ideal rigid-plastic deformation. Under such plane strain circumstances, continuous chip can be formed, and the stress distribution along chip-contact length abides by the Coulomb friction law. However, the assumed steady-state slip-line field in Dewhurst's model only holds with specific initial accumulation of deformation at the beginning of cutting process. Thus he inferred that there could be several solutions with regard to the one specific cutting condition. This is later concluded as the non-unique solution theory, which helps to perfect the methodology of Dewhurst-Collins matrix operators.

The slip-line field model in Fig. 7f is proposed by Usui [31] based on visioplasticity method in 1982. The method supposes that the directions of maximum shear stress and maximum shear strain velocity coincide in the whole plastic deformation zone. In this way, by directly measuring the deformations of the coordinates mesh drawn on the plane plastic flow surface in advance, the direction of the increment of maximum shear strain velocity can be determined. Then connect all the determined points, the final slip-line field model concerning strain hardening effect is attained. In Fig. 7f, the upper and nether boundaries are separately treated as in convex and concave form. The boundary of secondary deformation zone is similar to that in Kudo's model (see Fig. 7d).

The schematic view in Fig. 7g is the integrated model proposed by Fang and Dewhurst [32] in 2005, based mainly on two previous models, i.e., Lee's in Fig. 7c and Dewhurst's in Fig. 7e. These two basic models characterize the BUE formation ahead of tool edge and stress singularity at tool tip, respectively. Therefore, Fang combined these two characteristics into one model. It should be noted that the singularity is now assumed at the left endpoint. This model is numerically constructed and solved by the Dewhurst-Collins's Matrix Operators.

According to the Dewhurst's methodology using matrix operators, Ozturk [33] in 2012 deduced a new slip-line field model for cutting with negative rake angle given in Fig. 7h. Compared with previous models, the primary deformation zone keeps the same inverse S shape pattern marked by curve *ABCD*. The triangular region *GEBCDF* enclosed by concave line and tool rake face, is taken as the secondary deformation zone, where the formed DMZ (region *DFC*) is also included. The authors indicated that the size of DMZ would increase with the increase of negative rake angle (in absolute value).

In general, the adoption of non-uniform slip-line field geometry makes it more realistic to model the machining process, especially in the primary deformation zone. By means of numerical methodologies like Cauchy-Riemann conditions and Dewhurst-Collins Matrix, the single shear plane model and shear angle become dispensable under such circumstances. On the contrary, there have been two kinds of models with respect to the rigid-plastic boundaries in the secondary deformation zone, i.e., in concave kind and convex kind. This problem should be further investigated according to specific cutting conditions including tool-workpiece combination, tool rake angle and cutting speeds, etc.

2.2 Honed-edge tool

To be exact, the edges of all tools should be treated as honed since no tool edge could be produced absolutely sharp. In spite of this fact, the sharp edged tool can still be regarded as absolutely sharp unless the UCT becomes comparable with the tool hone edge radius. Nevertheless, with the broad application of micro cutting, finishing process, and high-precision machining (HPM), the effect of tool honed edge on cutting mechanisms has intrigued the researchers around the world. Moreover, when honed-edge is considered, MUCT is introduced as well. The initial concept of MUCT is defined whether a chip is formed or not [34]. From this perspective, MUCT can be considered as a critical depth of cut and undoubtedly increase with the growth of

edge radius [35, 36]. However, later scholars extended its definition to continuously cutting process that materials above MUCT become chip while materials under MUCT become part of the machined surface [37]. From this perspective, the value of MUCT can be determined by the height of stagnation point or the height of the bottom point of DMZ, which can be observed in slip-line fields [38, 39].

Here in Fig. 8, the representative and fundamental models are collected. Generally speaking, the investigation on honed edge starts in the grinding process field where UCT is usually rather small. Thus in 1974, Abdelmoneim and Scrutton [38] carried out a study on the material removal in grinding. As elaborated in Fig. 8a, an analytical cutting model concerning the formation of DMZ is developed with regard to the tool

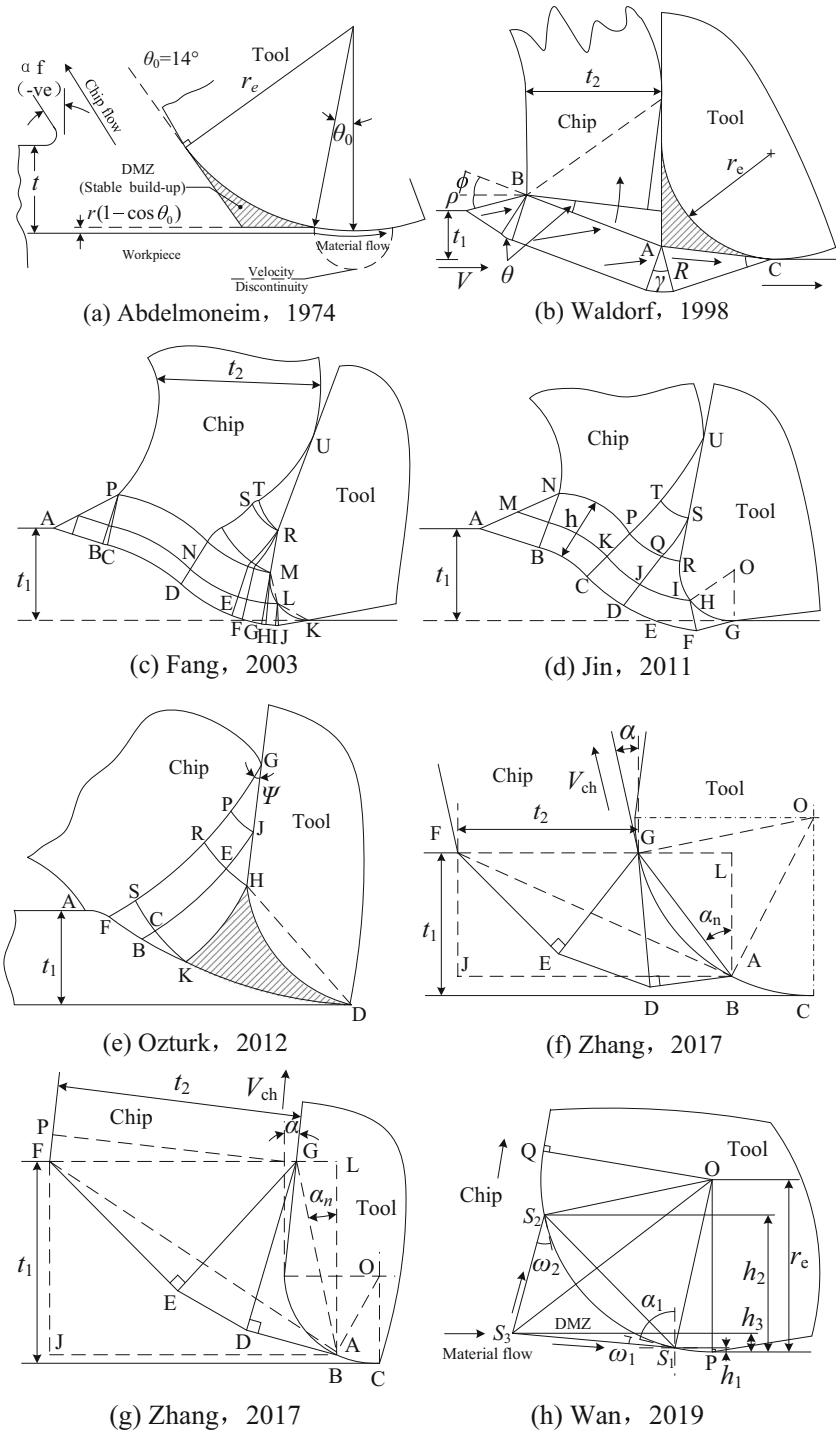

Fig. 8 Slip-line field models for hone edge tool. **a** Abdelmoneim 1974. **b** Waldorf 1998. **c** Fang 2003. **d** Jin 2011. **e** Ozturk 2012. **f** Zhang 2017. **g** Zhang 2017. **h** Wan 2019

edge rounding. Based on this model, they deduced the expressions for specific cutting energy with UCT.

Later in 1998, Waldorf et al. [40] extended Abdelmoeim's model into orthogonal turning process. As shown in Fig. 8b, they proposed a novel model for honed edge tool based on slip-line field approach. The DMZ in a shaded triangle is incorporated and acts as a rigid stable cutting edge dividing the material flow. The material flowing above DMZ is deformed into chip by shearing while that flowing beneath is ploughed into the machined surface. Therefore, the plough force and shear force components can be separately determined. What is more, the pre-flow region is included as well, serving as part of the primary shear band. Waldorf's model witnessed the very first application of slip-line field theory to turning with honed edge tool.

In view of the material separation phenomenon ahead of honed edge, Fang and Jawahir [41] developed a slip-line model for tools with honed edge as illustrated in Fig. 8c. In this model, 27 in total sub-regions are included considering the points of singularity at honed edge face (*KM*), first rake face (*MR*) and second rake face (*RU*). To simplify the calculation around the honed edge, two straight lines are introduced to substitute the rounding. And the intersection of these two lines is assumed as the material separation point, where the deformed material flow is divided. The chip curling and backflow effect are both considered. The model is experimentally proved to be practical in calculating cutting variables including chip-tool contact length and cutting forces etc.

The concept of separation point was adopted by Jin and Altintas [42] who in 2011 developed a similar slip-line field model for honed edge tool in micro cutting process. As demonstrated in Fig. 8d, the consists of four deformation zones, i.e., pre-flow region *ABN*, primary shear band *NBCDERQP*, secondary deformation zone *UTPQRS* and tertiary deformation zone *REG*. In the tertiary zone, point *H* acts as the separation point. The interfaces marked by RS and US represent two kinds of contact conditions at the chip-tool interface, i.e., sticking contact and sliding contact. Different from previous model, the material shear flow stress is determined and integrated into the model by utilizing Johnson-Cook constitutive expression, which incorporates the effect from the strain and temperature.

As has been mentioned the last subchapter, Ozturk and Altan [43] suggested two slip-line fields focusing on sharp and honed edge, respectively in 2012. Figure 8e depicts the one for honed edge tool, where curveline AFBKD stands for the primary deformation zone. The region FBKDHJGPIS is the secondary deformation zone enclosed by the tool and two concave-downwards boundaries. The region HKD is assumed as the DMZ. The convex point K can be treated as the material separation point.

In 2017, Zhang et al. [44] proposed two slip-line field models for honed edge tool with respect to conditions of UCT lower than tool edge radius and higher than edge radius. These two models are separately given in Fig. 8 f and g. It can be found from those two schematic views that primary deformation zone is regarded as polyline ABDEF. The right-triangle region ADG acts as the secondary deformation zone, where side AG is the effective cutting edge. The extrusion in the tertiary zone is depicted by arc AC. Such a model is relatively simpler and convenient to investigate the size effect.

Recently in 2019, Wan et al. [39] provided a novel approach to determine the DMZ formed ahead of the honed edge in micro-milling process as shown in Fig. 8h. The upper and bottom endpoints of the DMZ are treated as two critical reflection points, where material flow changes its direction suddenly. Therefore, the shear strain at these two critical points tends to be infinite based on the infinite shear strain principle in slip-line field theory. In this way, the geometry of the DMZ is determined and two-dimensional micro-milling force model is developed with power functions. Though the whole picture of the slip-line field is not obtained, it still offers a unique way of exploiting slip-line field theory to investigate the mechanism of machining with honed edge tool.

2.3 Chamfered-edge tool

Once chamfered edge is applied to metal cutting process, a stagnation zone confined by the edge is clearly observed. This stagnation zone full of trapped material is then recognized as the DMZ. To quantify the formation of DMZ, plenty of slip-line field models have been developed. Some typical models are elaborated in Fig. 9

The analytical modeling on chamfered edge tool with slip-line field theory was pioneered by Zhang et al. [45] in 1991. As depicted in Fig. 9a, the DMZ is emphasized in black triangle *SED*. Three separate zones enclosed by slip lines can be observed, i.e., the primary deformation zone *HABDEG*, the secondary deformation zone *GESF*, and the DMZ. This non-uniform slip-line field model was later modified by Ren and Altintas [46] in 2000. It can be found from Fig. 9b that the modified model was more distinct. With the present model, the stress and strain in primary deformation zone, secondary deformation zone, tertiary deformation zone, and DMZ are determined. The DMZ ahead of the chamfer is acting as the actual cutting edge separating the material flowing upwards and compressed below.

To simplify the calculation, Fang and Wu [47] in 2005 suggested a new slip-line field model for chamfered edge tool. As given in Fig. 9c, the primary deformation zone is substituted by a polyline *AEFB* without sub-region. Two additional fan-shaped transition zones are introduced, considering the stress singularity at the chamfer vertex *D* and chip-tool detaching point *C*. This model was then

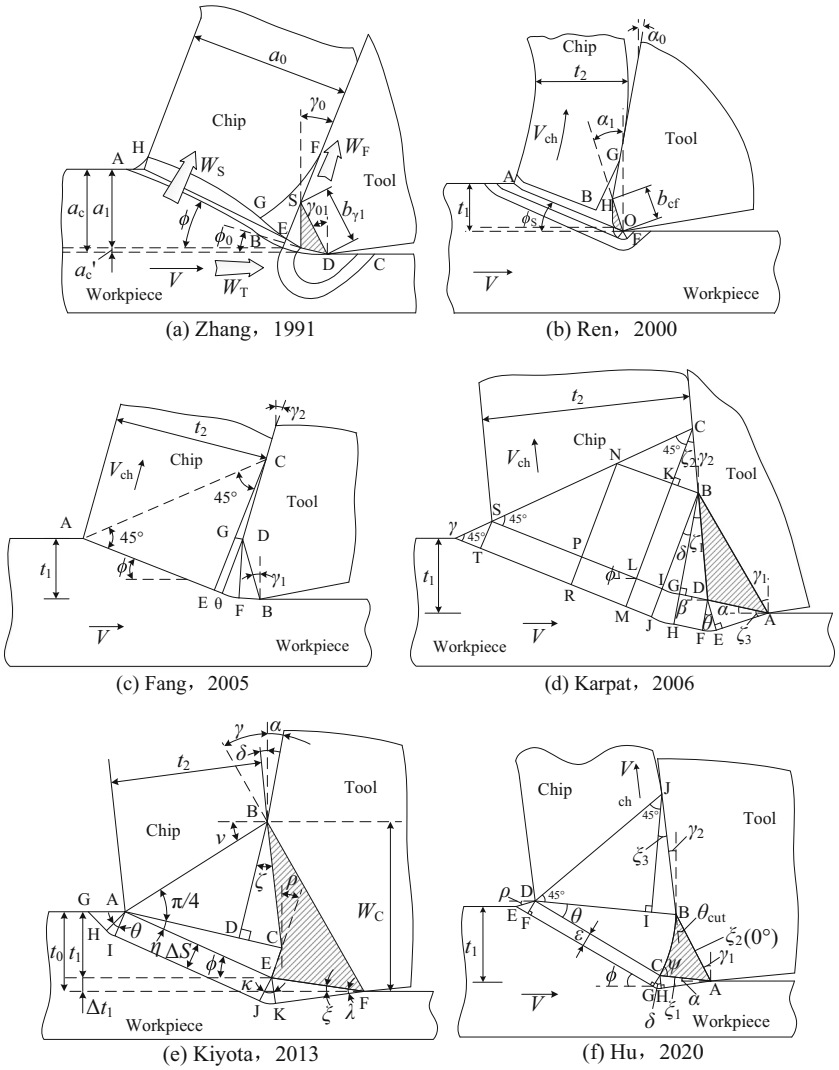

Fig. 9 Slip-line field models for chamfered edge tool. **a** Zhang 1991. **b** Ren 2000. **c** Fang 2005. **d** Karpat 2006. **e** Kiyota 2013. **f** Hu 2020

extended by Karpat and Özel [48] to negative-rake-angle cutting process as shown in Fig. 9d. The DMZ is still assumed as triangle. Different from previous work, the pre-flow region and sub-region are all considered. This uniform slip-line field model is helpful to compute the heat generation at the three main deformation zones.

The model shown in Fig. 9e was released by Kiyota et al. [49] in 2013. Different from traditional triangular DMZ, there is a small modification in the new model for the stress singularity at point *A* is also considered. Therefore, an additional fan region AEC is introduced. It can be noticed that the present model is dealing with the cutting condition where UCT is close to the chamfer height.

In 2020, Hu et al. [50] proposed a modified slip-line field model for negative-rake-angle cutting with chamfered tool (see Fig. 9f). The left side of the DMZ is changed into an arc boundary from the fan region DBC. The pre-flow region DEF and sub-region AHC are both considered. Stress singularities at the vertex *D* and *C* are concerned. Besides, an analytical thermal model is deduced based on the slip-line field model as well in the paper.

On the basis of the analysis above, a conclusion can be drawn that material separation is indeed existed and has been characterized by two main kinds of treatments, i.e., separation point and DMZ. It is hard to say which one is correct and better since every slip-line field model is developed with respect to various objectives and cutting conditions. What can be assured is that the investigation on honed edge with slip-line field theory is the tendency of future analytical researches. However, although numerous slip-line models are presented for metal cutting process, an intuitive mean for validation is still lacking. The validation of slip-line modeling is mainly from the perspective of cutting force. A more advanced technique for material characterization at high deformation speed and temperature is required.

3 Cutting mechanics

3.1 Cutting force

The total cutting force consists of shear force and edge force which is related to the micro edge geometry of tool in the cutting operations [52]. The cutting force prediction model that considers the edge geometry was proposed in the middle of the twentieth century [53], which is called the phenomenon of ploughing process. The percentage of edge force in total cutting force is often considered insignificant in previous literature and sometimes neglected in force modeling for simplification reasons. However, Moufki et al. [54] pointed out that the importance of edge force depends on the relation between UCT and edge size, edge force can be dominant when edge size is comparable to edge size. As shown in Fig. 10, various edge geometries are used to illustrate the edge effect in cutting operations. The result shows that cutting tools with microgeometries withstand a larger cutting force than a sharp tool in the condition of the same cutting parameters [51]. Similar results were obtained in micro-milling with different edge preparations [55]. The rounded and chamfered edge tools show high cutting force than sharp tool due to the increase of the effective rake angle by the chamfered edge.

Some scholars proposed analytical models for edge force components, attempting to explain the generation of edge force caused by deformation. For rounded tools, Waldorf et al. [40] proposed an effective function for the edge forces in orthogonal cutting as given in the following equation, the related slip-line field model can be found in Fig. 11a.

$$P_{cut} = k{\cdot}w{\cdot}[\cos 2\eta{\cdot}\cos(\phi{-}\gamma+\eta) + (1+2\theta+2\gamma+\cos 2\eta){\cdot}\sin(\phi{-}\gamma+\eta)]{\cdot}CA$$
$$P_{thr} = k{\cdot}w{\cdot}[(1+2\theta+2\gamma+\sin 2\eta){\cdot}\cos(\phi{-}\gamma+\eta){-}\cos 2\eta{\cdot}\sin(\phi{-}\gamma+\eta)]{\cdot}CA$$

where P_{cut} is the force components in cutting speed direction and P_{thr} is the thrust force component. k is the shear stress in shear zone; η, ϕ, γ, and θ are the angles described in slip-line field; w is the width of cut; and CA is the contact length between DMZ and workpiece. This model is widely adopted by scholars in analytical modeling of metal cutting processes [56–58].

Abdelmoneim and Scrutton [38] also proposed an edge force model considering the presence of a stagnation point on tool edge, θ_0 is the corresponding stagnation angle as shown in Fig. 11b. The expressions of edge force components are given as follows, including three force components in oblique cutting.

$$K_{te} = r_e{\cdot}k{\cdot}\left(\frac{2\theta_0}{\cos\theta_0} + \pi{\cdot}\sin\theta_0{\cdot}\tan\theta_0\right)$$
$$K_{fe} = r_e{\cdot}k{\cdot}\left(2\sqrt{3}\sin\theta_0\right)$$
$$K_{re} = K_{te}{\cdot}\sin\lambda_s$$

where K_{te}, K_{fe}, and $K_{r\beta}$ represent the edge force coefficients in cutting speed, tangential, and radial directions, respectively. r_e is the edge radius, λ_s is the inclination angle. This model also serves in many literature for force modeling [59–61].

For chamfered tool, [20] presented a semi-analytical model based on the simulation results, where a linear correlation between chamfer length, chamfer angle trigonometric function, and cutting force components can be found. The function is given as below.

$$\begin{cases} K_{te} = p_t{\cdot}k{\cdot}L{\cdot}\sin\theta \\ K_{fe} = p_f{\cdot}k{\cdot}L{\cdot}\sin\theta \\ K_{re} = p_r{\cdot}k{\cdot}L{\cdot}\sin\theta \end{cases}$$

where L and θ are chamfer length and chamfer angle, respectively. p_t, p_f, p_r are the model constants that required calibration through cutting tests. The authors applied this edge force expression for force modeling when cutting with a round insert.

Apart from analytical models, a lot of experimental work has been done in previous literature to find out the influence of edge geometry on cutting forces for different tool-workpiece couples and cutting conditions. Figures 12 and 13 show a similar linear relation between edge radius and cutting force component, with different workpiece materials employed (Titanium and Inconel 718). Similar trends can also be found in milling processes [66, 67]. Figure 14 focuses on general honed edge, with all microgeometries characterized by S_α and S_γ (cutting edge

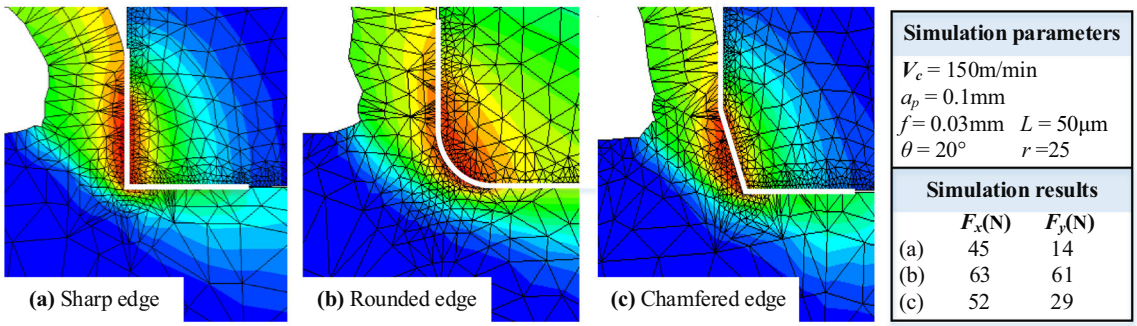

Fig. 10 Orthogonal simulations with various edged tools [51]. **a** Sharp edge. **b** Rounded edge. **c** Chamfered edge

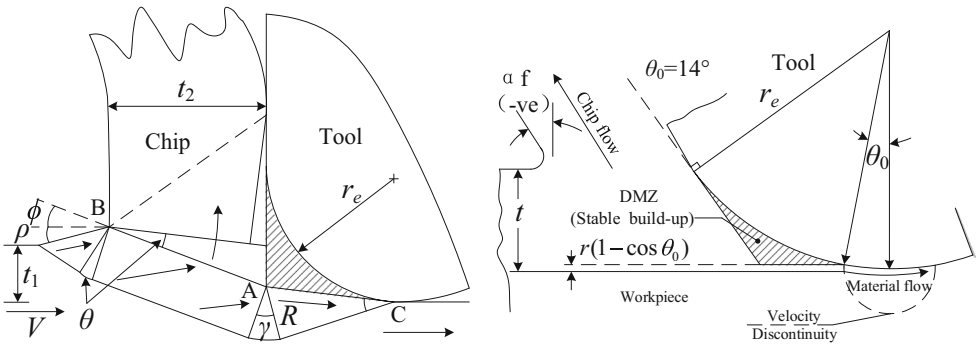

Fig. 11 Descriptions of two analytical models of edge force for rounded edge [38, 40]

segment on flank face and rake face). It can be found that the effect of S_α is positive on force components while S_γ is negative, which can be explained from the geometric analysis that a larger S_α will increase ploughing effect while a larger S_γ will lead to a more positive effective rake angle. This phenomenon is similar to that found by Padmakumar [68] when investigating milling processes. More discussions on the influence of S_α and S_γ on cutting force can be found in refs. [22, 69–71]. Figure 15 correlates the force coefficients with the ratio of UCT to r_e, where a sharp increase of force coefficients can be found when UCT is much smaller than edge radius. When the ratio is larger than 5, the force coefficients almost keep stable. In such condition, ploughing effect is negligible and shear effect takes the dominant place. Figure 16 discussed the edge chamfer width (i.e., chamfer length in orthogonal cutting). Researches targeting on the effect of chamfered edge tools on cutting force can also be found in Refs [12, 65, 72, 73]. Most mentioned literature briefly stated that cutting force rises with increasing chamfer length and chamfer angle of tool and considered the trend as linearity. Weng et al. [21, 74] proposed that the correlations between cutting force and the ratio of chamfer length to UCT can be divided into three stages based on the simulation results of both Inconel 718 and AISI 304, further, a *S* shape function was given to improve the force prediction.

3.2 Cutting temperature

Machining operation withstands severe deformation that could cause high thermal loads acting on the tool and workpiece, resulting in excessive tool wear and poor surface quality. With the requirement of longer tool life and higher surface integrity, investigations on cutting temperature are as significant as that of cutting force. The methods often used to predict the cutting temperature profiles include numerical (i.e., finite element method (FEM)), analytical, and hybrid methods. Long computing time is always the limitation of FEM modeling of metal cutting especially in three-dimensional simulations, which restricts the application of this method. However, it is still the main approach in temperature modeling because it can provide every detailed information during cutting processes [75–78]. Analytical method represents another important methodology in prediction cutting temperature, which is advanced in fast prediction and understanding the in-deep mechanisms. Although with a lot of assumptions to simplify the model, analytical model has been proved as a practical effective tool in cutting temperature modeling [79]. Hybrid methods represent those combine two or more approaches to estimate the cutting temperature values and distribution profiles with physical explanations. Usually, the hybrid method is to apply the outcomes (e.g., strain, stress, force, contact length) of numerical models to the analytical, empirical, or

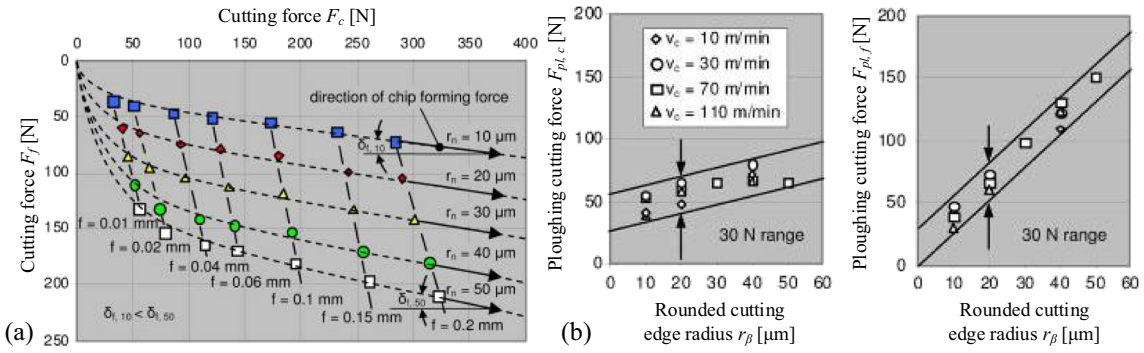

Fig. 12 Tool and cutting parameters vs. forces. **a** Effect of cutting edge radius and feed rate on cutting forces. **b** Effect of cutting edge radius and cutting speed on ploughing forces [62]

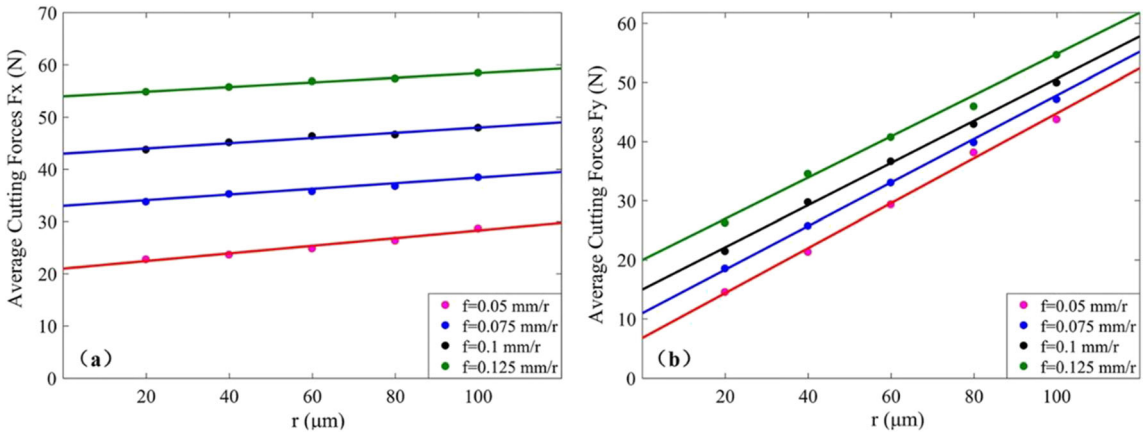

Fig. 13 Effects of edge radius and feed rate on cutting forces with rounded tools after turning at a_p = 0.1 mm by FEM [51]

artificial intelligence (AI) model to predict cutting temperature more accurately and save the computing time as well [80, 81].

Tools with different edge microgeometries are employed to predict the cutting temperature profiles based on 2D simulations (Fig. 17) and 3D simulations (Fig. 18). It can be noted from the simulation results that the max temperature is located in the tool flank surface, where the friction between chip and tool influences the temperature distributions. Edge profile zone of tool involved in the severe plastic deformation of the material withstands the highest thermos-mechanical loads than other zones. As shown in Fig. 17, the maximum temperature on the tool tips rises with the increase of edge radius. The temperature distribution beneath the machined surface is highly affected by the form-factor K. Deformation mainly occurs on the rake face when K>1 while near machined surface when $K < 1$, which leads to a lower temperature profile beneath machined surface when $K < 1$. Also, the changes of the contact conditions between tool-chip caused by different edge geometries will influence the heat generation and dissipation in the cutting operation. As shown in Fig. 18, the tool with chamfered edge shows less efficiency when compared with honed or asymmetry edged tools for the higher cutting temperature on the rake face. This may be resulted by the increase of effective rake angle which in turn increases the friction with chamfered tools. The friction and stress on contact area increase with the decrease of the ratio of instance uncut chip thickness to edge radius due to size effect. Thus, uniform microgeometry shows higher cutting temperature compared with variable edge. Similar results were obtained by Segebade et al. [83] in cutting TiAl4V with asymmetry tools shown in Fig. 19.

Although FEM methods can reveal the effects of edge geometry on temperature distribution and maximum temperature, it is still hard to explain the in-deep physics. This can be solved by analytical models, where three heat sources (shear plane heat source, frictional heat source at the tool-chip interface, and frictional heat source at tool-workpiece interface) are often considered to calculate the temperature rise in tool, chip, and workpiece, corresponding to three deformation zones [84, 85]. For a sharp tool, only shear plane heat

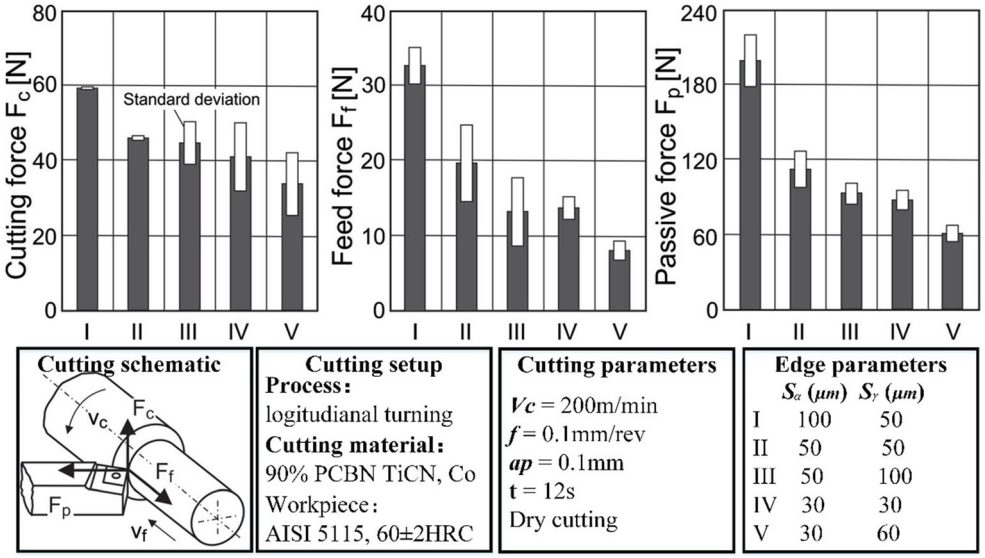

Fig. 14 Cutting setup and cutting forces with different rounded edge tool [63]

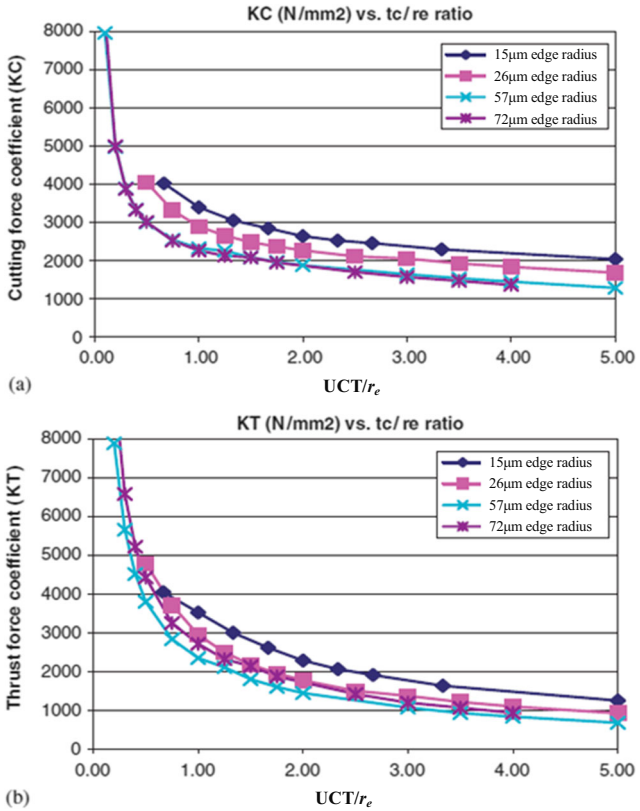

Fig. 15 Force coefficients vs. UCT/re: **a** cutting force; **b** thrust force [64]

source and tool-chip frictional heat source exist. When tool edge is taken into account, the presence of DMZ, ploughing zone will change with different microgeometries, causing the difference of heat-source distributions. From this aspect, it is possible to explain the influence of edge geometry on cutting temperature. For sharp tool, Komanduri et al. [84, 85] integrated previous models and proposed a widely accepted analytical model that employs image heat source for temperature modeling considering multiple boundary conditions. Later, Huang and Liang [86] presented an enhanced model for the frictional heat source at tool-workpiece interface. But in their model, the tool is still a sharp tool with a flat flank wear face. Hence, the expressions of the temperature rise cause by multiple heat sources is determined, the total temperature rise at an arbitrary point can be obtained by adding the efforts of all related heat sources.

For rounded tool, DMZ is always formed in front of tool tip and then employed as the real cutting edge; thus, the three heat sources can be modeled. From this aspect, a slip-line field model is required or the tool-workpiece interface can be simplified as on the same line of machined surface, as shown in Fig. 20. The influence of edge radius is mainly on the frictional heat source of tool-workpiece interface based on the presented model, similar solutions can be found in refs. [58, 87]. A larger edge radius can enhance the ploughing effect and enlarge the total cutting force, which leads to the improvement of heat intensity of heat sources. Therefore, cutting temperature will increase with the growth of edge radius based on the analytical models.

When it comes to chamfered tools, the DMZ in front of the tool chamfer introduces DMZ heat sources and induced heat sources in the deformation zone [89]. This characteristic can be considered because the geometry of chamfered tool is much simpler than that of rounded edge. As shown in Fig. 21, scholars have attempted to model the heat sources caused by chamfered tools based on slip-line field theory and moving heat source method [9]. Analytical modeling treats the cutting temperature the production of all heat sources, which means larger and stronger heat sources can result in a higher maximum temperature. Therefore, it can be imagined that a more negative chamfer angle or a larger edge radius can introduce a larger heat source on tool-workpiece interface and strengthen the heat intensity by enlarging the cutting force, further, increase the maximum cutting temperature. Similar trends have been presented in ref. [90], where the maximum temperature with various chamfer features is obtained and the cutting temperature increase with the larger chamfer angles and larger chamfer lengths (see Fig. 22).

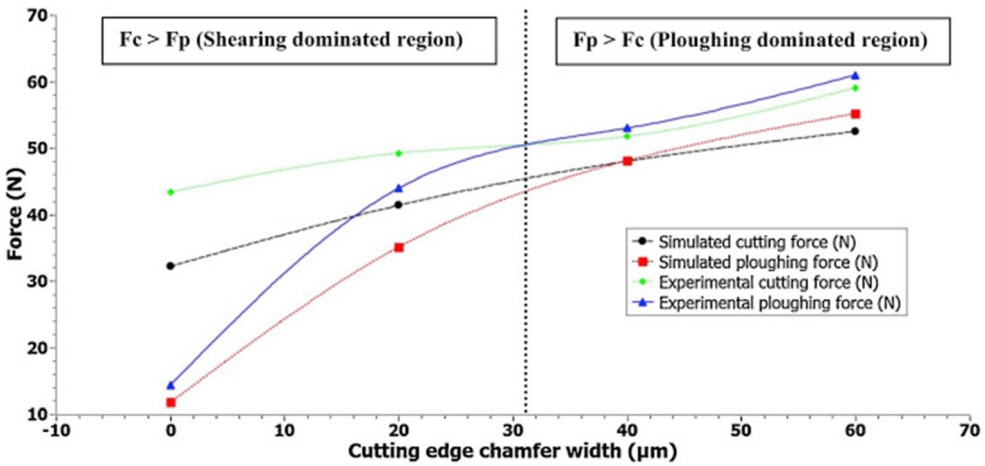

Fig. 16 Cutting forces at various chamfer length (f = 0.03 mm/rev) [65]

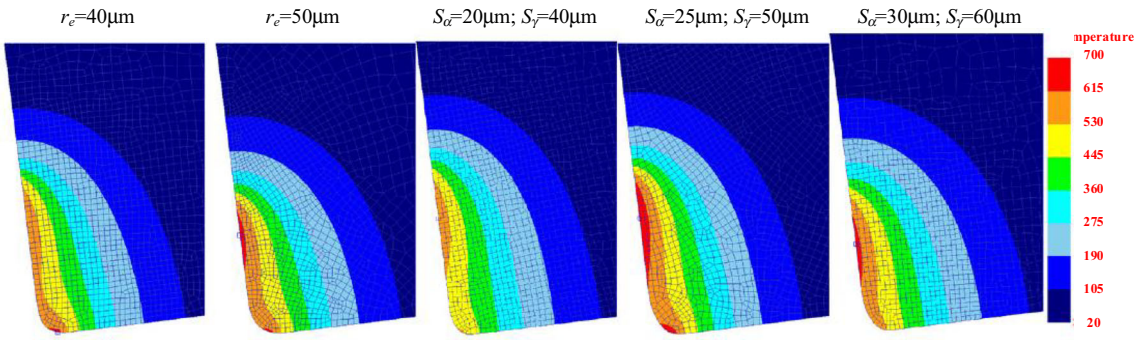

Fig. 17 Temperature distributions for rounded or honed tools based on 2D FEM simulations (V_c = 175 m/min, UCT = 0.15 mm) [17]

4 Tool performance

4.1 Wear behavior

As a significant indicator of tool performance, excessive tool wear will enlarge the mechanical and thermal loads, further, lower the surface quality. Most of the literature focus on the effects of cutting parameters, tool macrogeometries, lubricants, or coatings on tool wear. In recent years, researches pointed out that the tool performance in cutting operation is deeply influenced by the tool edge microgeometries. The edge geometry affects the thermal-mechanical loads on the tool edge through the different contact geometry between tool and workpiece [91]. Investigations of the cutting edge preparation on the wear mechanism is needed in tool design for industrial production.

Micro edge geometry of the tool changes the effective cutting angle in the contact area of tool and workpiece, which makes the tool with uniform or variable microgeometry show different wear resistance [82]. The friction factor as well as the special cutting energy shows an increase with decreasing instantaneous UCT. It can be estimated that the ploughing effect becomes more and more dominant with the decrease of the edge radius, which will discourage the tool performance. As shown in Fig. 23, Tiffe et al. [92] studied the effects of different honed microgeometries on tool wear in machining Nickel-based alloys and found that the wear rate is determined by S_α while S_γ shows limited effect. The wear rate can be significantly reduced if a tool with smaller S_α is employed. A deep analysis of the honed edge microgeometries has been presented in ref. [93] (Fig. 24), concluding that the flank wear is sensitive to the S_α, while crater wear is mainly influenced by

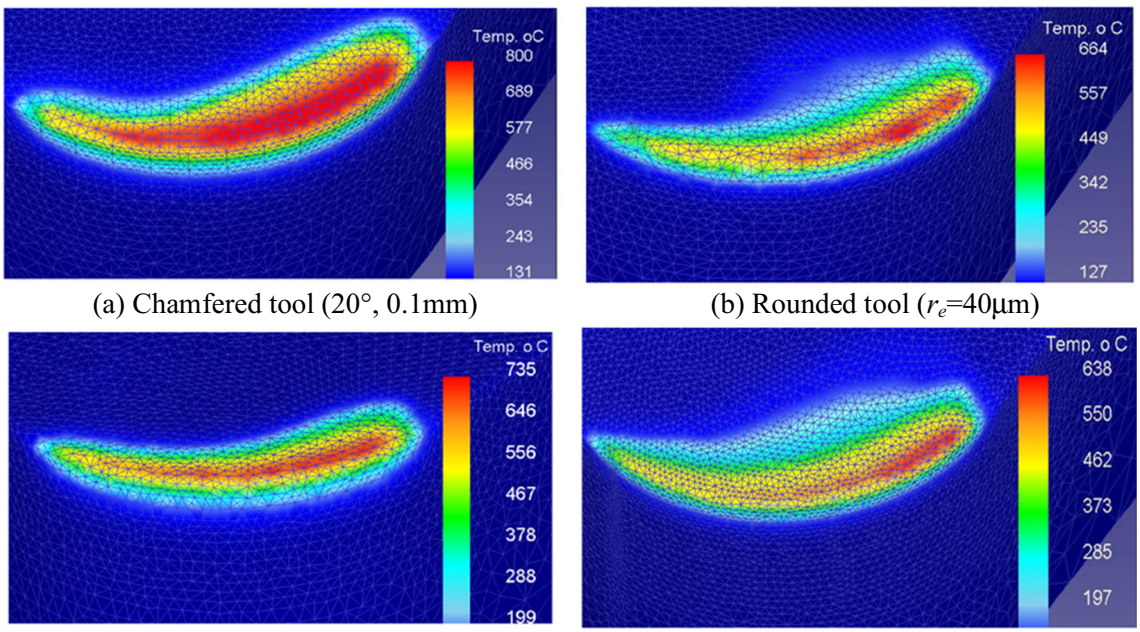

(a) Chamfered tool (20°, 0.1mm)

(b) Rounded tool (r_e=40μm)

(d) Honed tool (S_α=30μm; S_γ=60μm)

(d) Honed tool (S_α=50μm; S_γ=10μm)

Fig. 18 Temperature distributions for chamfered, rounded, or honed tools based on 3D FEM simulations (AISI 4330 steel, 40HRC, V_c = 300 m/min, f = 0.15 mm/rev, a_p = 1 mm) [82]. **a** Chamfered tool (20°, 0.1 mm). **b** Rounded tool (re = 40μm). **d** Honed tool ($S\alpha$ = 30 μm; $S\gamma$ = 60 μm). **d** Honed tool ($S\alpha$ = 50 μm; $S\gamma$ = 10 μm)

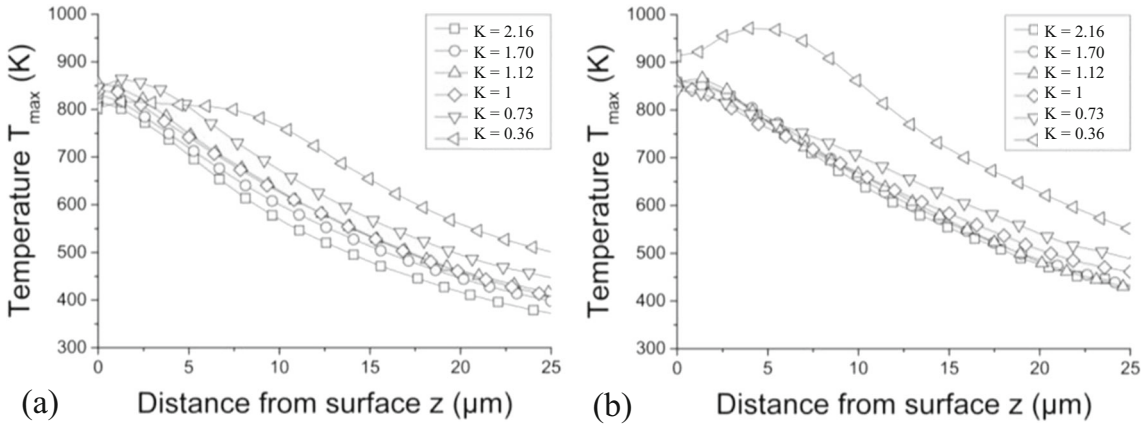

Fig. 19 Temperature distributions in subsurface for different *K* values after 1 mm length of cut: **a** UCT = 0.1 mm; **b** UCT = 0.3 mm [83]

S_γ. In the study by Zhao et al. [8], three types of rounded cutting tools were used to investigate the effect of tool radius on the wear behavior. They noticed that the larger the cutting edge radius is, the better the wear resistance of tool will be.

The flank wear mechanism when turning 17-4PH stainless steel with rounded edge tools was investigated by Fu et al. [94], shown in Fig. 25. The SEM results illustrate that the main wear behavior for rounded tool is abrasive wear and adhesive wear on the flank face. Flank wear as well as the groove wear play the dominant roles in this cutting situation. It can be also noted from EDS results that the elements in workpiece diffused into the wear area due to the thermal-mechanical coupling effect.

chamfered edge. **b** Rake face of tool with variable chamfered edge. **c** Flank face of tool with invariable chamfered edge. **d** Flank face of tool with variable chamfered edge. **e** Crater wear change curves with different tools. **f** Rake wear change curves with different tools

For chamfered tools, Zhou et al. [95] studied the influence of chamfer angle on flank wear of PCBN tools, which shows

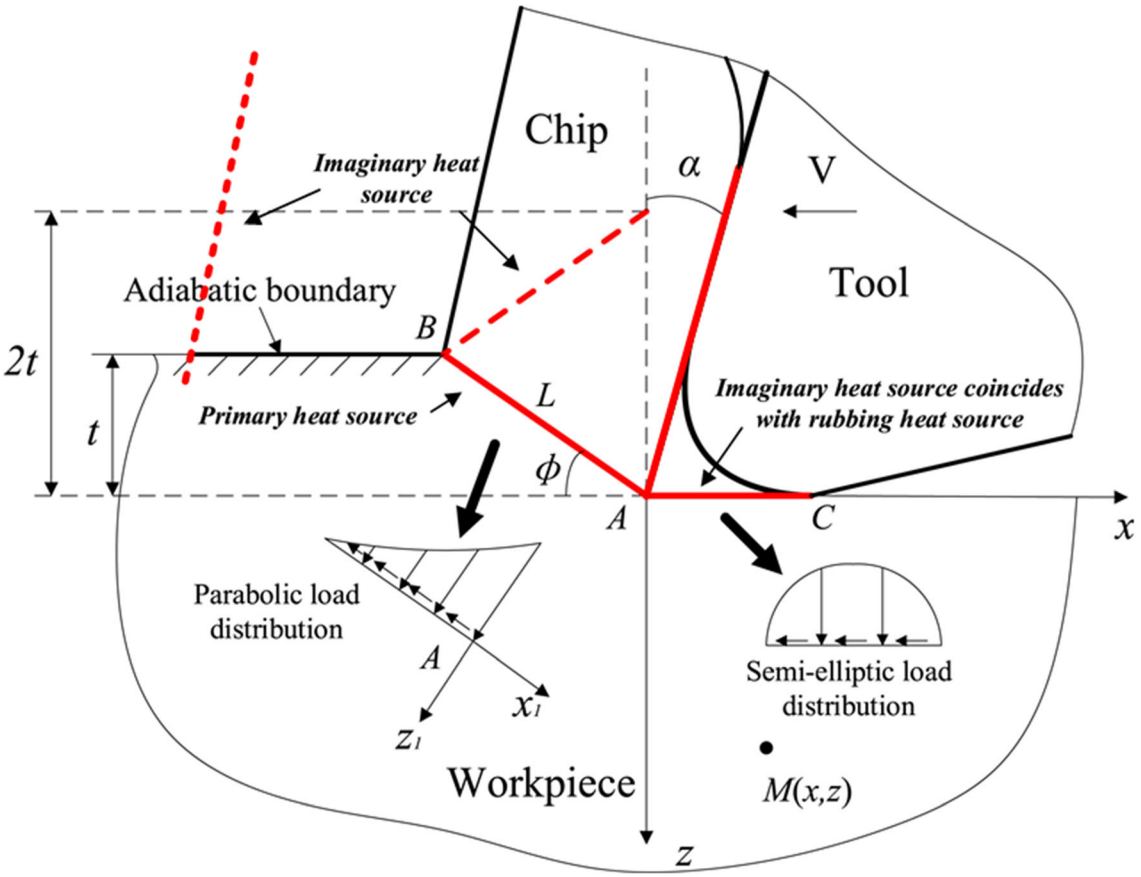

Fig. 20 Descriptions of heat sources for rounded tool, improved from ref. [57]

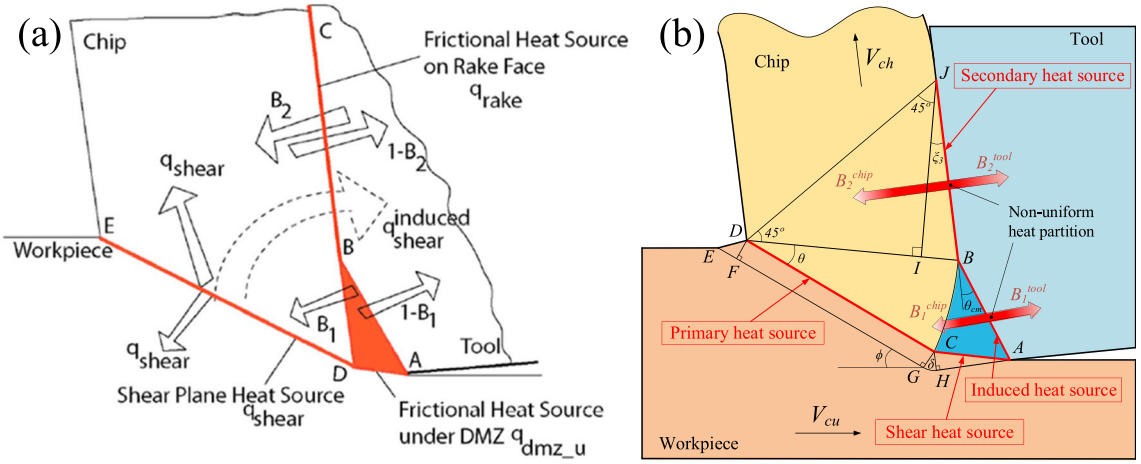

Fig. 21 Descriptions of heat sources for chamfered tool. **a** Simplified DMZ by Karpat and Özel [88]. **b** Improved DMZ by Hu et al. [50]

the best design of the chamfer angle is 15° (see Fig. 26). Chen et al. [96] compared the influence of invariable and variable chamfered edges on the tool wear modes of PCBN tools when machining GCr15. The invariable chamfered edge has fixed chamfer width and angle along tool nose while the variable chamfered edge has varying chamfer angle and fixed chamfer width. As described in Fig. 27a–d, the crater wear concentrated on the rake face and relative uniform flank wear on the flank face is the main wear mode when cutting with invariable chamfered tool. For variable chamfered angle tool, the rake face bears more crater wear and the flank wear is a long triangle and uneven distribution on the flank face, wear on the middle of the flank face is wider than that on sides. Figure 27e shows the crater wear and flank wear variation with two different kinds of chamfered angle tool. The wear curves of variable and invariable chamfered angle tools show similar trends in the first 4 min. Then, the curves of invariable chamfered tool grow faster than that of variable chamfered angle tool, which means the variable chamfered angle tool has superior wear resistance than the invariable one in the rake face. For variable chamfered edge, the second crater wear starts when the cutting time passed about 16 min, which may be caused by the enlarger contact area between tool and chip. The flank wear curves of different chamfered angle tools are given in Fig. 27f. The flank wear length keeps steady for both invariable and variable chamfered tools; meanwhile, the wear length of invariable tool is smaller than that of variable one. Also, the maximum wear width of cutting tool with invariable chamfered tool is larger than that of variable one. That means the invariable chamfered edge suffers severe flank wear than variable one. The tool wear with different chamfered length was studied by Gao et al. in micro-milling aluminum alloy 7075 [55]. In their study, the sharped edge tool

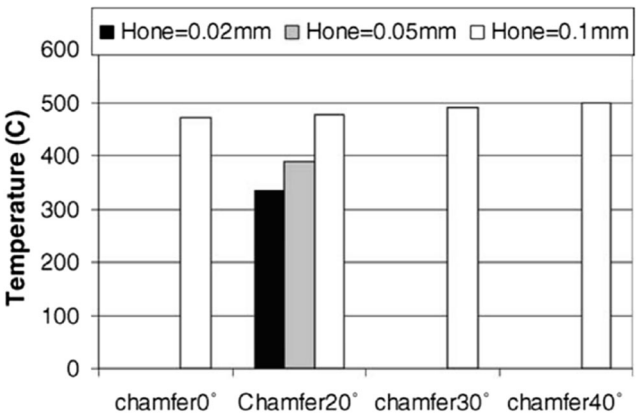

Fig. 22 Effects of chamfer angle and edge radius on maximum temperature (V_c = 20 m/min, f = 0.28 mm/rev, a_p = 0.35 mm, HRC = 56) [90]

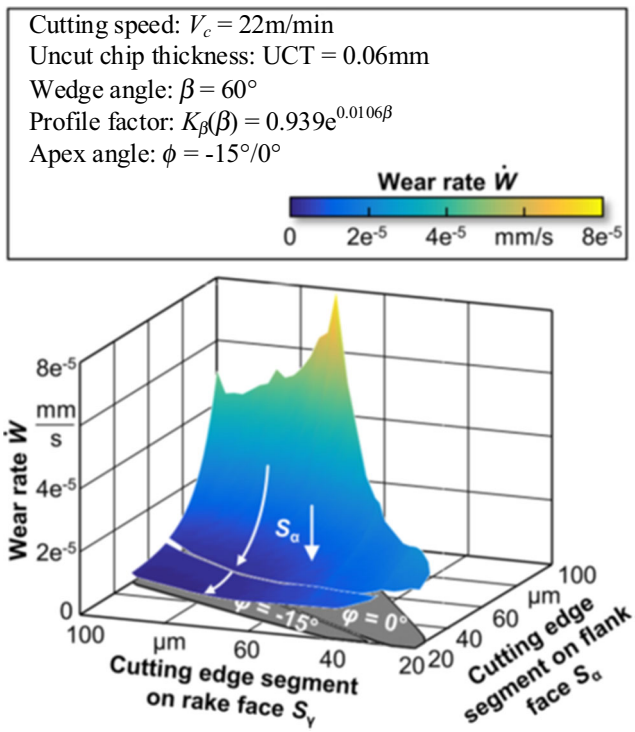

Fig. 23 Relationship between maximum wear rate and edge segments (S_α and S_γ) [92]

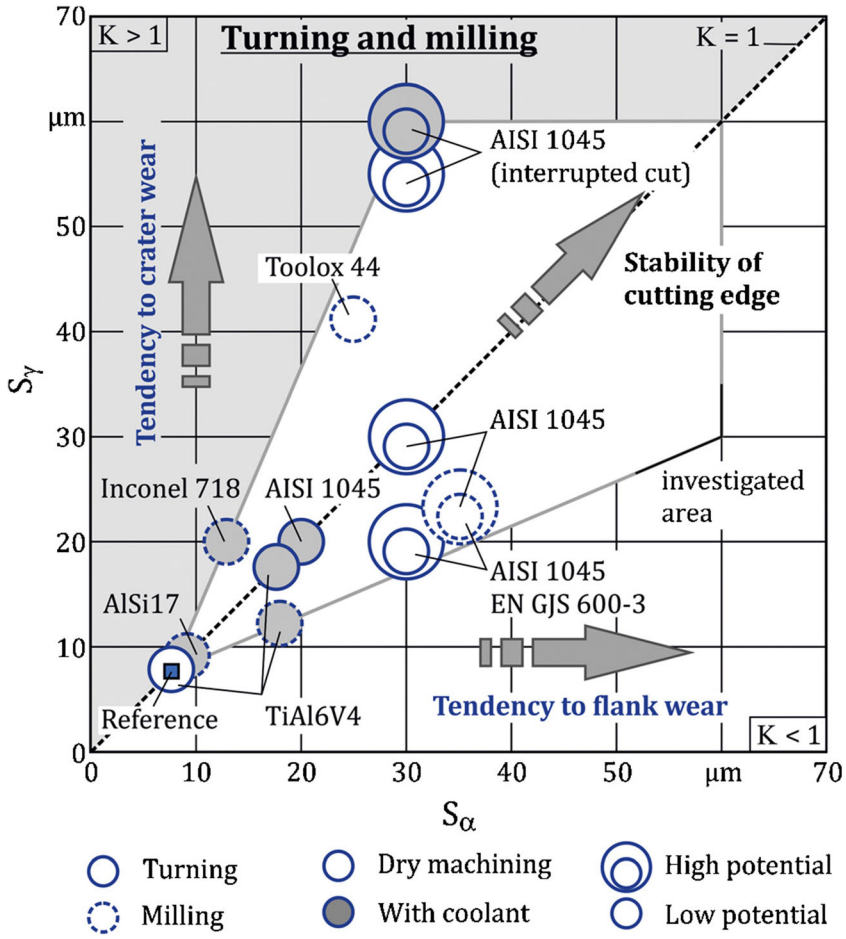

Fig. 24 Tool wear map for tailored micro edge geometry [93]

easily suffers fracture at the tool tip, which will cause tool broken at the cutting period. For chamfered edge tool, the adhesion wear is the main wear mechanism and larger chamfer length can enhance tool performance and prolong tool life.

Ventura et al. [22] investigated the tool performance with sharp, chamfered, honed tools employed in interrupt turning 16MnCrSS steel. As shown in Fig. 28, the chamfered insert shows superior wear resistance than other inserts, though the sharped inserts withstand lowest thermal-mechanical loads on the edge. The chamfered edge strength the cutting inserts and improve the wear resistance, while the sharped edge shows less stability in cutting operation. The honed edge (K = 2.0, 1.0, 0.5) shows lager flank wear width than chamfered tools, further, wear resistance can be worse with the reduction of K. Also, severe notch wear can be found on honed edge when compared with chamfered and sharp tools.

The methods of edge preparation also make difference to the tool wear behavior due to the various edge properties. Wang et al. [97] used three edge preparation technologies (brushing, drag finishing, and wet abrasive jet machining) in orthogonal cutting, with each tool sharing the same edge radius (r_β = 20 µm). It is reported that drag finished edge shows the best surface quality and highest hardness, resulting in a lowest flank wear when compared with other prepared tools. Bouzakis et al. [98] stated that grinding plus coating is much better than micro-blasting when producing rounded edge of milling tools, which is based on the maximum cuts before fracture of coating happens.

4.2 Tool life

Tool life is defined when the tool wear exceeds a specified value, which is the most important issue that the tool manufacturing industries focus on. Tool suffers extensive tool wear must be replaced to protect the machining system and ensure the part quality. Table 1 gives a summary of the effect of the micro edge geometries (rounded, chamfered, and sharp edge) on tool life in turning and milling operations in recent years. With the general agreed results, curvilinear and straight edge geometry has positive effect on the tool life comparing with the sharp cutting insert. The rounded and chamfered edge can strengthen the cutting tool to withstand higher thermal-mechanical loads; hence, prolong the tool life.

As mentioned above, different preparation methods may induce various edge properties of tool and show different tool performance in cutting operations. Chen et al. [110] used the

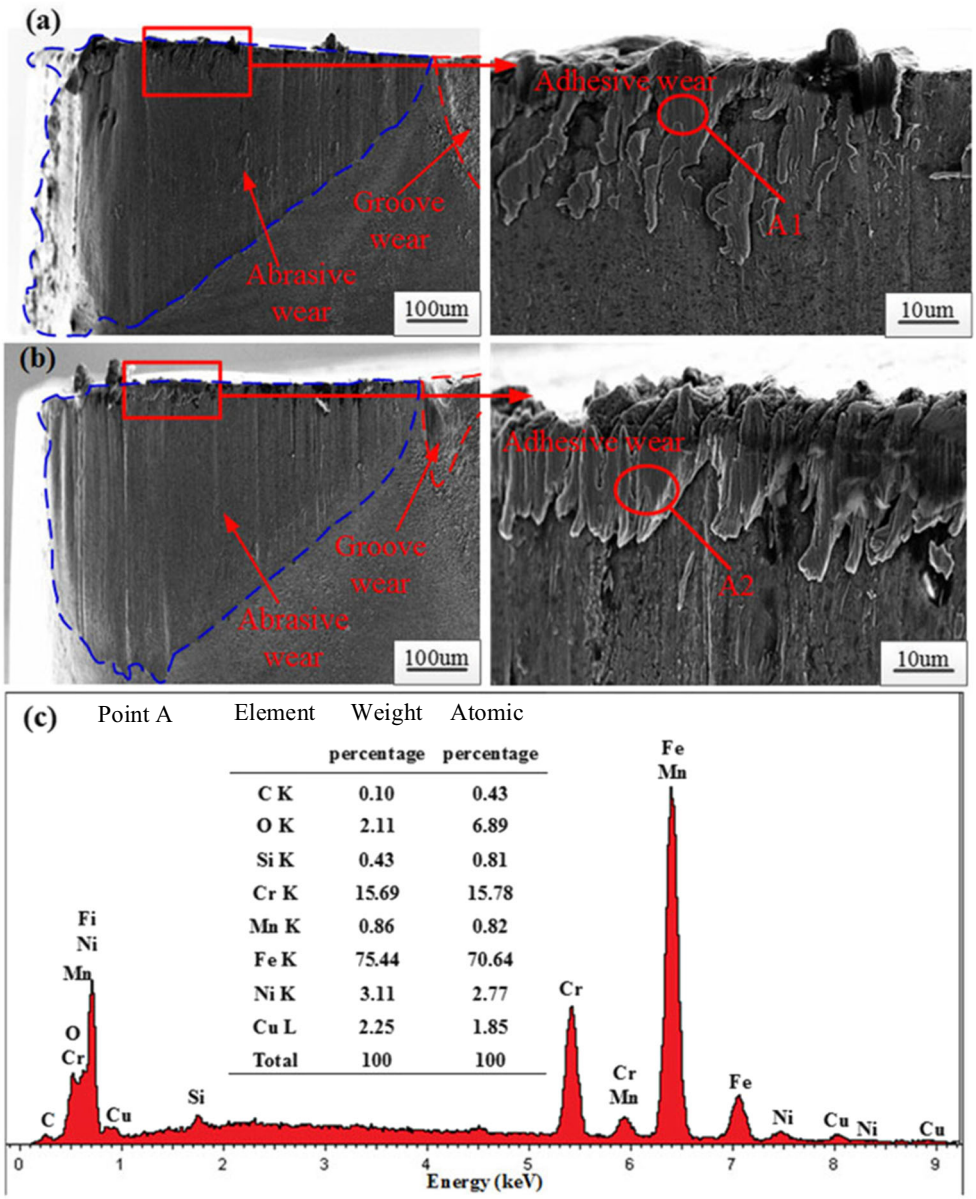

Fig. 25 The SEM images and EDS results of worn flank face when machining 17-4PH stainless steel using cermet inserts at V_c = 250m/min, f = 0.1 mm/rev, a_p = 0.3 mm [94]

magnetic polishing method to obtain various edge radius from 7 to 49 μm, then series of drilling tests were employed for tool performance evaluation. The edge radius ranges from 24 to 27 μm shows superior cutting performance and longest tool life. Similar results were obtained when turning AISI 1045 with rounded cutting edge inserts (r_β = 30 μm) [69]. A suitable edge radius can significantly improve the tool life by 86% when compared to inserts without micro-abrasive blasting

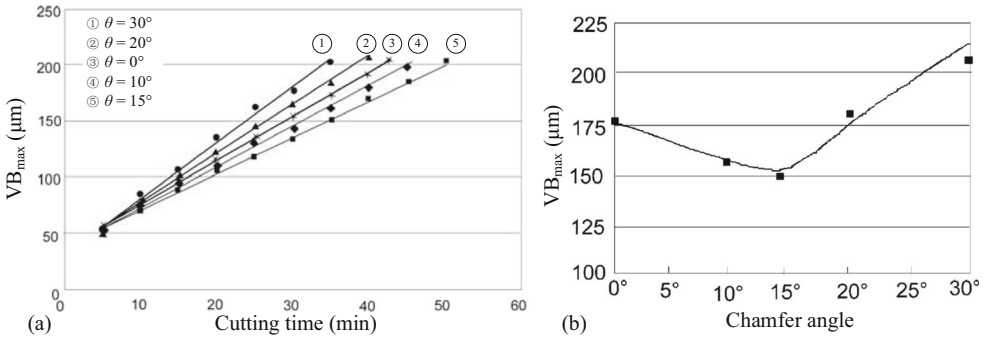

Fig. 26 Influence of chamfer angle on flank wear of PCBN tools (V_c = 160 m/min, f = 0.05 mm/rev, a_p =0.05mm) [95]. **a** Cutting time (min). **b** Chamfer angle

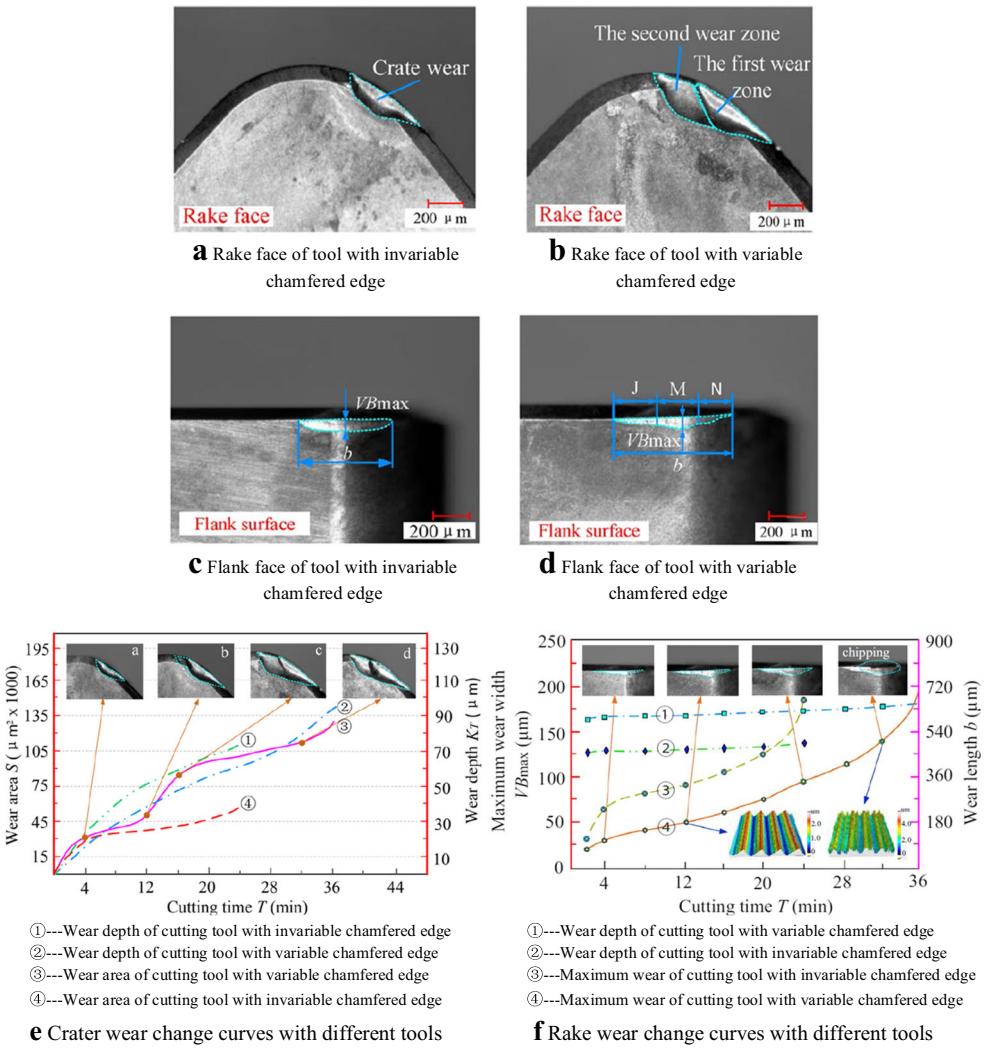

a Rake face of tool with invariable chamfered edge

b Rake face of tool with variable chamfered edge

c Flank face of tool with invariable chamfered edge

d Flank face of tool with variable chamfered edge

e Crater wear change curves with different tools

f Rake wear change curves with different tools

Fig. 27 Crater wear and flank wear for invariable and variable chamfered tools (V_c = 150 m/min, f = 0.2 mm/rev, a_p = 0.1 mm) [96]. **a** Rake face of tool with invariable

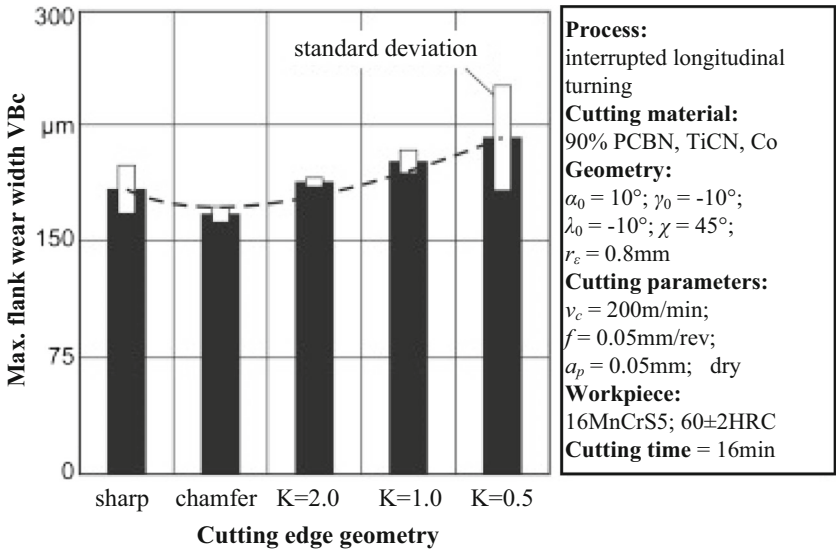

Fig. 28 Flank wear width after 16 min interrupt cutting with different edge microgeometries [22]

Table 1 Summary of researches discussing the influnecne of edge microgeometries on tool life

Methods	Ref	Workpiece	Tool	Edge geometry	Remarks
Turning	[97]	AISI 4140 steel	Cemented carbide	Rounded	Drag machining shows better tool life than abrasive jet machining and brushed machining at 100 μm flank wear.
	[94]	17-4PH	Cemented carbide	Rounded	Rounded edge with 15 μm radius shows the highest tool life.
	[99]	17-4PH	Cemented carbide	Rounded	Micro-abrasive blasting method can improve the tool life 37% longer than unprepared ones
	[100]	GCr15	PCBN	Chamfered	Variable chamfered edge can prolong tool life compared with fixed chamfered edge
	[19]	Q235	–	Chamfered	Feed rate is sensitive to chamfer characteristic, small angle and large length for small feed rate, while large angle and small length for the large. Increase feed rate will shorten tool life.
	[22]	16MnCr55	CBN	Sharp, chamfered	The chamfered tool works better than sharp tool
	[101]	DF-3 tool steel	Ceramic	Rounded, chamfered	The chamfer tool can prolong the tool life compared with honed one.
	[102]	AISI 1045	Cemented carbide	Rounded	Longest tool life was obtained with honed cutting edge (S_γ = 50 μm, S_α = 30 μm), increase the S_γ and S_α will reduce the tool life.
	[103]	AISI 4340	PCBN	Rounded, chamfered	Variable micro-geometry cutting inserts shows longer tool life than invariable one.
Milling	[104]	AISI 304	Tungsten Carbide	Rounded	Same radius of different flutes shows shorter tool life compared with the various radius of different flutes.
	[105]	Aluminum 7075	Cemented carbide	Sharp, chamfered	Chamfered tool shows superior performance than sharp tool
	[106]	Austenitic stainless steel	–	Rounded	Small rounded edge can improve 54.8% tool life compared with sharp edge tool
	[107]	X12CrMoVNbN9-1	Sintered carbide	Rounded	With the increasing edge radius, the tool life rises
	[108]	Inconel 718	–	Rounded	The increasing rounded (2 to 25 μm) prolong the tool life
	[109]	42CrMo4	Cemented carbide	Rounded	K influence the tool life and longest tool life can be obtained with S_α = S_γ = 30 ± 5μm.

preparation. The inserts with micro-abrasive blasting shorten the stage of initial wear and prolong the transitional wear phase, then a longer tool life can be obtained.

Symmetrical and asymmetrical tool edge asl show different tool performance, for instance, the maximum tool life can be obtained with asymmetrical edge radius (S_α = 30 μm and S_α = 50 μm) when compared with symmetrical ones in turning AISI 1045 steel [102]. As shown in Fig. 29, the tool life map with different honed microgeometries is given in slot milling of 42CrMo4-QT [109], where series of cutting tests were performed to evaluate tool life with the defined wear criteria. It can be noted that the increase of S_α and S_γ will

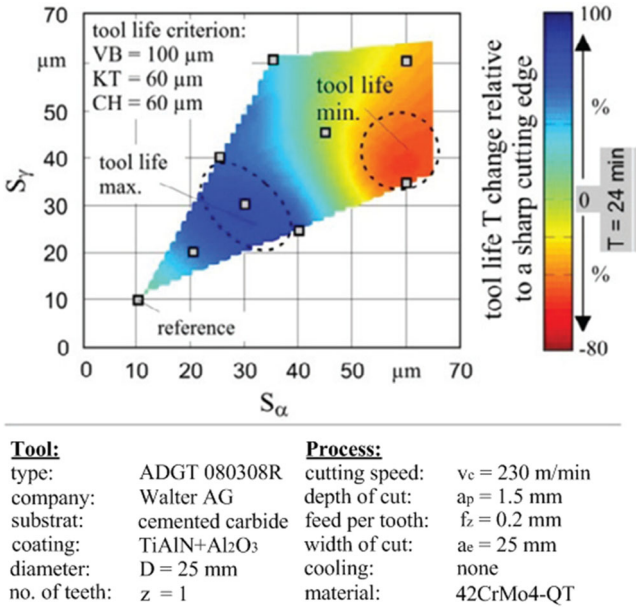

Fig. 29 Tool life map with various honed microgeometries [109]

not always extend the tool life compared with the reference tool life (lifetime of sharp tool). The maximum tool life can be obtained when S_α = 30 µm and S_γ = 30 µm, extending the reference tool life by almost 100%. However, an improbable combination of S_α and S_γ will reduce the tool life by 80%. According to the research by Davoudinejad et al. [101], the chamfered edge tools show longer tool life compared with honed edged tools in hard turning ASSAB DF-3 tool steel. Fu et al. [94] investigated the lifetime of tools with edge radius ranging from 5 to 45 µm, which demonstrated that 15 µm is the best choice of edge rounding with the longest tool life (see Fig. 30).

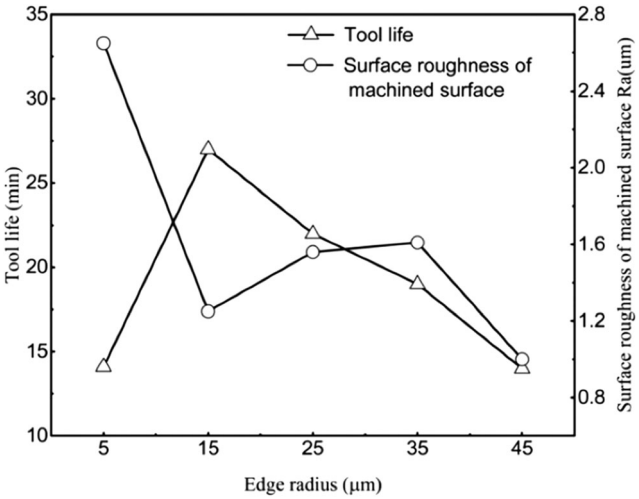

Fig. 30 Tool life and surface roughness vs. edge radius when machining 17-4PH martensitic stainless steel at V_c = 250 m/min, f = 0.1 mm/rev, a_p = 0.3 mm [94]

5 Surface integrity

In metal cutting processes, improve the service performance of high-value components is an important field. Surface integrity of the machined components is one of the key factors to ensure the part quality and functional performance, especially for aerospace, marine, and medical industries. With the explanation by Liang et al. [111], machined surface integrity of components can be categorized into three main areas, namely surface topography, microstructural modifications and mechanical properties. Here, literature around four topics (surface roughness, microstructure, microhardness, and residual stresses) within these areas are discussed, with special attention on the influence of edge microgeometries. The thermal-mechanical loads in contact area caused by different edge types have significant effects on machining-induced surface integrity.

5.1 Surface roughness

For final components, surface roughness influences the friction coefficients and adhesion properties of the machined surface. The surface roughness has a strong relationship with the ratio of UCT to cutting edge radius when these two factors are of a similar magnitude.

Based on previous researches, micro edge of cutting tool have a significant influence on the surface roughness and should be studied to facilitate the design of the cutting tool [113, 114]. For honed edge tools, it can be summed up that the surface roughness increases with the increasing edge radius [115]. However, the edge with very small microgeometries could also produce rough surface in some cases, where the tool micro cracks happen due to low wear resistance. Zhao et al. [116] found that the best surface roughness can be obtained with the edge radius of 30 µm in hard turning with CBN tools. As shown in Fig. 31, Ventura et al. [112] studied the effect of microgeometries on surface roughness when machining AISI 4340. It can be noted that the sharp tool can produce the smoothest surface and the surface roughness will increase with an increasing edge radius. Moreover, increasing S_α can positively lower the surface roughness while increasing S_γ can negatively enlarge the surface roughness, which means a smaller K value causes smoother surface. Maiss et al. [117] illustrated the surface roughness map with various cutting edge geometry (see Fig. 32). It can be noted that the lower surface roughness value can be obtained from the area $K < 1$ and the surface roughness value increases with the growth of edge radius ($K = 1$). Opposite law was found by Padmakumar [68] when studying face milling processes, where a tool with larger K factor showed superior surface finish. As shown in Fig. 33, Denkena et al. [118] investigated the effects of cutting edge radius and feed rate on surface roughness. It can be seen that the surface roughness value first decreases ($f < 0.07$ mm/

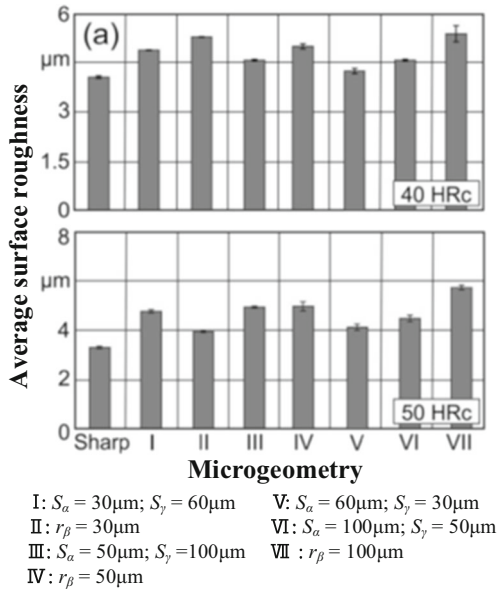

Fig. 31 Surface roughness with different honed edge when machining AISI 4340 at V_c = 200 m/min, f = 0.1 mm/rev, a_p = 0.1 mm [112]

rev) and then rises (f > 0.07 mm/rev) with the growth of feed rate. Increasing edge radius can result in poor surface quality, which is in accord with the experimental results presented by Maiss et al. [117].

When it comes to chamfered edge tools, Karpat et al. [119] noted that the surface machined by 30° chamfer angle tool shows better roughness than the tool with 45° chamfer angle. In the research by Khan et al. [120], the chamfered wiper inserts produced the best roughness compared to the conventional inserts. The superior surface roughness can be achieved in turning Inconel 718 with hone modified chamfered edge PCBN tools [121], which can be illustrated by the fact that edge preparation with honed about 13–18 μm enhances the machinability of the tool. Davoudinejad and Noordin [101] studied the effect of microgeometries of ceramic tools on cutting performance. The authors concluded that the chamfered edge of ceramic tool can produce better surface roughness than honed inserts, especially at low feed rate. Han et al. [122] compared the milling surface roughness between sharp PCD tool and chamfered PCD tool. The surface roughness of the milling workpiece was affected by both edge geometry and PCD grain size. The authors noted that the surface roughness values can be slightly affected by the edge geometry with the PCD grain size 0.5~1 μm and 2~30 μm, while the low surface roughness value can be obtained using the sharp tool with the 25 μm PCD grain size. Kalyan and Samuel [65] studied the effect of chamfer length on the variation of surface roughness as well as feed rate. The value of surface roughness changes significantly at low feed rate while insignificantly at high feed rate. In micro milling processes, no representative work on the effects of chamfer length on surface roughness has been published. Gao et al. [55] studied the milling with different chamfer length tools (0, 5.5 μm, and 15.6 μm), whereas no significant difference between the machined surface roughness can be observed.

The edge preparation also has a significant effect on the surface roughness by changing the edge properties (residual stress and surface roughness) rather than microgeometries. In the study by Wang et al. [97], four symmetry round edge prepared with different methods (unprepared, wet abrasive jet machine, brush, and drag finish) were used to test the cutting performance. The results illustrated that cutting tool manufactured by drag finishing method can induce the best surface roughness with less friction and small tool flank wear.

5.2 Microstructure

The severe thermal and mechanical loads generated on the machined area cause changes in the surface microstructure of material. The recrystallization and strain aging below the

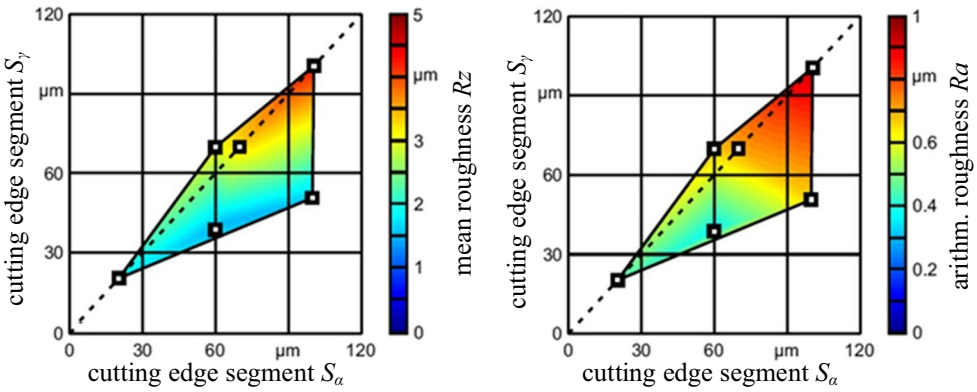

Fig. 32 Surface roughness map with different edge microgeometry [117]

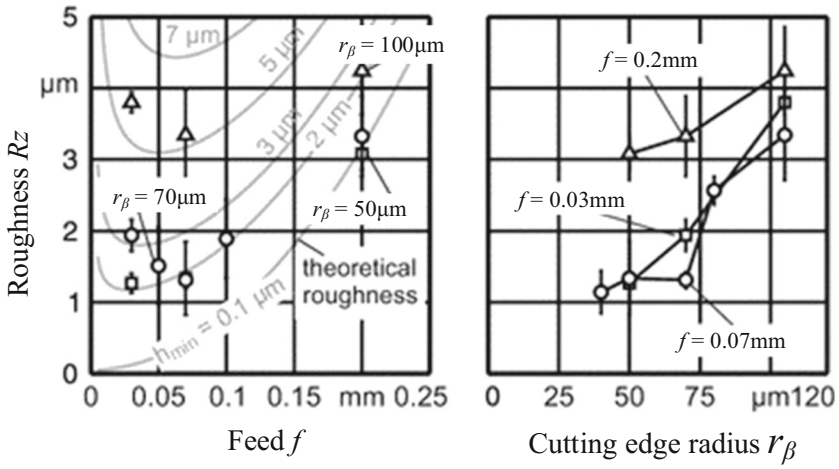

process: hard turning
cutting speed: v_c = var.
feed: f = var.
depth of cut: a_p = 0.1mm
cutting edge radius: r_β = var.

tool: DNMA 150616
coating: Ti(C,N) + Al2O3

material: AISI 52100
hardness: 62HRC

Fig. 33 Effect of feed rate and cutting edge microgeometries on surface roughness [118]

machined surface affect the service function of the components. The deformed layer beneath the machined surface can be divided into three distinct parts. Fig. 34a and b describe the microstructure of Inconel 718 before and after machining. As indicated in Fig. 34b, zone 1 is nanocrystalline layer affected by mechanical-thermal loads, zone 2 is the plastic deformation layer identified by severe bending and elongation of grain boundaries and slip bands, and zone 3 is unaffected layer with undeformed material [123]. Plastic deformation is the first and foremost factor to the surface integrity, and it includes material drags and deformed grains, which can be easily observed under optical and electronic microscope. Cutting edge geometry plays a decisive role in the plastic deformation according to many research studies. However, several studies proposed that though severe plastic deformation was observed on the subsurface layer, no significant alteration with respect to edge microgeometries can be found. [114, 121]. An overview of the machining-induced microstructure is given in this section with special attention on the influence of edge microgeometries.

Zhao et al. [116] explored the effect of cutting tools with edge radius of 20, 30, 40 μm on sub-surface deformation during hard turning AISI 52100 at the cutting speed of 160 m/min, the feed rate of 0.08 mm/rev, the depth of cut of 0.1 mm. It can be seen from Fig. 35 that the deformation layer increases with the growth of edge radius, which can be explained by the deeper ploughed depth and the increasing of plastic strain. Coated tools with larger edge radius of 20~22 μm normally extend the deformation zone to 10~15 μm after turning Inconel 718 at the cutting speed of 250 m/min the feed rate of 0.1 mm/rev [124]. The results shown larger edge radius of coated tools contribute to larger ploughing action and thus result in more severe subsurface deformation like slip lines in the cutting direction, see Fig. 36. Thiele and Melkote [125] observed that large honed tool produced plastic flow in the circumferential direction in turning AISI 52100, while no significant subsurface flow was observed with 22.9 μm and 25.4 μm honed tools. In machining AISI H13 steel, plastic deformation can be observed by metallographic images while milling at V_c = 200 m/min, f_z = 0.2 mm/rev, and the axial and radial depth of cut was kept constant at 1.5 mm. As shown in Fig. 37, the thickness of the plastic deformation layer increased from 2.2 to 3.7 μm when

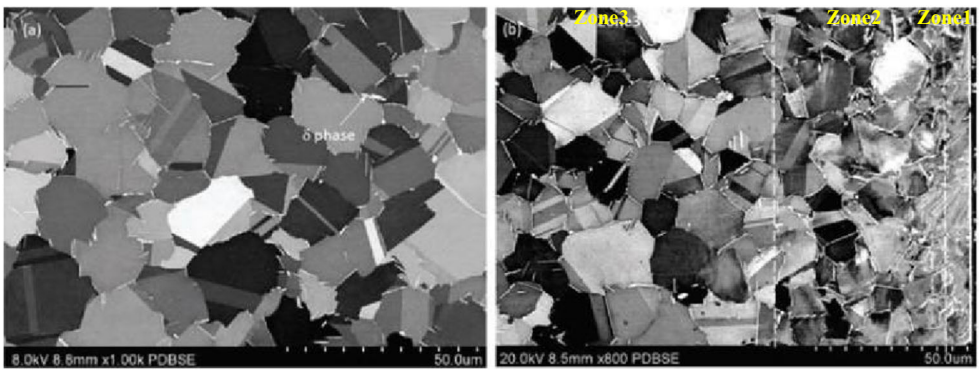

Fig. 34 Microstructure of Inconel 718: **a** before machining; **b** after turning at V_c = 300 m/min, f = 0.2 mm/rev, and a_p = 0.3 mm with ceramic honed edge tools [123]

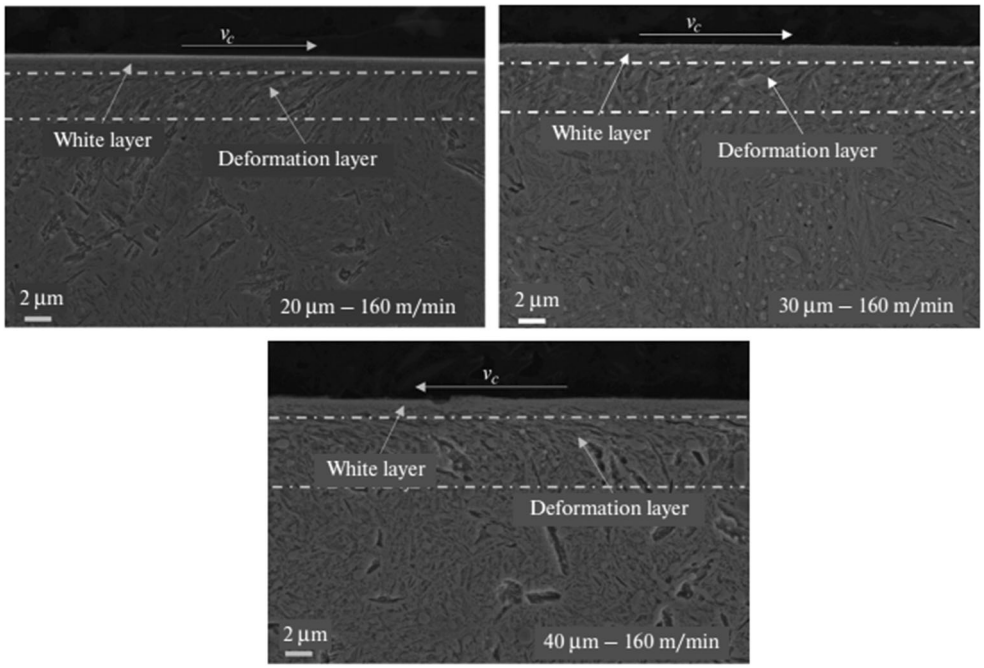

Fig. 35 Deformation layer after turning AISI 52100 at V_c = 160 m/min, f = 0.08 mm/rev, a_p = 0.1 mm with honed edge tools [116]

tool edge changing form sharp to 120 µm honed radius [67]. Similar result was obtained by Li et al. [126] that the depth of plastic deformation layer beneath the machined surface presents an increasing trend with the increase in edge honed radius as indicated in Fig. 38. This phenomenon can be explained by the fact that large edge hone tools result in severe friction between tool flank face and machined surface as well as shear action and plowing. Wyen et al. [127] performed up and down milling of the titanium alloy Ti-6Al-4V using five different cutting edge radius at the cutting speed of 70 m/min, the feed per tooth of 0.08mm/rev, and the cutting width of 25 mm. Cross-sections of surfaces viewed by SEM revealed an increase in plastically deformed surface layer with the growth of cutting edge radius as shown in Fig. 39. It can be concluded from these studies that the plastic deformation layer increases with the cutting edge radius, possibly due to the deeper ploughed depth generated by large edge radius, thus contribute to large friction force and high temperature.

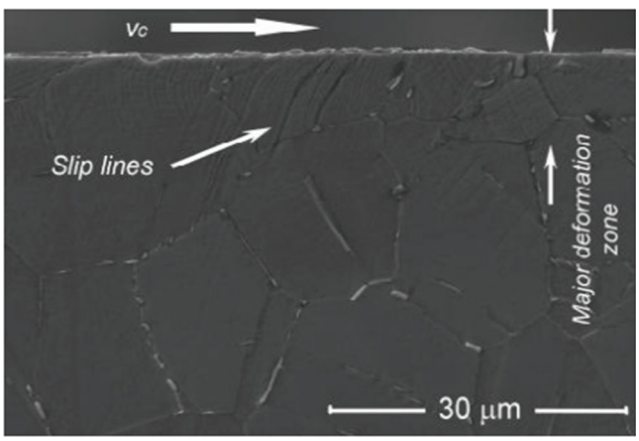

Fig. 36 Slip lines after turning Inconel 718 with large edge radius (20~22 µm) tool at V_c = 250 m/min, f = 0.1 mm/rev [124]

With the consideration of the effects of edge preparation techniques on edge properties, Bordin and Zeilmann [128] evaluated the effect of the cutting tool edge and surface preparation on the surface integrity during dry drilling of AISI P20 steel. Three different edge preparations were obtained: sharp (SH), polished with abrasive brushes (POL) and drag finished (DF). The deformation layer was characterized by the material drag on the hole boundary. It can be observed from Fig. 40 that SH and DF conditions present slightly higher values for the affected layer than the POL condition. This behavior can be associated with the high hole wall temperature, which decreases the material's shear strength, benefiting the plastic deformation. Zeilmann et al. [129] compared the tools in original factory form (OF), drag finished (DF), and polished (POL) when milling of AISI P20 steel at V_c = 180 m/min, f = 0.06 mm/tooth, a_p = 0.5 mm, a_e = 0.2 mm. It can be found that POL tool under dry condition has the highest plastic deformation followed by DF and OF tools (Fig. 41). Their studies showed that the thickness of deformation layer was associated with temperature though no uniform trend of affected layer was found under these edge preparation conditions.

Furthermore, under the combined action of the mechanical and thermal loads, the machined surface layer exhibits different material behavior, which appears white viewed with SEM and optical microscope, hence it is called white layer [130, 131]. These layers are composed mostly of small grain size that is harder and more brittle than that of the bulk material [111]. Previous studies indicated that the mechanism of white layer formation was attributed to the grain refinement induced by plastic deformation, phase transformation induced by

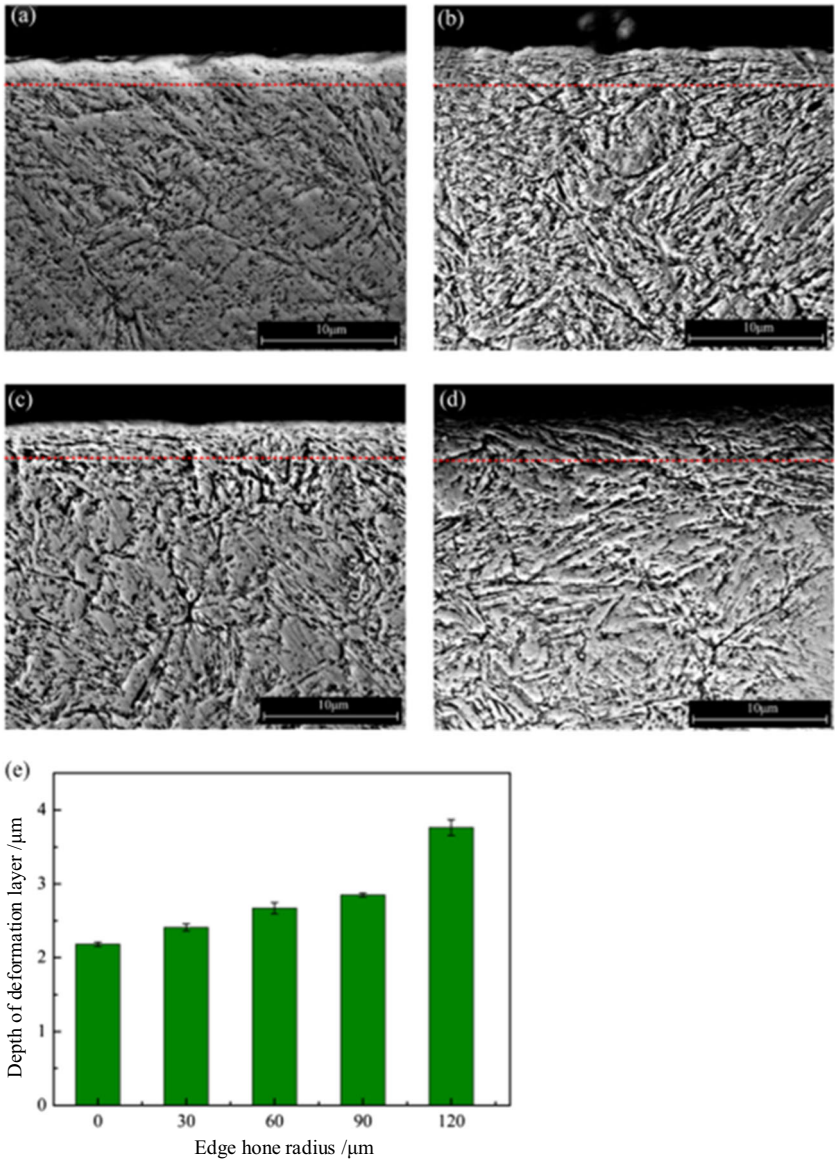

Fig. 37 Deformation layer after milling AISI H13 steel at $V_c = 200$ m/min, $f = 0.2$ mm/tooth, $a_p = 1.5$ mm, $a_e = 1.5$ mm: **a** sharp edge; **b** $r_\beta = 60$ μm; **c** $r_\beta = 90$ μm; **d** $r_\beta = 120$ μm; **e** depth of plastic deformation layer [67]

heating and subsequent cooling of the workpiece material, and the machined surface reaction with the environment. Zhang et al. [132] stated that the thermally driven phase transformation is one of the important reasons for white layer formation as well as the severe plastic deformation, while the former one plays a dominant role in hard turning of AISI 52100 steel [133].

The researches on the effects of cutting edge radius on white layer thickness during hard turning AISI 52100 claimed that the thickness of the white layer increases when the edge radius increase. Denkena et al. [118] concluded that the cutting edge radius had the most significant effect on the occurrence and the thickness of white layer compared to cutting speed and feed rate as shown in Fig. 42. The thickness of white layer increases slightly up to 1.5 μm and 1 μm as feed rate and cutting speed increase to 0.2 mm and 300 m/min, respectively. It can also be noted that increasing the cutting edge radius from 40 to 105 μm leads from no white layer to a very constant layer thickness of more than 5 μm. Additionally, Zhao et al. [116] found that the depth of deformation and white layer increased as the cutting edge radius, and this may be attributed to plastic strain. Figure 43 reveals the influence of cutting edge radius and cutting speed on the thickness of deformation layer and white layer. It is observed that the machined surface produced by CBN tools in three groups of edge radius are formed with white layer and deformation layer, which is substantial when the tool with edge radius of 40 μm was employed, but there is almost no difference between edge radius of 20 μm and 30 μm.

Another research performed by Thiele et al. [134] compared effects of sharp, chamfered, and honed edge on white layer formation during finish hard turning process, in which

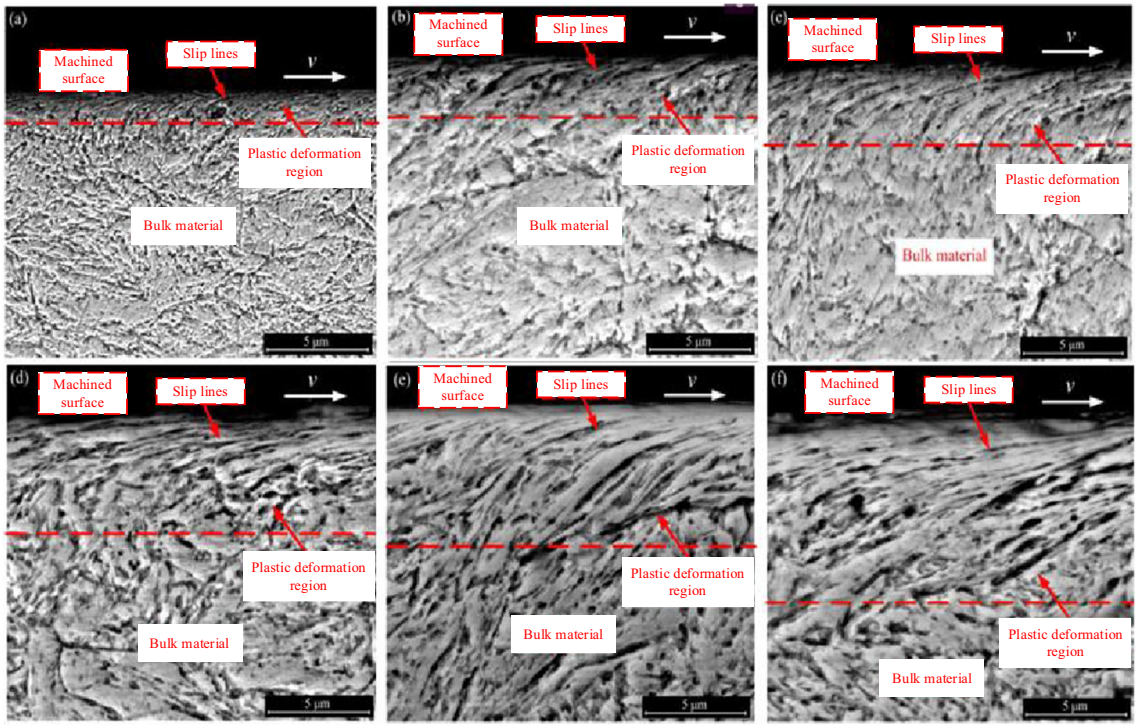

Fig. 38 Microstructure under different cutting edge radius after milling AISI H13 steel at $V_c = 200$ m/min, $f = 0.2$ mm/tooth, $a_p = 1.5$ mm, $a_e = 1.5$ mm: **a** sharp edge; **b** $r_\beta = 30$ μm; **c** $r_\beta = 60$ μm; **d** $r_\beta = 90$ μm; **e** $r_\beta = 120$ μm; **f** $r_\beta = 150$ μm [126]

the workpiece material was the same as that in refs. [116, 118]. Figure 44 illustrates three basic microstructural patterns including continuous white layers, intermittent white layers, and dark layers. It can be concluded that large honed edge tools produce continuous white layer at all feed rate and workpiece hardness values, small honed edge tools mostly lead to over-tempered layer, and the chamfered edge tools result in different deformed layers depending on the cutting parameters. Dark layer was also observed when dry turning AISI O1 tool steel using coated ceramic tool [135]. Zhang and Zhuang [136] predicted the white layer based on 2D finite element analysis applying the phase transition mechanism with the consideration of the combined effects of stress and strain, and found that large honed edge and large chamfered edge can contribute to white layer formation. Their studies suggested that both phase transformation and plastic

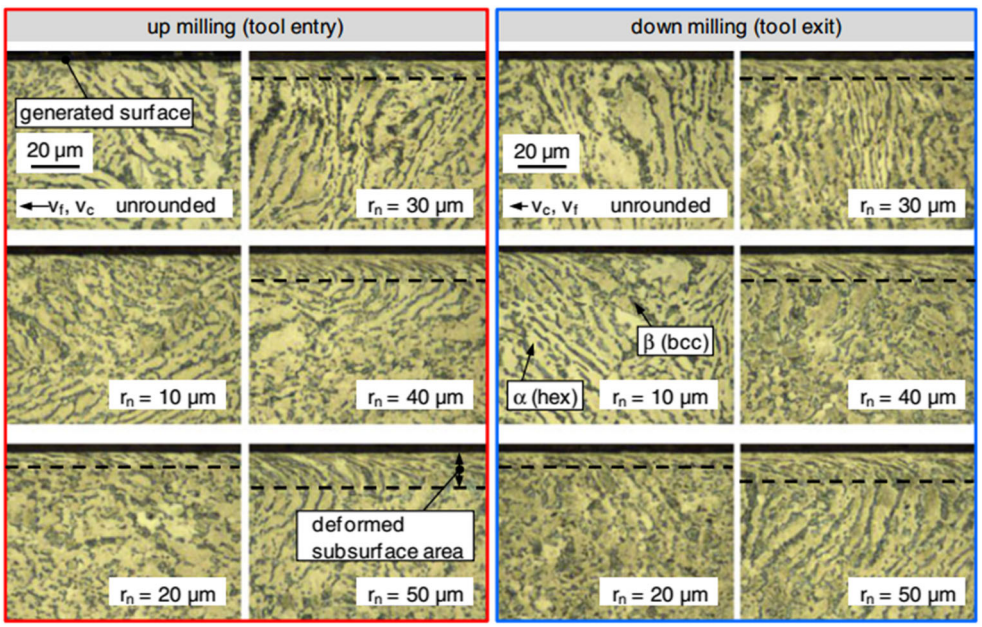

Fig. 39 Subsurface deformation layer after milling Ti6Al4V with rounded edge tools at $V_c = 70$ m/min, $f = 0.08$ mm/tooth, $a_p = 4$ mm, $a_e = 25$ mm [127]

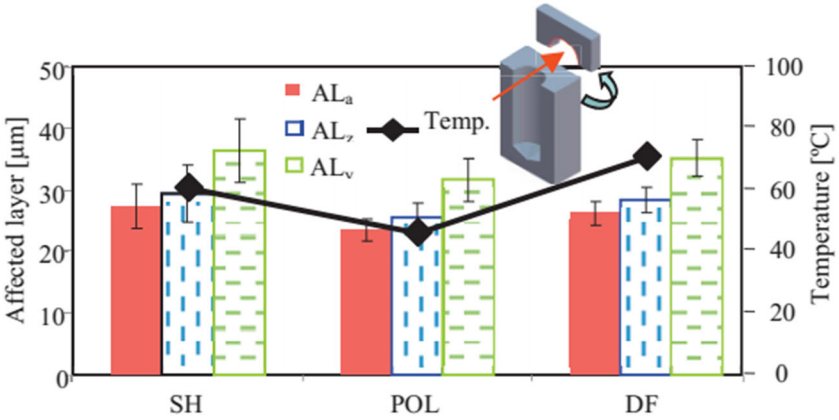

Fig. 40 Affected layer after drilling of AISI P20 steel V_c = 40 m/min, f = 0.1 mm/rev with different edge preparation [128]

deformation could result in white layer, and the increased honed edge as well as the chamfered edge contributed to the thickness of white layer.

Li et al. [67] found neither a white layer nor phase transformation occurs in the machined surface of AISI H13 after hard milling employing tools with different edge radius. Additionally, Burhanuddin et al. [114] concluded that the layer softening occurred rather than the hard white layer after dry cutting of Ti-6Al-4V alloys with chamfered and honed tools.

Besides, previous studies indicated that microstructure characteristics twins, dislocations or their combination could result in dynamic recrystallization, which induced severe grain refinement [137–141]. The grain size alterations and the bending and elongation of grain boundaries and slip bands are momentous indicators of severe plastic deformation [142–144], and the edge geometries of cutting tools play a significant role in the deformation. Arisoy and Özel [145] investigated the effect of cutting edge geometries on the grain size and distribution in IN100 after face turning at a constant depth of cut of 1 mm. The microstructure of IN100 alloy consists of γ and γ′ phases, in which primary γ′ and secondary γ′ sizes were measured in this research. The distribution of primary γ′ and secondary γ′ grain sizes are given in Fig. 45. And the effect of cutting edge geometries on grain size and volume fractions indicated that sharp edge tool yields the highest value of primary γ′ grain size, followed by the tools with edge radius of 25 µm, 10 µm, and TiAlN coated tool respectively (Fig. 46). However, these trends are reversed for secondary γ′ grains. Moreover, the volume fractions of secondary γ′ phase are much higher than the primary γ′ at all tool types, and uncoated WC/Co tools with edge radius of 25 µm produce the highest volume fraction in secondary γ′ phase, whereas the lowest in primary γ′ ' . Same cutting tools were used when turning Ti6Al4V alloy [145]. The results noted that the sharp tool generated smaller grain sizes at V_c = 55 m/min, f = 0.05 mm/rev, a_p = 2 mm, and all tools resulted in less grain refinement at V_c = 90 m/min.

Jafarian et al. [146] indicated that increasing the edge radius and chamfer angle resulted in decreasing the grain size, where chamfered edge tools show more obvious trend. During the orthogonal cutting of Inconel 718 with V_c = 70 m/min and f = 0.1 mm/rev, respectively, and the tool edge geometry was varied at different levels. The fact of the grain refinement generally accompanies with the increase of microhardness on surface as given in Fig. 47. As a result of this event, larger geometry characteristic of tool edge induces

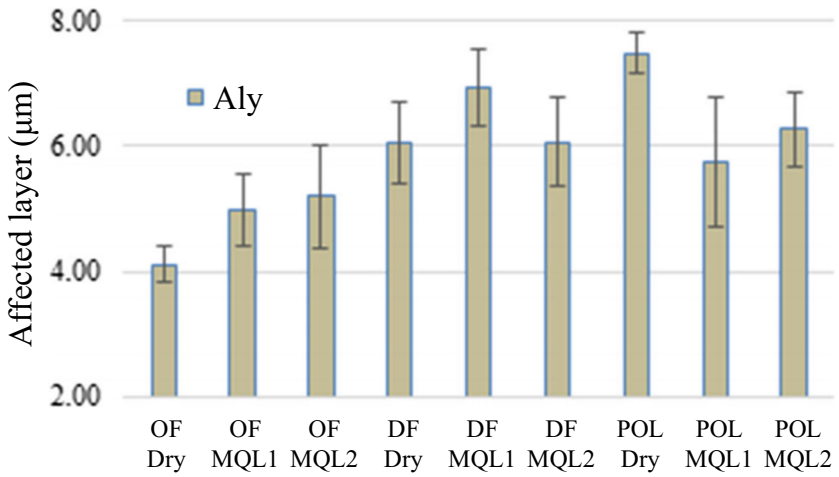

Fig. 41 Plastic deformation layer after milling of AISI P20 at V_c = 180 m/min, f = 0.06 mm/tooth, a_p = 0.5 mm, a_e = 0.2 mm with different cutting edge preparation [129]

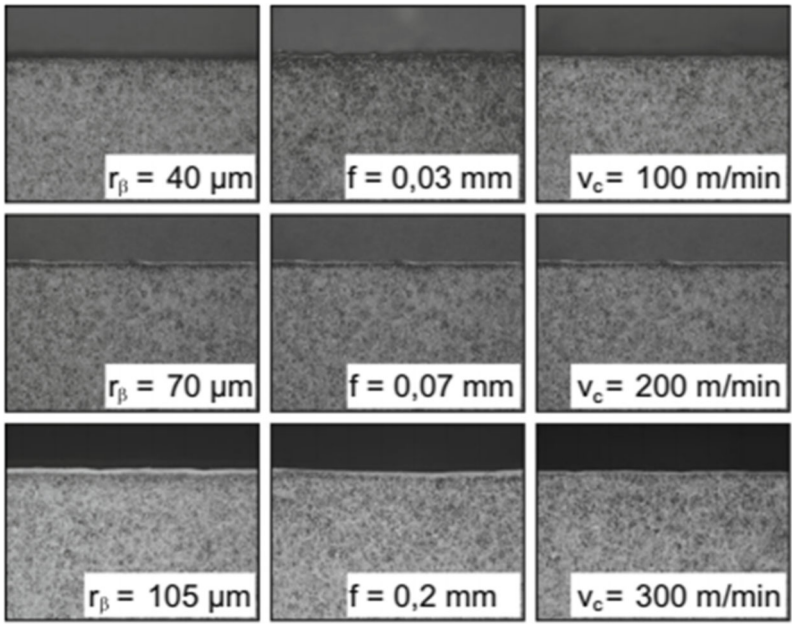

Fig. 42 Influence of cutting parameters on white layer when turning AISI 52100 [118]

higher mechanical contact between the tool and the workpiece, thus results in more severe grain refinement. Gerstenmeyer et al. [147] examined the influence of cutting edge geometries (form-factor K), surface modification velocity and penetration depth on process forces, maximal temperatures, and resulting grain size during the mechanical surface modification by complementary machining of AISI 4140 and Armco-Iron. Seen from Fig. 48, larger form-factor K causes smaller grain size either at a constant penetration depth or surface modification velocity. It can be concluded under the given cutting parameters form-factor $K > 1$ generates higher temperature than $K < 1$, consequently leads to smaller grain size. Apart from grain size prediction, the layer affected by the recrystallization was conducted by Segebade et al. [83, 148] when turning Ti6Al4V at V_c = 160 m/min, f = 0.1 mm/rev and broaching AISI 4140 at cutting speed V_c = 75 m/min and cutting depth h = 54 µm respectively, and found that smaller form-factor leads to an even deeper grain refined layer.

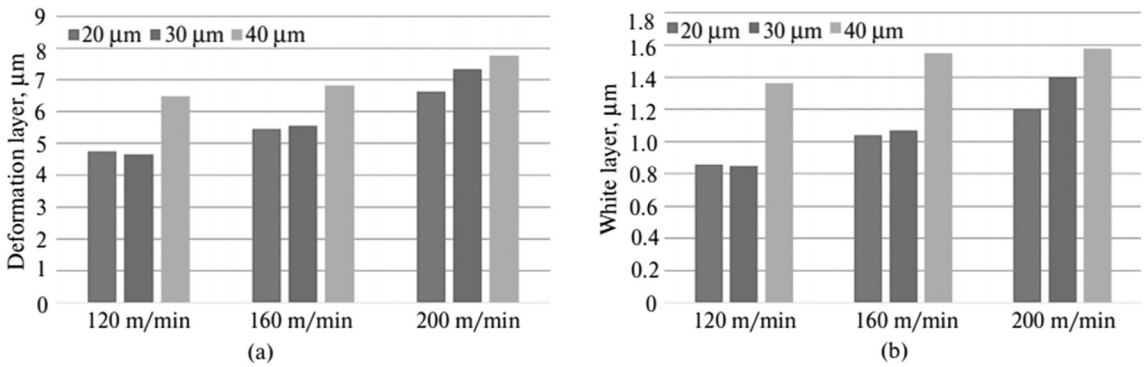

Fig. 43 Effect of edge radius on the depth of deformation (**a**) and white (**b**) layers (f = 0.08 mm/rev, a_p = 0.1 mm) [116]

Factor Level Combination			Stress Component		Microstructure	d_0 [Å]
Hardness [HRC]	Edge Prep [μm]	Feed Rate [mm/rev]	Axial [MPa]	Hoop [MPa]		
57	22.9 Hone	0.05	-252	11	Over-Tempered Layer	1.1707
57	22.9 Hone	0.10	10	118	Over-Tempered Layer	1.1706
57	22.9 Hone	0.15	146	319	Small Intermittent White Layers	1.1706
57	121.9 Hone	0.05	-530	35	Continuous White Layer	1.1706
57	121.9 Hone	0.10	-642	-633	Continuous White Layer	1.1705
57	121.9 Hone	0.15	-377	-286	Continuous White Layer	1.1704
57	25.4 Chamfer	0.05	-594	-306	Over-Tempered Layer	1.1702
57	25.4 Chamfer	0.10	-407	-368	Large Intermittent White Layers	1.1706
57	25.4 Chamfer	0.15	-232	-48	Continuous White Layer	1.1706
41	22.9 Hone	0.05	94	73	No Visible Change	1.1702
41	22.9 Hone	0.10	121	38	Over-Tempered Layer	1.1704
41	22.9 Hone	0.15	355	168	Over-Tempered Layer	1.1704
41	121.9 Hone	0.05	-406	57	Continuous White Layer	1.1703
41	121.9 Hone	0.10	-282	-228	Continuous White Layer	1.1703
41	121.9 Hone	0.15	-275	-551	Continuous White Layer	1.1702

Fig. 44 Microstructure pattern of AISI 52100 after turning with different edge geometries tools [134]

5.3 Microhardness

In response to the machining-induced deformations on the surface and subsurface, work hardening layer was formed under excessive strain loading, creating the reduction of the plasticity of the workpiece and making it extremely difficult for the sequential cuts [111, 130]. The plastic deformation caused by high mechanical and thermal effects results in grain refinement and microhardness improvement of the surface layer. The hardness in the vicinity of the machined surface is generally higher than the hardness in the deeper machined surface [120, 149–151], while the results are sometimes reversed due to the thermal softening effects [114, 142, 152]. The microhardness and the hardness penetration depth of the machined material are affected by the edge geometry significantly. On the one hand, the effect of cutting edge radius on surface hardness and work hardening have been studied by many researchers, and they found that larger edge radius leads

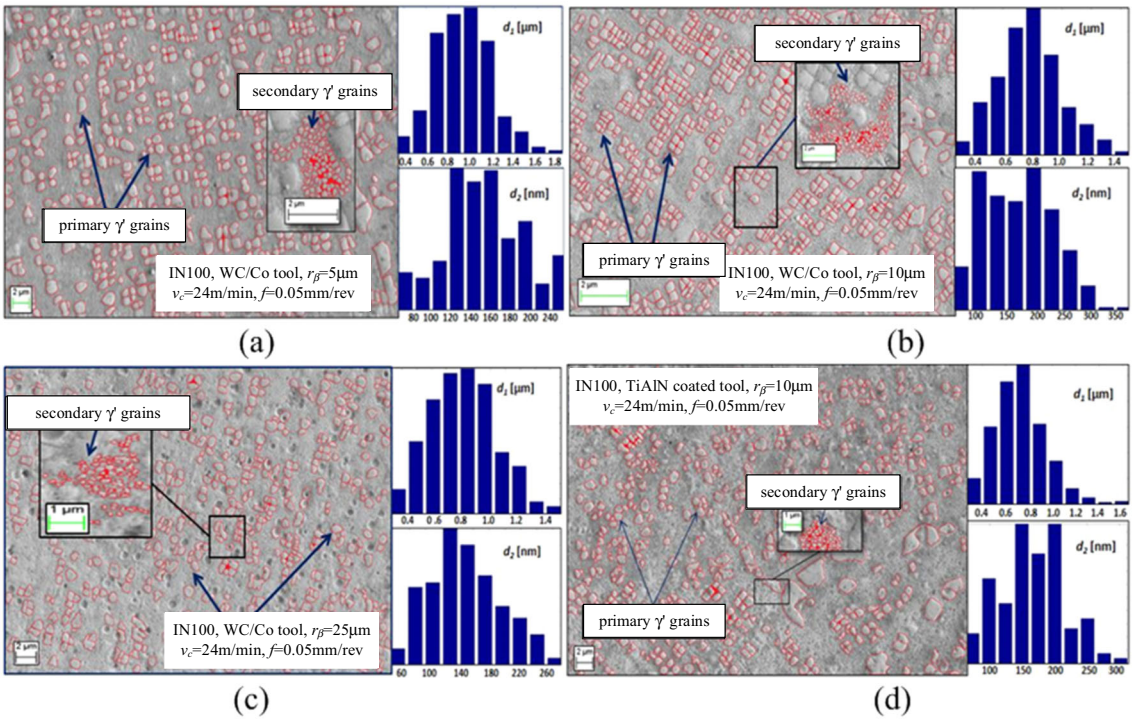

Fig. 45 Subsurface microstructure of machined IN100 (V_c = 24 m/min, f = 0.05 mm/rev), histograms of primary γ′ (d_1), and secondary γ′ (d_2) grains. **a** WC/Co, sharp; **b** WC/Co, r_β = 10 μm; **c** WC/Co, r_β = 25 μm; **d** TiAlN coated, r_β = 10 μm [145]

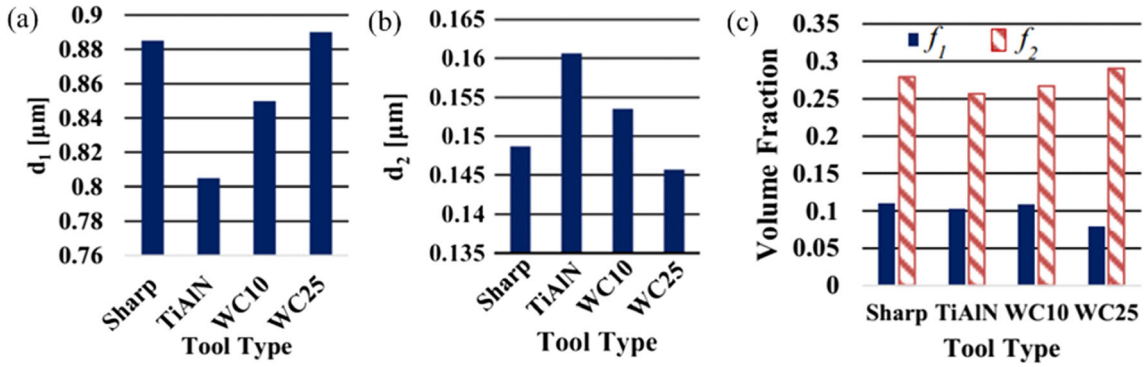

Fig. 46 Effect of edge radius on the **a** primary and **b** secondary γ′ grains, and on the **c** grains volume fractions when turning Ti6Al4V alloy at V_c = 55 m/min, f = 0.05 mm/rev, a_p = 2 mm [145]

to higher microhardness. Arısoy et al. [153] revealed that largest edge radius tools r_β = 25 µm produced highest microhardness after turning Inconel 100 at V_c = 12~24 m/min, f = 0.05 mm/rev, and a_p = 1 mm, and the high hardness layer is about 25 µm (see Fig. 49). Similar results were obtained in Fig. 50 after turning Ti6Al4V at higher cutting speed of V_c =v55~90 m/min with one exception [145]. According to ref. [67], cutting tools with r_β = 120 µm generate higher microhardness than those with r_β = 60 µm and sharp edge tools after milling AISI H13 steel. It can be observed from Fig. 51 that the nanohardness of the machined surface is much higher than the values of the subsurface, which is attributed to the work hardening induced by shear plastic strain, and the depth of affected layer is very thin approximately less than 10 µm. The higher hardness of the surface layer than that of the bulk material can also be found in ref. [139], and it could be because of the plastic deformation [132, 154]. In addition, a combination of reduced thermal softening effect and greater refinement might result in a higher surface hardness in the machined surface [143]. Another research on AISI 52100 showed an increase of the surface hardness in axial direction from 720$HV_{0.025}$ (r_β = 50 µm) to 900$HV_{0.025}$ (r_β = 105 µm) during hard turning process at constant values of f = 0.07 mm/rev and a_p = 0.1 mm (see Fig. 52). Moreover, the hardness profiles illustrate that the depth of affected zone varies from 50 to 100 µm and the area beneath the surface gets softer along the depth [118].

On the other hand, several researchers have studied the effect of chamfer edge tools on the surface hardness and the depth of work hardening layer. Jafarian et al. [146] found that microhardness on the surface increased with the chamfer angle and hone radius during the orthogonal cutting of Inconel 718 alloy at a fixed cutting speed of 70 m/min and feed rate of 0.1 mm/rev, while this trend was more intensive for chamfered tools. Besides, the cutting edge geometry did not give an obvious effect on the depth of affected layer and the value of chamfered tools (250 µm) is significantly higher than that of the honed edge tools (125~150 µm). In turning metastable austenitic steel AISI 347 at V_c = 30 m/min, f = 0.15 mm/rev, a_p = 0.2 mm, Hotz and Kirsch [155] noted that increasing the cutting edge radius and chamfer angle the α′-martensite content increased, consequently leading to an increase in mico hardness. Figure 53 reveals that large edge radius contibuted to a more pronounced hardening of the workpiece, and the increased chamfer angle leads to an increase in maximum microhardness and the hardness penetration depth. Zhuang et al. [156] studied the effect of chamfered only tools on the surface microhardness and depth of work hardening layer during turning Inconel 718 at V_c = 150 m/min, f = 0.05~0.2 mm/rev, and found that the thickness of work hardening layer is about 60~80 µm, the machined surface microhardness is 1.2 times that of the bulk material and the chamfer length had a more significant influence on the work hardening thickness than the chamfer angle.

In addition, the microhardness induced by chamfer plus hone edge tools has been compared with chamfered or honed only tools. In machining Inconel 718, the chamfered plus

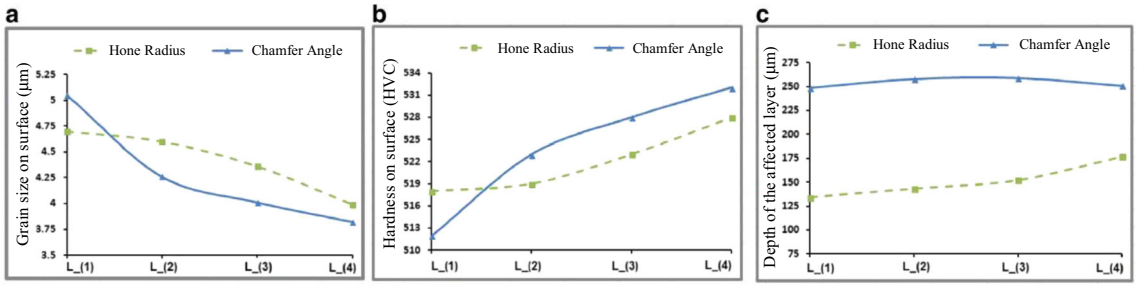

Fig. 47 Effect of cutting edge geometry on **a** grain size on surface, **b** hardness on surface, and **c** depth of the affected layer after turning Inconel 718 at V_c = 70 m/min and f = 0.1 mm/rev [146]

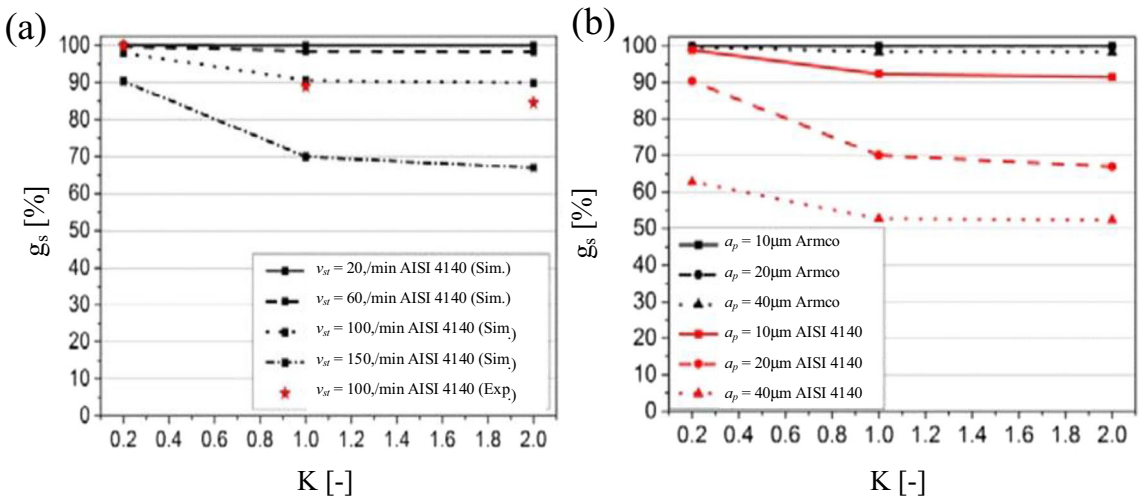

Fig. 48 Grain size g_s under the condition of **a** constant penetration depth of 20 µm; **b** surface modification velocity of 150 m/min [147]

honed cutting edge geometry(CH) induces the highest microhardness in the machined subsurface compared to other chamfered cutting edges CW1 (30° chamfer angle) and CW2 (20° chamfer angle) at V_c = 125~475 m/min, f = 0.05~0.15 mm/rev, a_p = 0.5~1 mm, and the depth of the machining affected zone (MAZ) reaches up to 200 µm for most of the experimental conditions (see Fig. 54) [157]. It can also be seen from Fig. 54 that 30° chamfered edge tool generates the lowest microhardness. The trend is the same as degree of work hardening (DWH) measured in the machined subsurface up to a depth of 50 µm, as shown in Fig. 55. This could be explained by the ploughing effect induced by honed edge. Mayer et al.

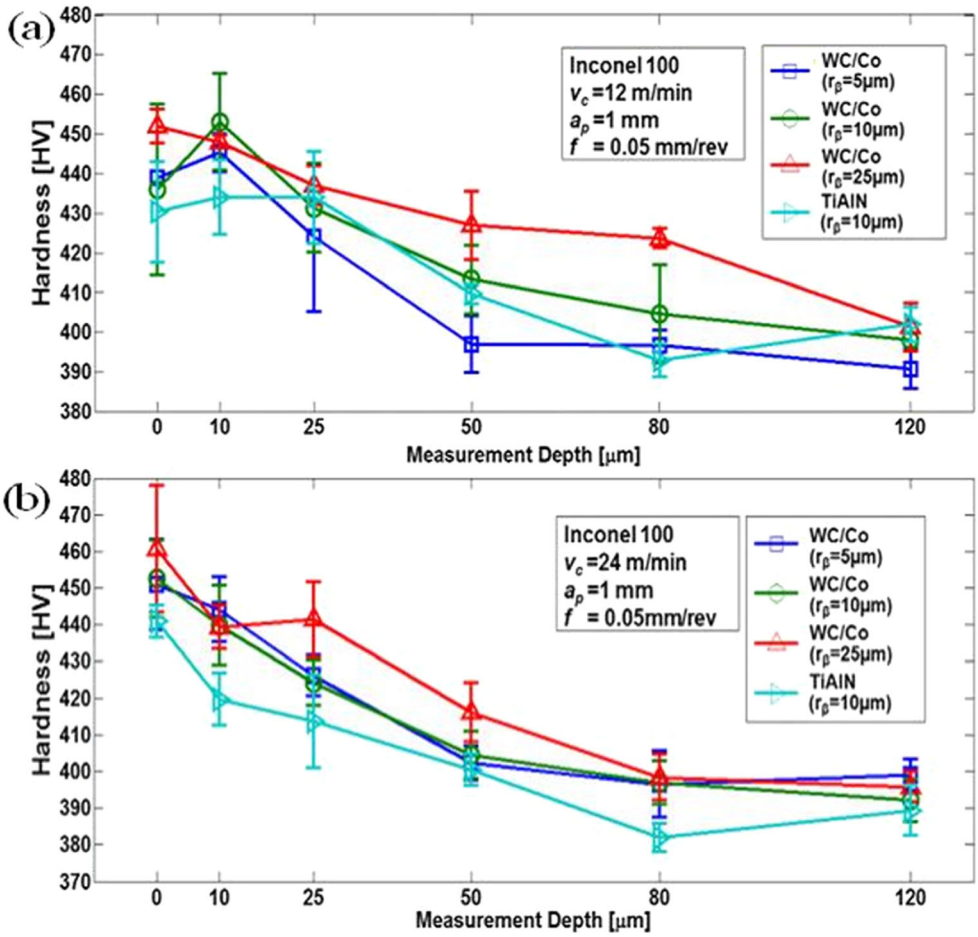

Fig. 49 Microhardness profiles for different honed edge tools after turning Inconel 100 at **a** V_c = 12 m/min and **b** V_c = 24 m/min [153]

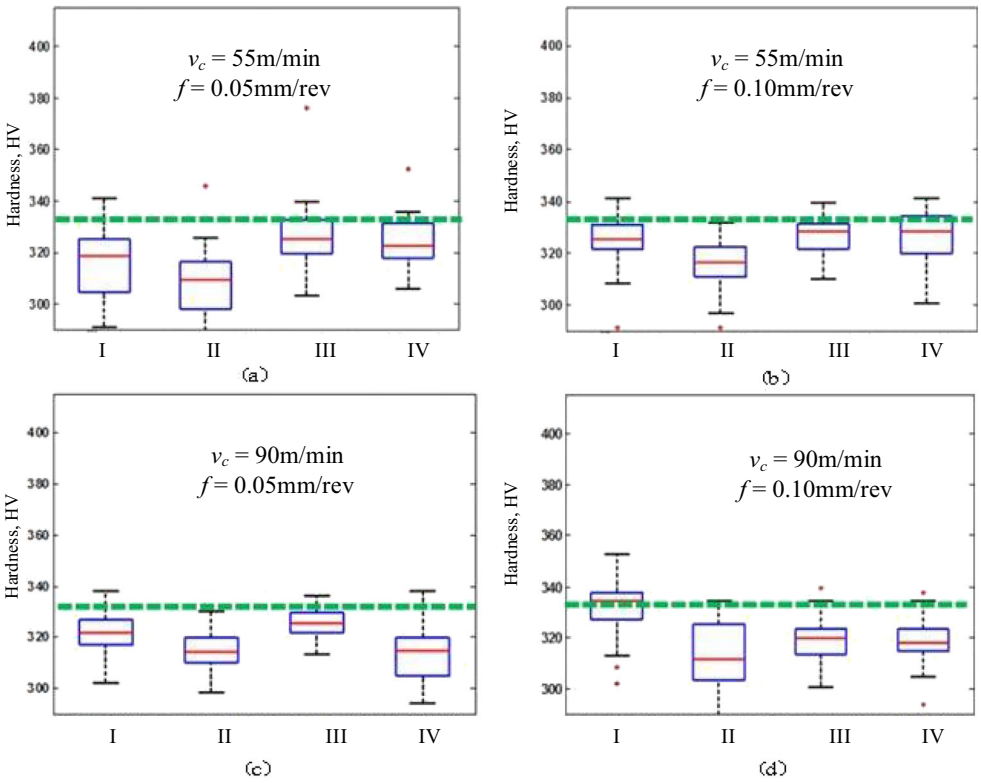

Fig. 50 Effect of cutting edge radius on the microhardness after turning Ti6Al4V: I: uncoated WC/Co r_β = 5 μm; II: uncoated WC/Co r_β = 10 μm; III: uncoated WC/Co r_β = 25 μm; IV: TiAlN WC/Co r_β = 10 μm [145]

[13] assessed the values of microhardness by the amount of α′-martensite when turning AISI 347 and found the higher was the hardness the more α'-martensite was formed. Figure 56 reveals that insert 1 with chamfered and honed edge result in highest fraction of α′-martensite compared to tools with no chamfered edge, and the amount of martensite increased as the edge radius, which means chamfer plus hone edge tools create highest values of microhardness followed by edge radius of 70 μm and 55 μm. The hardened layer induced by phase transformation can also be found in [158] after turning hardened steel 16MnCr5. Other hardening effects like increase of dislocation density as well as the formation of twins and nano grains might contribute to the surface hardening [13, 137]. Sarnobat et al. [159] investigated the effect of light honed (15° chamfer angle), standard honed (25°chamfer), and heavy honed (35° chamfer angle) tools on the microhardness when turning AISI D2 steel at V_c = 60~120 m/min, f = 0.05~0.16 mm/rev, a_p = 0.1~0.35 mm, which noted the nano hardness increased to about 4~9.5 GPa and lighter honed tools had less influence on work hardening.

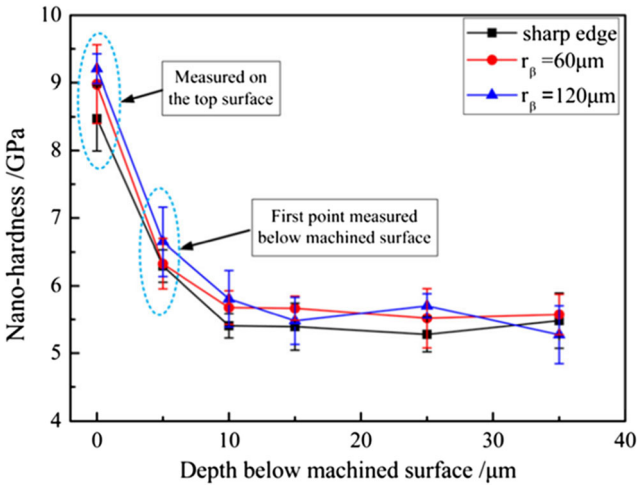

Fig. 51 Nano-hardness profiles of machined surface for AISI H13 with honed edge tools (V_c = 250 m/min, f = 0.2 mm/tooth, a_e = a_p = 1.5 mm) [67]

In some specific conditions, the microhardness profiles induced by different edge microgeometries have no uniform trend. Burhanuddin et al. [114] found the edge geometry (chamfered, honed) had insignificant effects on the hardness of the machined surface during the turning process for Ti6Al4V alloys at either low or high cutting conditions. For these materials, similar result was acquired by Wyen et al. [127] in down milling. These studies show that large honed or chamfered only tools can create severe work hardening on the machined surface, and chamfer plus hone edge tools have a more significant influence than honed only and chamfered only tools. Additionally, the surface microhardness generally increases with the increasing edge radius and chamfer angle.

5.4 Residual stresses

Residual stress is referred to the stress that remains in the workpiece material after the external loading is removed,

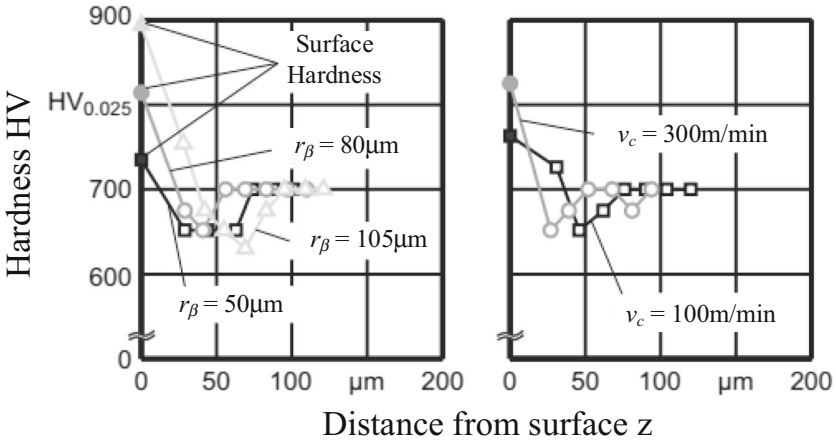

process: hard turning
cutting speed: v_c = var.
feed: f = 0.07mm
depth of cut: a_p = 0.1mm
cutting edge radius: r_β = var.
tool: DNMA 150616
coating: Ti(C,N) + Al_2O_3
material: AISI 52100
hardness: 62HRC

Fig. 52 Affected microhardness of machined surface for AISI 52100 [118]

and its value reflects the sum of macrostresses that retain on the machined surface [160]. Residual stress significantly influences the service performance of componernts such as corrosion resistance and fatigue life [154], thus it can be used to evaluate overall structural resilience of the component and its propensity of fatigue failure in-service [161]. Previous studies have concluded that the mechanical loads tend to generate compression residual stress, while the thermal loads generally produce tensile residual stress. High temperature, higher cutting forces, and strain rate will accelerate the development of residual stress and the depth of stress distribution beneath the machined surface [162, 163]. It has been found that compression residual stresses usually contribute to the fatigue life, creep behavior and crack propagation resistance [164], while the effects of tensile residual stresses are usually adverse [144]. Hence, it is necessary to prevent tensile residual stresses from occurring during machining processes [130, 165]. The stress sources and heat sources for workpiece during cutting process are the same, that is, the primary shear zone and tool-workpiece interface, which usually is sensitive to edge microgeometries. Since the generation of residual stresses is determined by stress-strain and thermal load histories, this section reviews the researches about the effects of edge microgeometries on residual stress profiles.

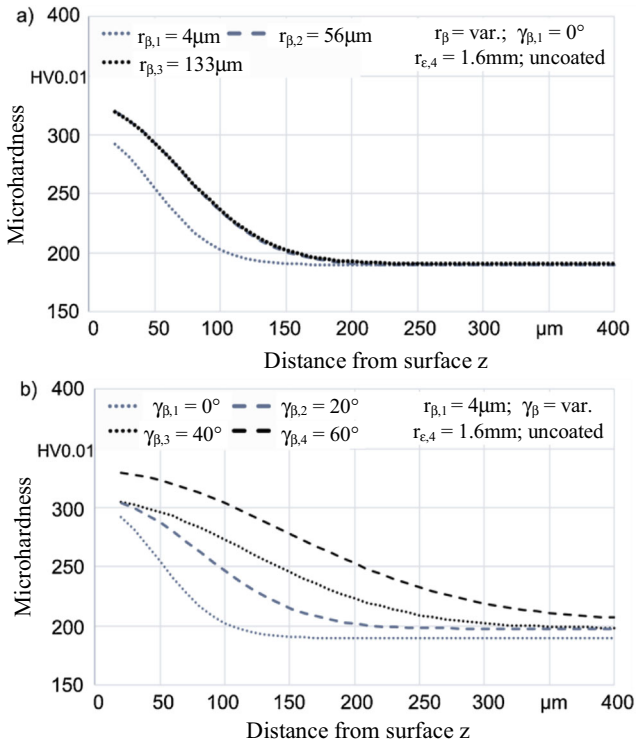

Fig. 53 microhardness profiles when employing different **a** edge radius and **b** chamfer angles after turning AISI 347 at V_c = 30 m/min, f = 0.15 mm/rev, a_p = 0.2 mm [155]

On the one hand, honed edge tools generate compressive residual stress and it increases with the edge radius. Denkena et al. [118] performed the turning experiments of AISI 52100 to investigate the effect of edge radius on the residual stress. It is believed that large edge radius is useful to create large compression residual stresses at V_c = 200 m/min, f = 0.07 mm/rev, a_p = 0.1 mm, and with the increasing edge radius the affected surface layer gets thicker. It can be found from Fig. 57 that the maximum compressive stresses for both peripheral and axial directions increase from 570 MPa (r_β = 40µm) to 1050 MPa (r_β = 105 µm). This phenomenon could be correlated with the high passive forces caused by large cutting edge radius. The passive forces lead to high mechanical loads on the subsurface area, which further result in compressive residual stresses. Wyen et al. [127] studied the influence of the cutting edge radius on residual stress of the surface

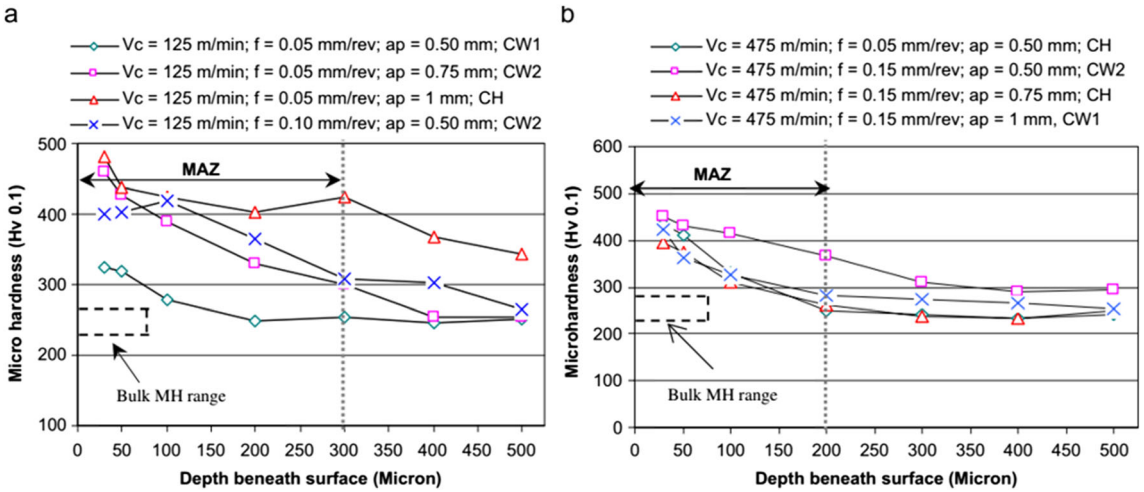

Fig. 54 Microhardness profiles for edge geometry (CW1; CW2; CH) after turning Inconel 718 at **a** V_c = 125 m/min and **b** V_c = 475 m/min [157]

and near surface area in up and down milling for Ti6Al4V. Figure 58 depicts that the maximum compressive residual stress on the surface increases with the growth of cutting edge radius from around 310 MPa (r_β = 6 μm) to approximately 600 MPa (r_β = 50 μm), whereas no uniform trend is observed in down milling. On the contrary, the maximum compressive stresses decrease with the increase of edge radius in turning Ti6Al4V, which can be attributed to the low thermal conductivity of the workpiece material [166]. Moreover, Fig. 59 reveals that surface compressive residual stress increases but the depth of maximum compressive stress and the influencing range of machining induced residual stress decrease with the change of edge radius from 0.01 to 0.03 mm. In another study during turning porous tungsten, researchers found a steep growth in compression residual stress from edge radius of 2 μm to 5 μm, and the stresses slightly increase with the edge radius for dense polycrystalline tungsten. However, the compressive residual stress decreases with the edge radius for porous tungsten and the absolute value is lower (see Fig. 60), which could be explained by shear machining in dense polycrystalline tungsten and fracture machining in porous tungsten [167]. In machining 16MnCrS5 at V_c = 200 m/min, f = 0.1 mm/rev, and a_p = 0.1 mm, symmetrical and asymmetrical edge roundings were discretized by several chamfers, as a result the contact length was used to indicate the tool edge geometry and to assess the induced residual stress [63]. Figure 61 reveals that longer contact length increases the subsurface maximum compression residual stress σ_{max} but decreases the surface compressive stress σ_o, and it could increase the depth of subsurface maximum compressive residual stress Z_{max} as well as the subsurface affected zone Z_t.

Other researchers have compared the mechanical properties induced by the sharp and hone edge tool, and they concluded that honed tools performed better than the sharp edge tools. Coelho et al. [121] and Li et al. [67] explored the residual stress using sharp and honed tools when turning Inconel 718 at V_c = 500 m/min, f = 0.1 mm/rev, a_p = 0.35 mm, and milling AISI H13 steel at V_c = 250 m/min, f_z = 0.2 mm/tooth, a_p = 1.5 mm, and found that the honed edge generated compressive residual stresses and the values were higher than the sharp edge tool. Nespor et al. [168] compared the effect of edge geometry on residual stress after machining Ti6Al4V using the complex ball end milling process as well as the fundamental orthogonal turning and planing process. It can be concluded that superficial residual stresses in cutting direction σ_2 increase with the increased edge radius both in ball end milling and orthogonal turning processes, and the absolute values are higher for turning than for planing (Fig. 62). In

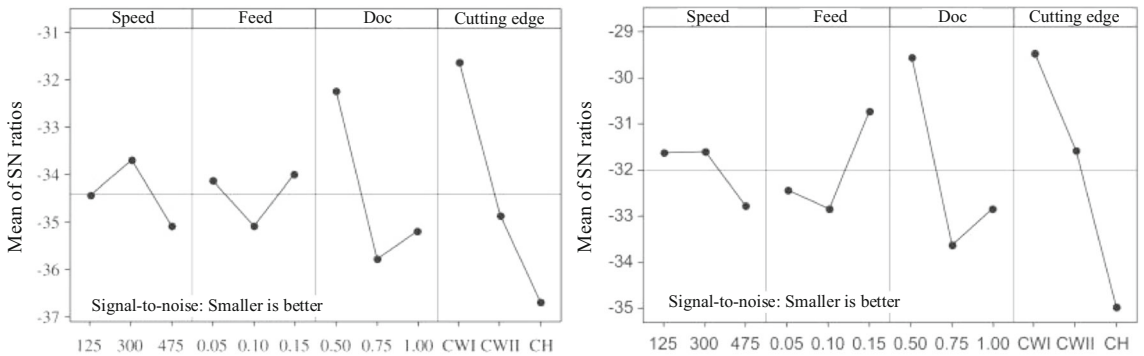

Fig. 55 Main effects for DWH (%) at **a** 30 μm and **b** 50 μm depth [157]

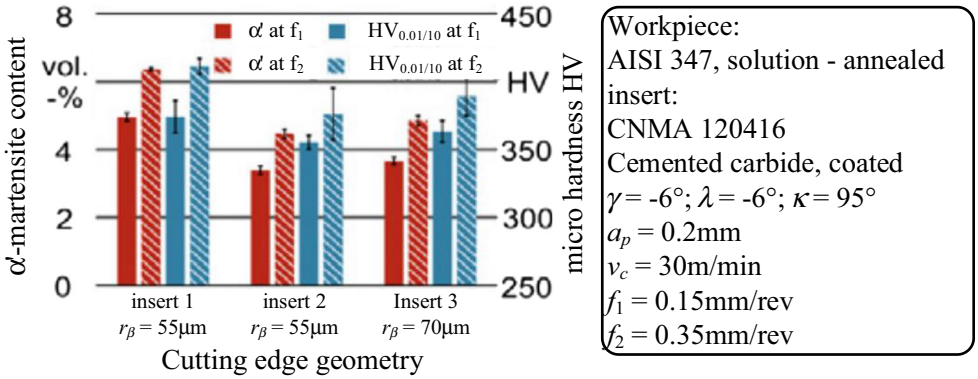

Fig. 56 The effect of cutting edge geometry on the α′-martensite content of machined AISI 347 surface at f_1 = 0.15 mm/rev and f_2 = 0.35 mm/rev [13]

addition, honed edge tools could lead to tensile residual stress reported by several studies. Bushlya et al. [124] found coated PCBN tools with larger edge radius of 20 µm generates compressive residual stress up to 600 MPa, whereas the uncoated ones generate higher values of compression residual stress and present a tendency of transition from compression to tensile surface residual stresses. They also found that coated tools have a thicker affected layer (~ 120 µm) than uncoated tools (~ 100 µm). Ozel and Ulutan [169] compared the effect of cutting edge radius on the residual stress profiles when turning Ti6Al4V and IN100. In the radial direction, all tests for Ti6Al4V generate compressive residual stresses both at the surface and deep into the material, while the stresses in the circumferential direction show tensile at the surface and become compressive gradually(see Fig. 63a). For IN 100, it shows that surface tensile stresses increase with the cutting edge radius for both circumferential and radial directions, and the maximum compressive residual stresses vary from 400 to 600 MPa (see Fig. 63b). The forces and frictions between tool and workpice result in mechanical load, and further lead to compression residual stress, hence the contact area between tool and workpiece plays a decisive role in formation of residual stress [170]. The normalized ploughing zone considering the undeformed chip thickness as well as the contact length was used to analyze the influence of edge geometry on the residual stress during slot milling of 42CrMo4-QT steel [109]. As seen from Fig. 64, high tensile residual stresses up to 350–400 MPa occur as A′α increases by the variation of the hone design.

On the other hand, residual stress induced by chamfered tools has been investigated and compared to that generated by honed tools. In machining bearing steel AISI 52100, Hua et al. [90] demonstrated that the maximum compressive residual stress increased with cutting edge radius and chamfer angle, and the increase was significantly larger when chamfer angle changes from 0° to 20° than that from 20° to 30°. It can be noticed from Fig. 65 that the compressive residual stress in circumferential direction is much larger than that in axial direction and the depth of maximum compressive stress remains almost unchanged. Paschoalinoto et al. [171] concluded that

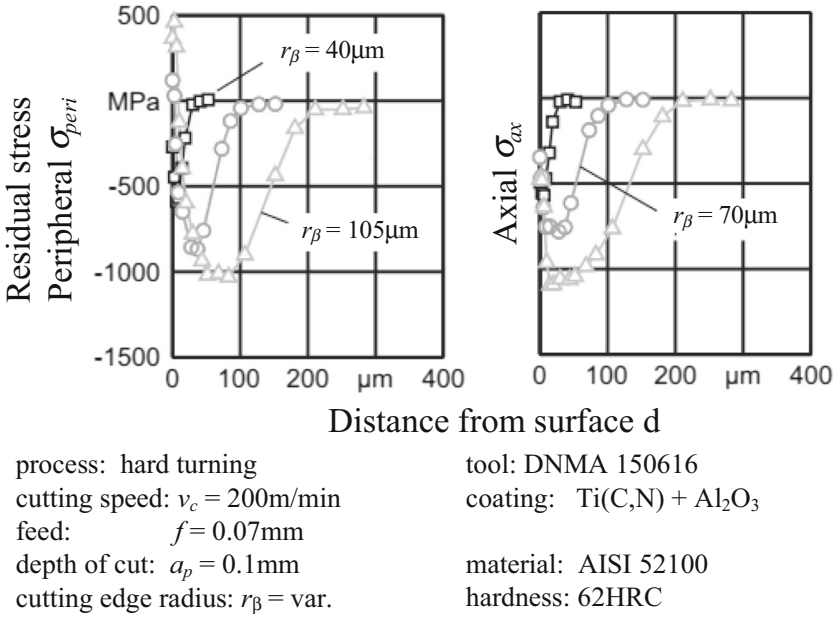

Fig. 57 Residual stress profiles in the peripheral and axial directions for different cutting edge radius after turning AISI 52100 at V_c = 200 m/min, f = 0.07 mm/rev, a_p = 0.1 mm [118]

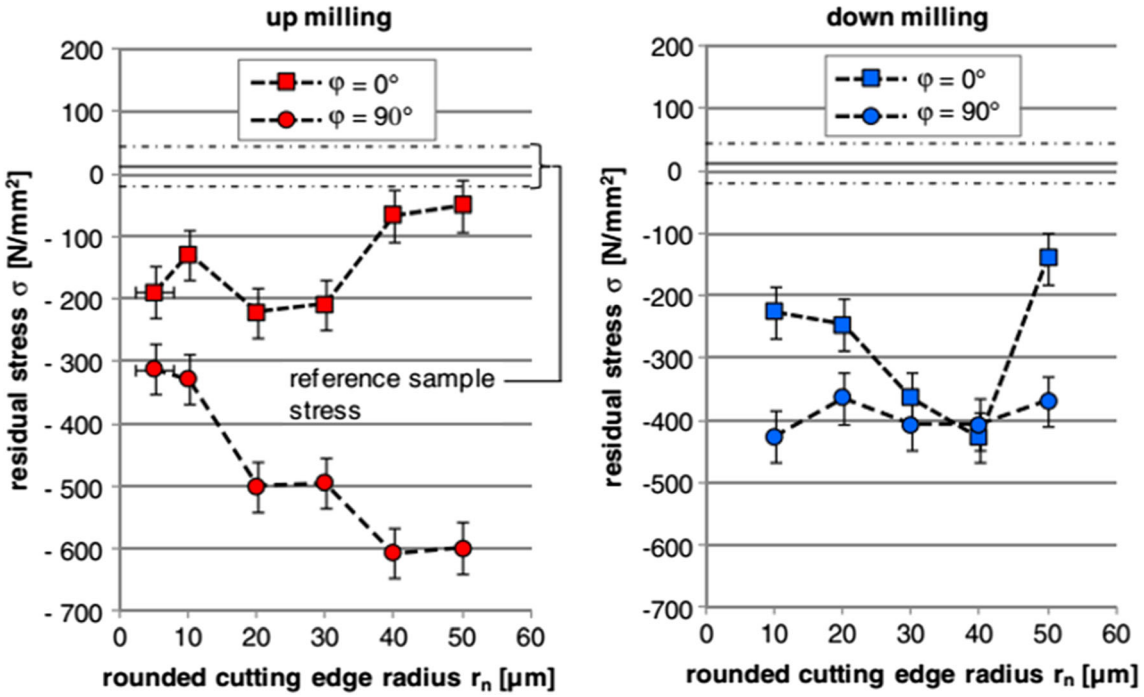

Fig. 58 Residual stress profiles for different cutting edge radius after milling Ti6Al4V at V_c = 70 m/min, f_z = 0.08 mm/rev, and $a_e = a_s$ = 25 mm [127]

residual stress was more compressive for type-3 insert with larger chamfer angle 30° when machining SAE 52100 steel at V_c = 200~225 m/min, f = 0.06~0.1 mm/rev, and a_p = 0.05~0.15 mm (see Fig. 66). Thiele et al. [134] found that large honed edge and chamfered edge tools produced more compressive residual stress in the hoop and axial directions than small honed edge tools for 57 HRC workpeice after turning AISI 52100. In addition, large honed edge tools result in deeper and more compressive residual stresses than small honed edge and chamfer edge, which is attributed to subsurface plastic flow. According to Arunachalam et al. [165], in the case of both dry and wet cutting, the sharp edge tools result in higher values of tensile residual stresses than the honed edge tools, while the chamfered edge generates compressive

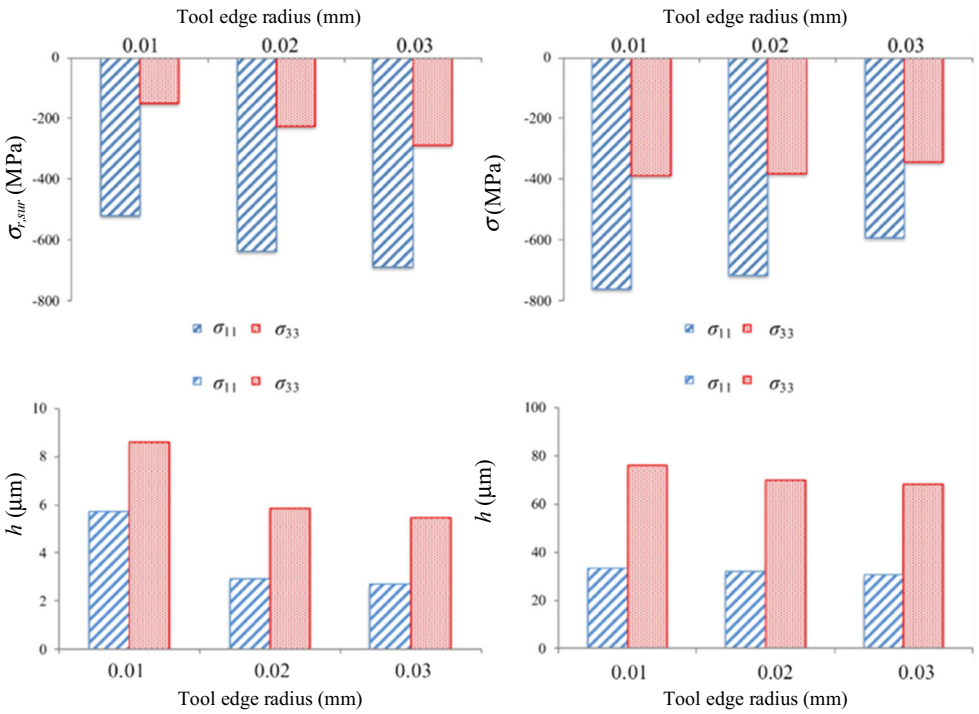

Fig. 59 Effect of tool edge radius on the surface and peak residual stress, the depth of maximum compressive stress, and the influencing range of machining induced residual stress after turning Ti6Al4V at V_c = 70 m/min, f = 0.01 mm, and a_p = 0.1 mm [166]

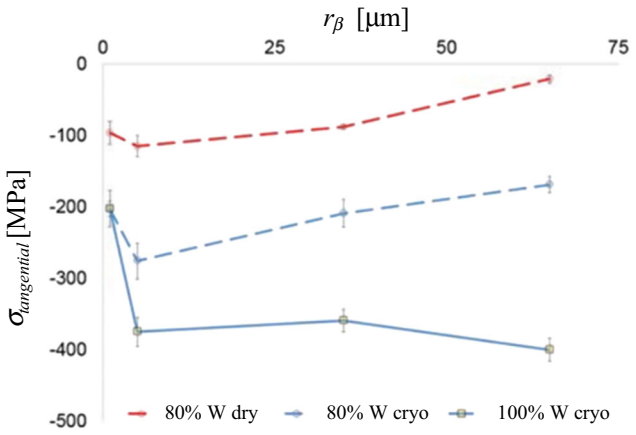

Fig. 60 tangential surface stress as a function of r_β for cryogenic machining of 80% porous (dashed blue line) and fully dense polycrystalline tungsten (solid blue line), and for dry machinning of 80% porous tungsten(dashend red line) at V_c = 20 m/min, f = 0.025 m/rev, and a_p = 0.075 mm [167]

residual stress when turning age hardened Inconel (see Fig. 67). These studies show that larger chamfer angle lead to more compressive residual stress and it performs better than the small honed tool and sharp tool.

In addition, some studies indicated that chamfer plus hone tools could obtain optimum residual stress profiles. Pawade et al. [157] concluded that the state of residual stress in the machined surface changed from tensile to compressive as the cutting edge changing from 30° chamfer angle to 20° chamfer angle and became more compressive with further change to a honed cutting edge after turning Inconel 718. Hua et al. [172] revealed that the maximum residual stress and the depth for a desired residual stress of 200 MPa increase with the edge radius after turning AISI 52100 at V_c = 120 m/min and f = 0.1 mm/rev, and the chamfer plus hone edge tool generates high values equivalent to the large hone tool. Varela et al. [14] focused on the effect of sharp, hone, and chamfer-hone edge tools on the machining induced residual stress when turning of 300M steel, which indicated that chamfer-hone edge tool produces compressive stresses at all cutting conditions, thus outperforms the chamfer only and hone only cutting tools. Shen et al. [173] investigated the effect of cutting edge microgeometry factors of average cutting edge radius $\bar{S}$, form-factor K, and different cutting edge type on residual stress in orthogonal cutting for Inconel 718 by FEM. Figure 68 reveals that the values of maximum compression residual stress and the surface tensile residual stress present an increasing trend with the increase of average cutting edge radius $\bar{S}$, and the maximum compression stress displays obvious growth by introducing chamfer to the cutting edge, which plays a similar role with a larger average cutting edge radius $\bar{S}$. It is suggested that the increased surface tensile residual stress is attributed to higher temperature gradient in the subsurface layer, which can be attributed to the increasing frictional contact length between cutting edge and workpiece and the deeper plastic deformation caused by larger ploughing depth. The increase of ploughing depth also indicated more material was squeezed, which contributes to the increase of maximum compression residual stress. In turning AISI D2 steel at V_c = 60~120 m/min, f = 0.05~0.16 m/min, and a_p = 0.1~0.35 mm, Sarnobat and Raval [159] found that standard honed edge tool (25° chamfer angle) produced highest values

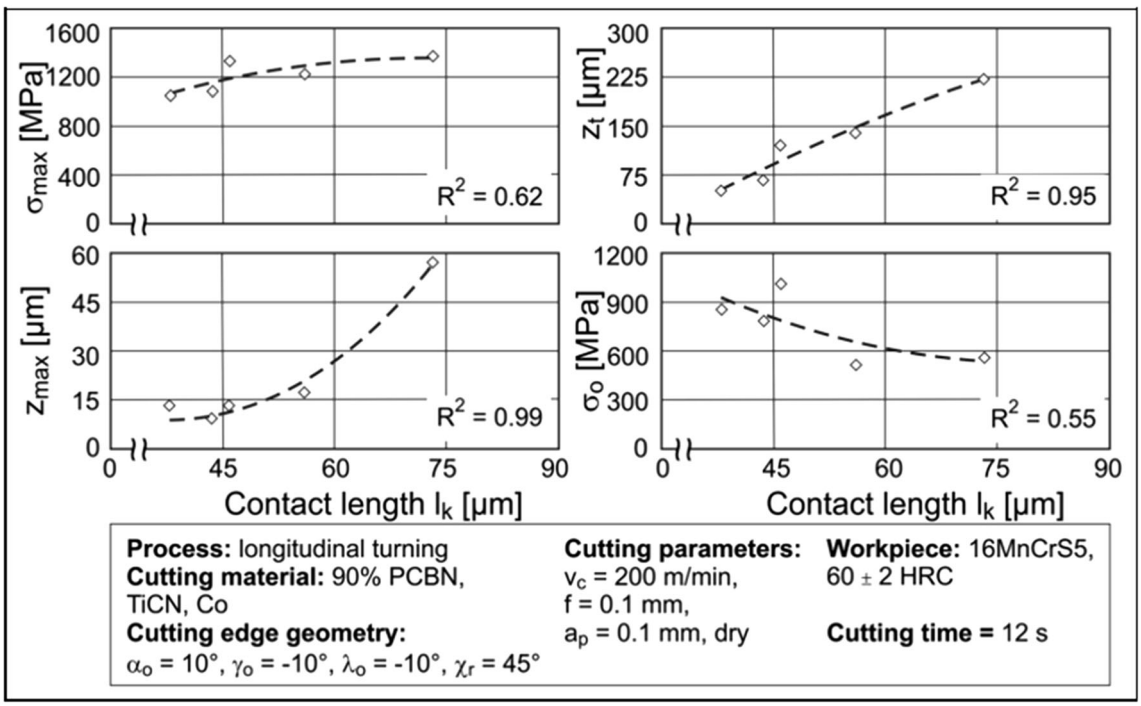

Fig. 61 Variations of residual stresses parameters after turning 16MnCrS5 with too-workpiece contact length [63]

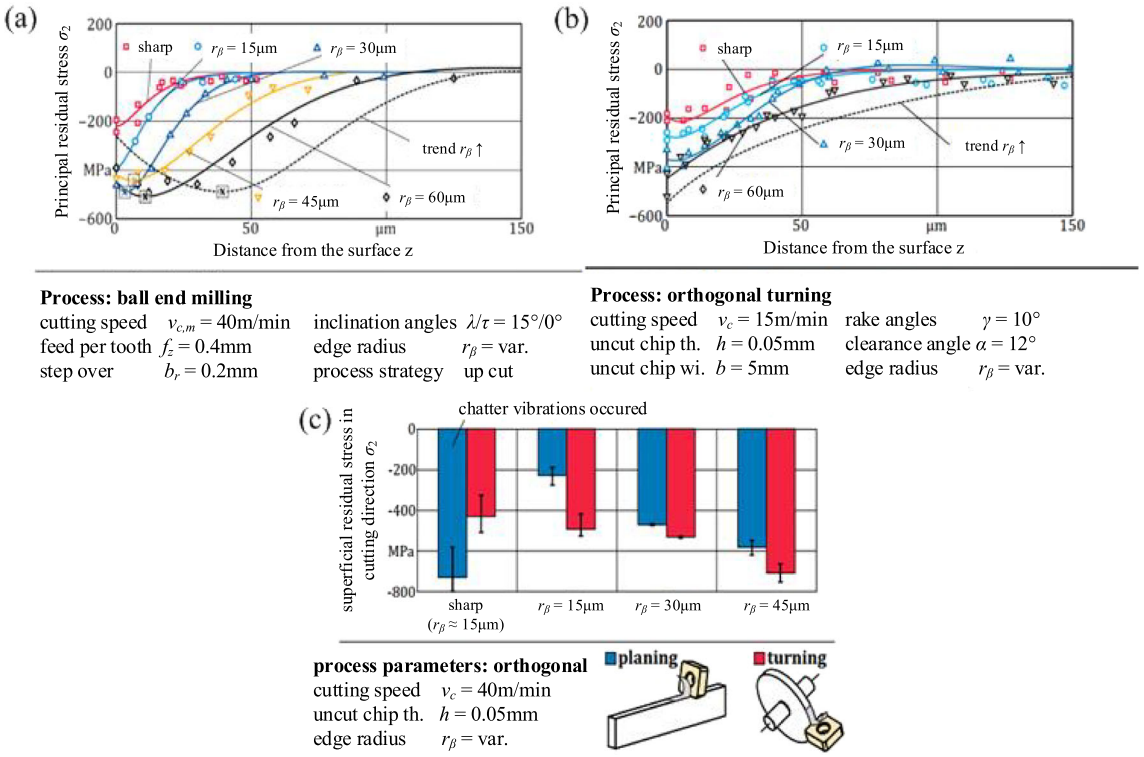

Fig. 62 Effect of edge radius on surface residual stress during **a** ball end milling, **b** orthogonal turning, and **c** orthogonal planing and turning processes [168]

of tensile residual stress both in the axial and circumferential directions, and the light honed edge tool (15° chamfer angle) lead to compressive stress in the radial direction.

6 Summary and outlook

Edge microgeometry is a key factor that makes difference to cutting phenomena in advanced manufacturing, covering material flow state, cutting mechanics, tool performance, and surface integrity. To address the role of different edge preparations in metal cutting, this review paper provides an overview in this research field from the aspect of machining-induced cutting phenomena, explaining this topic through theoretical modeling as well as discussing it based on experimental work. The major conclusions and future suggestions are given as follow:

- Subtractive manufacturing always represents a dominant role in industry due to its high productivity and the high quality of produced components. Researches in this field mainly focus on three aspects, that is, tool production, material removal processes, and surface integrity. Among all these issues, the optimization of tool edge microgeometries is still the challenge and requires more attention.
- Multiple types of cutting edge have been employed in manufacturing, for instance, rounded, general honed, chamfered, grooved, etc. The advantages of different types of cutting edge in specific cutting conditions have been reported by a lot of literature. Honed and chamfered tools are the main research object; further, the honed edge can be characterized by cutting edge segment on flank face and rake face while chamfered edge can be characterized by chamfer angle and chamfer length.
- Chip formation, as well as MUCT and DMZ in metal cutting when considering the presence of edge microgeometries can be revealed by slip-line fields. The contributions in modeling material separation for sharp, honed, and chamfered edge based on slip-line field theory are illustrated in Section 2.2. It can be concluded that the influence of edge microgeometries on cutting phenomena can be attributed to the various material flow state. An in-depth understanding of material flow state can help to understand how the edge microgeometries affect cutting mechanics, and further, tool performance and surface integrity.
- Several analytical or semi-analytical models have been proposed in previous literature for rounded or chamfered edge tools. Normally, a linear relation between edge radius and cutting force can be found in both turning and milling for different tool-workpiece couples. S_α is positive on force components while S_γ is negative, which can be

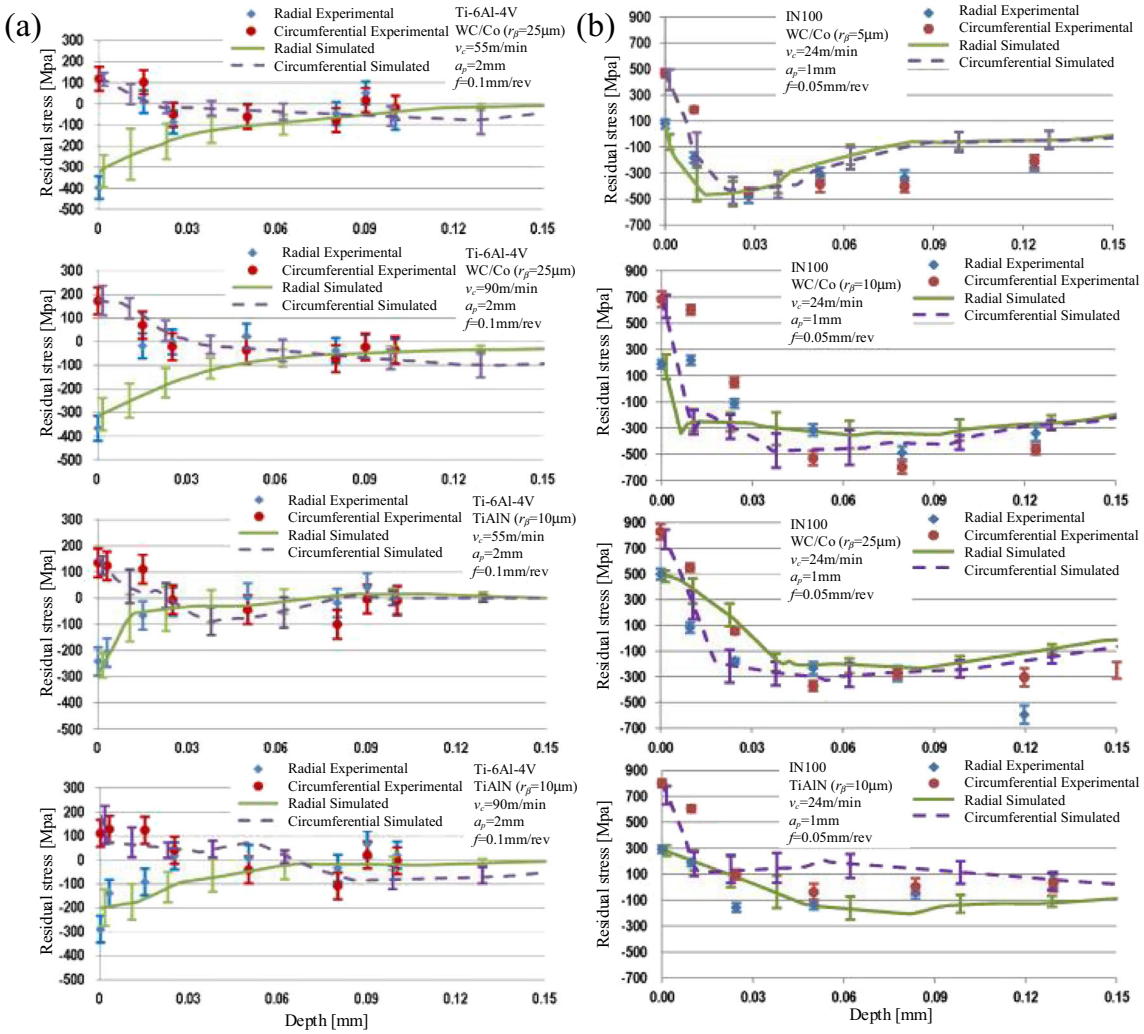

Fig. 63 Residual stress profiles in face turning of **a** Ti6Al4V at V_c = 55~90 m/min, f = 0.1 mm/rev, a_p = 2 mm and **b** IN 100 at V_c = 24 m/min, f = 0.05 mm/rev, a_p = 1 mm [169]

explained from the geometric analysis that a larger S_α will increase ploughing effect while a larger S_γ will lead to a more positive effective rake angle. Size effect will happen when UCT is much smaller than edge radius. Cutting force components will increase with increasing chamfer length and the trend could be linear or nonlinear.

- FEM and analytical method are major approaches for cutting temperature modeling. Simulation results indicate that temperature profile will be reduced if a $K < 1$ honed tool is employed; further, a chamfered tool will result in higher maximum temperature on rake face due to a more negative effective rake angle. From the aspect of analytical modeling, larger edge microgeometries produce higher temperature profile because the heat sources become larger and the heat intensity gets stronger.
- For rounded tools, the major agreement in tool wear is that it can be mitigated if a tool with larger edge radius is employed. For general honed tools, the influence of S_α and S_γ on tool wear is complicated and still a clear relation is missing. Variable and invariable chamfered edge tools show significantly different performance on crater wear and flank wear. Edge preparation techniques also make difference.
- Tool life can be greatly extended if a correct couple of edge parameters is chosen, whereas also can be reduced if an improbable combination of edge parameters is employed. The influence of different edge microgeometries on tool life is complicated and the major contributions in this issue are listed in Table 1, considering turning and milling operations.
- Most of the literature stated that a smoother surface can be obtained when employing tools with smaller edge radius. However, adverse effects will also happen if tool edge is sharp to a certain extent due to possible micro cracks. Honed edge tools with $K < 1$ can produce lower surface roughness. Feed rate is another indicator that can affect the effects of edge microgeometries on surface roughness, which indicates that edge geometries can be more

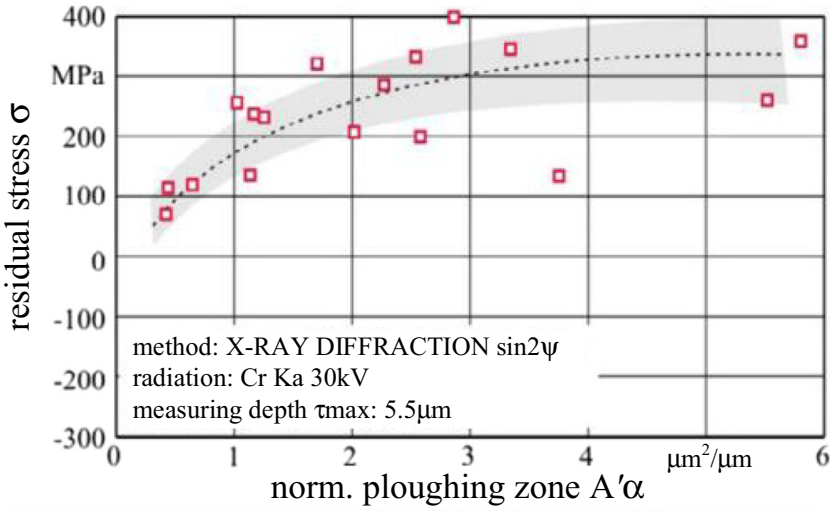

Fig. 64 Residual stress profiles for nomalized ploughing zone A ′α during slot milling of 42CrMo4-QT steel [109]

Tool:		**Process:**	
type:	ADGT 080308R	Cutting speed:	v_c = 230m/min
company:	Walter AG	Depth of cut:	a_p = 1.5mm
substrat:	cement carbide	Feed per tooth:	f_z = 0.2mm
coating:	TiAlN+Al_2O_3	Width of cut:	a_e = 25mm
diameter:	D = 25mm	cooling:	none
no. of teeth:	z = 1	material:	42CrMo4QT

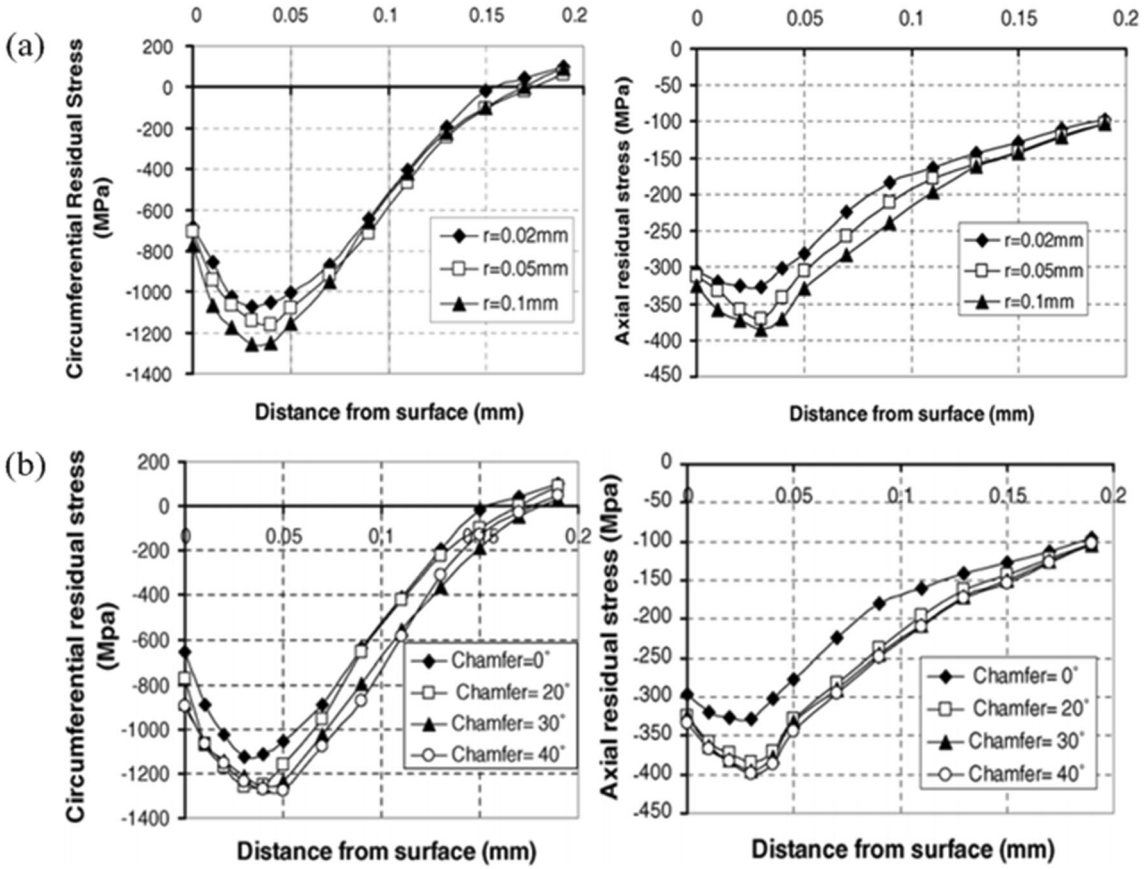

Fig. 65 Predicted circumferential and axial residual stress for different hone edges (**a**) and chamfer angles (**b**) when turning AISI 52100 at V_c = 120 m/min, f = 0.28 mm/rev, and a_p = 0.35 mm [90]

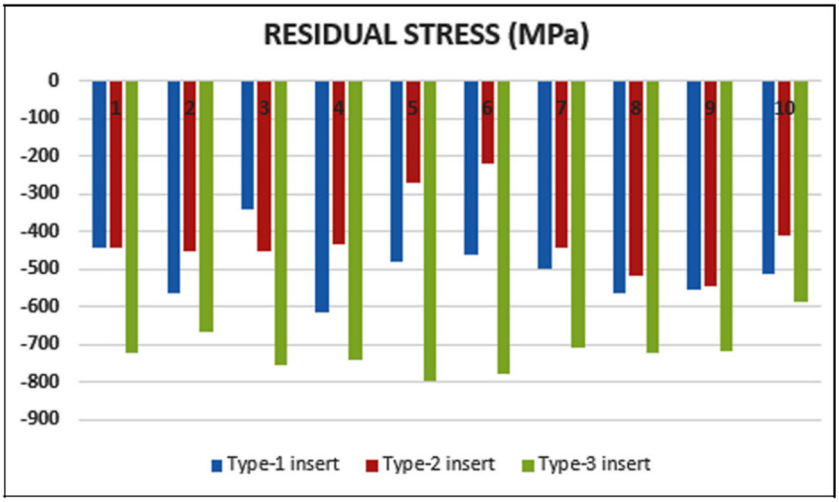

Fig. 66 Average circumferential residual stresses for the three types of inserts after machining SAE 52100 steel at V_c = 200~225 m/min, f = 0.06~0.1 mm/rev, and a_p = 0.05~0.15 mm [171]

important under the condition of low feed rate. Different edge preparation techniques also lead to surface roughness variation.

- When it comes to machining-induced microstructural alterations, it is widely recognized that the deformation of microstructure can be severer with the increasing edge radius due to ploughing effect. Moreover, some scholars claimed that white layer is more likely to be formed if a tool with larger honed edge is used. Similar trends can be observed when investigating grain refinement for that larger edge microgeometries resulting in severer plastic deformation.
- The effect of edge radius on microhardness in subsurface is commonly recognized that larger edge radius makes higher microhardness. This phenomenon is closely related to the microstructural alternations induced by different edge microgeometries. For chamfered edge tools, increasing chamfer angle and chamfer length results in higher microhardness improvement in subsurface, which can be explained that a more negative effective rake angle is formed and more significant ploughing effect happens. Some researchers also stated that chamfer plus hone edge tools can further increase the microhardness profile.
- On the one hand, residual stress profile can be more compressive with the growth of honed edge magnitude, which could be correlated with the higher passive forces. On the other hand, more compressive residual stresses can be obtained by employing tools with a larger chamfer angle. Usually, the performance of chamfered edge tools is better than sharp tools or tools with small hone. Additionally, chamfer plus hone edge tools outperform simply honed or chamfered tools in some cases.

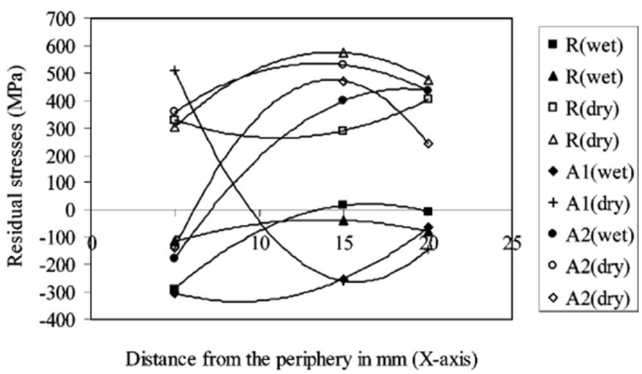

Fig. 67 Residual stress profiles for different cutting edge preparation (R-honed; A1-chamfered; A2-sharp) when turning age hardened Inconel 718 at V_c = 60 m/min, f = 0.1 mm/rev, and a_p = 0.5 mm [165]

Although numerous studies have been reported on the influence of edge microgeometries on cutting phenomena, there are still some questions remaining: (1) Effects of the surface quality of cutting edge (for instance, friction coefficient, surface roughness, residual stresses, etc.) on metal cutting have not been explored well; (2) the form-factor K defines the start and end points of edge while neglects the curvature of the connecting line; (3) although numerous slip-line models are proposed to describe the material flow state, the validation mainly focuses on the cutting force comparison. A more intuitive method for observing the material flow state at high deformation speed from the micro level is still missing; and (4) a comprehensive study on the collective effect of edge microgeometry and chip breaker is required because most of the commercial tools have a chip breaker.

Author contribution KZ: supervision, original idea, manuscript writing. CF: manuscript writing, data collection. JW: reviewing and editing. CH: manuscript writing, data collection.

Funding This work is partially supported by the National Natural Science Foundation of China (51705385, 51975237), and State Key Laboratory

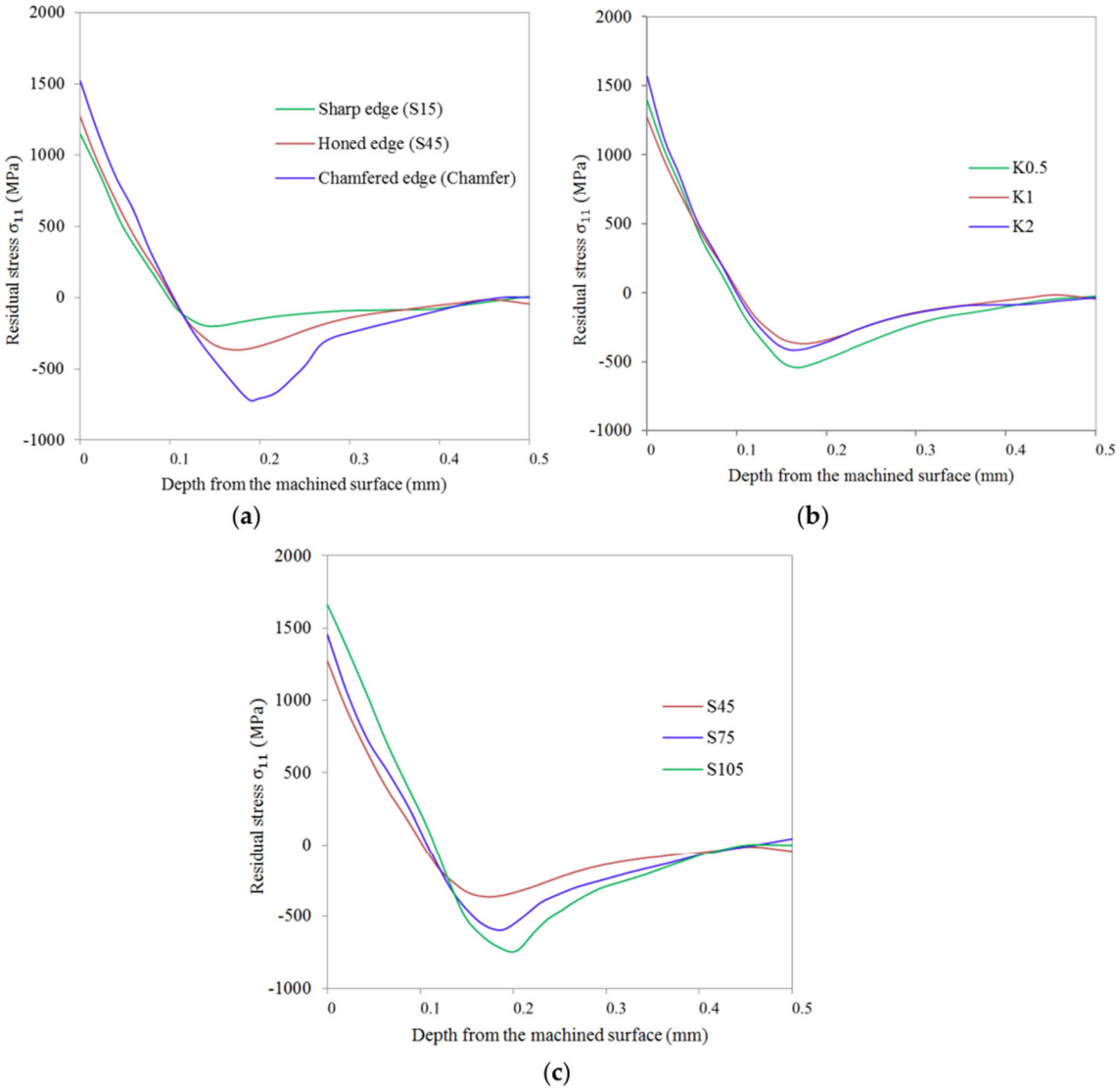

Fig 68. Residual stress profiles for machined Inconel 718 by FEM at $V_c = 29$ m/min and $a_p = 0.15$ mm, circumferential stress σ_{11} for **a** different cutting edge type, **b** form-factor K, and **c** average cutting edge radius $\bar{S}$ [173]

of Digital Manufacturing Equipment and Technology (DMETKF2020009, DMETKF2021005).

Data availability All data generated or analyzed during this study are included in this published article.

Declarations

Ethics approval Not applicable.

Consent to participate All the authors involved have agreed to participate in this submitted article.

Consent for publication All the authors involved in this manuscript give full consent for publication of this submitted article.

Competing interests The authors declare no competing interests.

References

1. Bobzin K (2017) High-performance coatings for cutting tools. CIRP J Manuf Sci Technol 18:1–9
2. Brinksmeier AE, Meyer AD, Heinzel AC, Lübben T, Slter AJ, Langenhorst AL, Frerichs AF, Kmmler AJ, Kohls AE, Kuschel AS (2018) Process signatures—the missing link to predict surface integrity in machining. Procedia CIRP 71:3–10
3. Brinksmeier E, Gläbe R, Klocke F, Lucca DA (2011) Process signatures—an alternative approach to predicting functional workpiece properties. Procedia Eng 19:44–52
4. Thakur A, Gangopadhyay S (2016) State-of-the-art in surface integrity in machining of nickel-based super alloys. Int J Mach Tools Manuf 100:25–54
5. Junge T, Liborius H, Mehner T, Nestler A, Schubert A, Lampke T (2020) Method for process monitoring of surface layer changes in turning of aluminium alloys using tools with a flank face chamfer. Procedia CIRP 87:432–437

6. Magalhães F, Ventura C, Abrão A, Denkena B (2020) Experimental and numerical analysis of hard turning with multi-chamfered cutting edges. J Manuf Process 49:126–134
7. Karpuschewski B, Schmidt K, Beňo J, Maňková I, Prilukova J (2014) Measuring procedures of cutting edge preparation when hard turning with coated ceramics tool inserts. Measurement 55: 627–640
8. Zhao T, Zhou JM, Bushlya V, Ståhl JE (2017) Effect of cutting edge radius on surface roughness and tool wear in hard turning of AISI 52100 steel. Int J Adv Manuf Technol 91(9):3611–3618
9. Hu C, Zhuang KJ, Weng J, Zhang XM (2019) Thermal-mechanical model for cutting with negative rake angle based on a modified slip-line field approach. Int J Mech Sci 164:105167
10. Yussefian NZ, Koshy P (2013) Parametric characterization of the geometry of honed cutting edges. Precis Eng 37(3):746–752
11. Benjamin B, Thilo G (2018) Basic principles for the design of cutting edge roundings. CIRP Ann Manuf Technol 67(1):73–78
12. Wan L, Wang D, Gao Y (2015) Investigations on the effects of different tool edge geometries in the finite element simulation of machining. Stroj Vestn-J Mech Eng 61(3):157–166
13. Mayer P, Kirsch B, Müller R, Becker S, Ev H, Aurich JC (2016) Influence of cutting edge geometry on deformation induced hardening when cryogenic turning of metastable austenitic stainless steel AISI 347. Procedia CIRP 45:59–62
14. Varela PI, Rakurty CS, Balaji AK (2014) Surface integrity in hard machining of 300M steel: effect of cutting-edge geometry on machining induced residual stresses. Procedia CIRP 13:288–293
15. Denkena B, Köhler J, Ventura CEH (2013) Customized cutting edge preparation by means of grinding. Precis Eng 37(3):590–598
16. Reilly GA, McCormack BAO, Taylor D (2004) Cutting sharpness measurement: a critical review. J Mater Process Technol 153-154: 261–267
17. Karpat Y, Özel T (2008) Mechanics of high speed cutting with curvilinear edge tools. Int J Mach Tool Manu 48(2):195–208
18. Denkena B, Biermann D (2014) Cutting edge geometries. CIRP Ann Manuf Technol 63(2):631–653
19. He GH, Liu XL, Wu CH, Zhang SQ, Zou LL, Li DJ (2016) Study on the negative chamfered edge and its influence on the indexable cutting insert ' s lifetime and its strengthening mechanism. Int J Adv Manuf Technol 84(5-8):1229–1237
20. Weng J, Zhuang KJ, Chen D, Guo SS, Ding H (2017) An analytical force prediction model for turning operation by round insert considering edge effect. Int J Mech Sci 128-129:168–180
21. Weng J, Zhuang KJ, Hu C, Ding H (2019) A PSO-based semi-analytical force prediction model for chamfered carbide tools considering different material flow state caused by edge geometry. Int J Mech Sci 169:105329
22. Ventura CEH, Koehler J, Denkena B (2015) Influence of cutting edge geometry on tool wear performance in interrupted hard turning. J Manuf Process 19:129–134
23. Merchant ME (1945) Mechanics of the metal cutting process I. orthogonal cutting and a type 2 chip. J Appl Phys 16(5):267–275
24. Lee E (1951) The theory of plasticity applied to a problem of machining. J Appl Phys 18:405
25. Shaw MC, Cook NH, Finnie I (1953) The shear angle relationship in metal cutting. Trans ASME 75:273–288
26. Oxley PLB, Welsh MJM (1967) An explanation of the apparent bridgman effect in Merchant ' s orthogonal cutting results. J Eng Ind 89(3):549–555
27. Zorev N (1958) Results of work in the field of the mechanics of the metal cutting process. In: Proceedings of Conference on Technology of Engineering Manufacture, pp 255–268
28. Toropov A, Ko S-L (2003) Prediction of tool-chip contact length using a new slip-line solution for orthogonal cutting. Int J Mach Tool Manu 43(12):1209–1215
29. Kudo H (1965) Some new slip-line solutions for two-dimensional steady-state machining. Int J Mech Sci 7(1):43–55
30. Dewhurst P (1978) Eigen-vector slip-line field solutions. In: Applications of Numerical Methods to Forming Processes, pp 121–127
31. Usui E (1981) Simulation analysis of built-up edge formation in machining of low carbon steel. Bull Jpn Soc Precis Eng 15:237–242
32. Fang N, Dewhurst P (2005) Slip-line modeling of built-up edge formation in machining. Int J Mech Sci 47(7):1079–1098
33. Ozturk S (2012) Slip-line modeling of machining and determine the influence of rake angle on the cutting force. Trans Can Soc Mech Eng 36(1):23–35
34. Basuray P, Misra B, Lal G (1977) Transition from ploughing to cutting during machining with blunt tools. Wear 43(3):341–349
35. Yuan Z, Zhou M, Dong S (1996) Effect of diamond tool sharpness on minimum cutting thickness and cutting surface integrity in ultraprecision machining. J Mater Process Technol 62(4):327–330
36. Kim C-J, Bono M, Ni J (2002) Experimental analysis of chip formation in micro-milling. Trans NAMRI/SME 30:247–254
37. Zhou TF, Wang Y, Ruan BS, Liang ZQ, Wang XB (2020) Modeling of the minimum cutting thickness in micro cutting with consideration of the friction around the cutting zone. Front Mech Eng-PRC 15(1):81–88
38. Abdelmoneim ME, Scrutton R (1974) Tool edge roundness and stable build-up formation in finish machining. J Eng Ind 96(4): 1258–1267
39. Wan M, Wen DY, Ma YC, Zhang WH (2019) On material separation and cutting force prediction in micro milling through involving the effect of dead metal zone. Int J Mach Tool Manu 146:103452
40. Waldorf DJ, DeVor RE, Kapoor SG (1998) A slip-line field for ploughing during orthogonal cutting. J Manuf Sci E T ASME 120(4):693–699
41. Fang N, Jawahir I (2003) Analytical prediction of the chip back-flow angle in machining with restricted contact grooved tools. J Manuf Sci E T ASME 125(2):210–219
42. Jin X, Altintas Y (2011) Slip-line field model of micro-cutting process with round tool edge effect. J Mater Process Technol 211(3):339–355
43. Ozturk S, Altan E (2012) A slip-line approach to the machining with rounded-edge tool. Int J Adv Manuf Technol 63(5-8):513–522
44. Zhang T, Liu Z, Shi Z, Xu C (2017) Investigation on size effect of specific cutting energy in mechanical micro-cutting. Int J Adv Manuf Technol 91(5-8):2621–2633
45. Zhang H, Liu P, Hu R (1991) A three-zone model and solution of shear angle in orthogonal machining. Wear 143(1):29–43
46. Ren H, Altintas Y (2000) Mechanics of machining with chamfered tools. J Manuf Sci E T ASME 122(4):650–659
47. Fang N, Wu Q (2005) The effects of chamfered and honed tool edge geometry in machining of three aluminum alloys. Int J Mach Tool Manu 45(10):1178–1187
48. Karpat Y, Özel T (2006) An integrated analytical thermal model for orthogonal cutting with chamfered tools. Transactions of the North American Manufacturing Research Institution of SME (Society of Manufacturing Engineers) 34:9–16
49. Kiyota H, Itoigawa F, Endo S, Nakamura T (2013) Analytical approach for optimization of chamfered cutting tool preparation considering built-up edge extrusion behavior. Int J Autom Technol 7(3):329–336
50. Hu C, Zhuang KJ, Weng J, Zhang XM, Ding H (2020) Cutting temperature prediction in negative-rake-angle machining with chamfered insert based on a modified slip-line field model. Int J Mech Sci 167:105273

51. Dai X, Zhuang KJ, Ding H (2019) A systemic investigation of tool edge geometries and cutting parameters on cutting forces in turning of Inconel 718. Int J Adv Manuf Technol 105(1-4):531–543
52. Altintas Y (2012) Manufacturing automation: metal cutting mechanics, machine tool vibrations, and CNC design. Cambridge university press
53. Albrecht P (1960) New developments in the theory of the metal-cutting process: part I—the ploughing process in metal cutting. J Eng Ind 82(4):348–357
54. Moufki A, Dudzinski D, Le Coz G (2015) Prediction of cutting forces from an analytical model of oblique cutting, application to peripheral milling of Ti-6Al-4V alloy. Int J Adv Manuf Technol 81(1-4):615–626
55. Gao P, Liang Z, Wang X, Li S, Zhou T (2018) Effects of different chamfered cutting edges of micro end mill on cutting performance. Int J Adv Manuf Technol 96(1-4):1215–1224
56. Liang SY, Su JC (2007) Residual stress modeling in orthogonal machining. CIRP Ann Manuf Technol 56(1):65–68
57. Zhang WQ, Wang XL, Hu YJ, Wang SY (2018) Predictive modelling of microstructure changes, micro-hardness and residual stress in machining of 304 austenitic stainless steel. Int J Mach Tool Manu 130-131:36–48
58. Wan M, Ye XY, Yang Y, Zhang WH (2017) Theoretical prediction of machining-induced residual stresses in three-dimensional oblique milling processes. Int J Mech Sci 133:426–437
59. Srinivasa YV, Shunmugam MS (2013) Mechanistic model for prediction of cutting forces in micro end-milling and experimental comparison. Int J Mach Tool Manu 67:18–27
60. Yuan YJ, Jing XB, Ehmann KF, Cao J, Li HZ, Zhang DW (2018) Modeling of cutting forces in micro end-milling. J Manuf Process 31(JAN):844–858
61. Weng J, Zhuang KJ, Zhu DH, Guo SS, Ding H (2018) An analytical model for the prediction of force distribution of round insert considering edge effect and size effect. Int J Mech Sci 138-139: 86–98
62. Wyen CF, Wegener K (2010) Influence of cutting edge radius on cutting forces in machining titanium. CIRP Ann Manuf Technol 59(1):93–96
63. Ventura CEH, Breidenstein B, Denkena B (2018) Influence of customized cutting edge geometries on the workpiece residual stress in hard turning. Proc Inst Mech Eng B J Eng 232(12): 2132–2139
64. Ranganath S, Campbell AB, Gorkiewicz DW (2007) A model to calibrate and predict forces in machining with honed cutting tools or inserts. Int J Mach Tool Manu 47(5):820–840
65. Kalyan C, Samuel GL (2015) Cutting mode analysis in high speed finish turning of AlMgSi alloy using edge chamfered PCD tools. J Mater Process Technol 216:146–159
66. Zhou L, Peng FY, Yan R, Yao PF, Yang CC, Li B (2015) Analytical modeling and experimental validation of micro end-milling cutting forces considering edge radius and material strengthening effects. Int J Mach Tool Manu 97:29–41
67. Li B, Zhang S, Yan Z, Jiang D (2018) Influence of edge hone radius on cutting forces, surface integrity, and surface oxidation in hard milling of AISI H13 steel. Int J Adv Manuf Technol 95(1-4): 1153–1164
68. Padmakumar M (2020) Effect of cutting edge form factor (K-factor) on the performance of a face milling tool. CIRP J Manuf Sci Technol 31:305–313
69. Bassett E, KöHler J, Denkena B (2012) On the honed cutting edge and its side effects during orthogonal turning operations of AISI1045 with coated WC-Co inserts. CIRP J Manuf Sci Technol 5(2):108–126
70. Denkena B, Köhler J, Breidenstein B, Abrão AM, Ventura CEH (2014) Influence of the cutting edge preparation method on characteristics and performance of PVD coated carbide inserts in hard turning. Surf Coat Technol 254:447–454
71. Tomoiagă V-B, Popa MS, Sattel S, Conțiu G, Vereş OV, Bozga M, Slătineanu L, Merticaru V, Mihalache AM, Dodun O (2018) Influence of the cutting edge microgeometry in drilling operation of 42CrMo4 and X5CrNi18-10. MATEC Web of Conferences 178:01011
72. Gutnichenko O, Bushlya V, Zhou JM, Ståhl JE (2017) Tool wear and machining dynamics when turning high chromium white cast iron with pcBN tools. Wear 390:258–269
73. Zhuang KJ, Weng J, Zhu DH, Ding H (2018) Analytical modeling and experimental validation of cutting forces considering edge effects and size effects with round chamfered ceramic tools. J Manuf Sci E T ASME 140(8):081012
74. Weng J, Zhuang KJ, Zhou JM, Ding H (2020) A hybrid model for force prediction in orthogonal cutting with chamfered tools considering size and edge effect. Int J Adv Manuf Technol 110(11): 1367–1384
75. Liu Y, Xu DD, Agmell M, Saoubi RM, Zhou JM (2021) Numerical and experimental investigation of tool geometry effect on residual stresses in orthogonal machining of Inconel 718. Simul Model Pract Theory 106:102187
76. Yang Y, Zhu WW (2014) Study on cutting temperature during milling of titanium alloy based on FEM and experiment. Int J Adv Manuf Technol 73(9):1511–1521
77. He HB, Li HY, Yang J, Zhang XY, Yue QB, Jiang X, Lyu SK (2017) A study on major factors influencing dry cutting temperature of AISI 304 stainless steel. Int J Precis Eng Manuf 18(10): 1387–1392
78. Liu GL, Huang CZ, Su R, Özel T, Liu Y, Xu LH (2019) 3D FEM simulation of the turning process of stainless steel 17-4PH with differently texturized cutting tools. Int J Mech Sci 155:417–429
79. Qi ZX, Li B, Xiong LS (2014) An improved algorithm for McDowell ' s analytical model of residual stress. Front Mech Eng-PRC 9(2):150–155
80. Grzesik W (2006) Determination of temperature distribution in the cutting zone using hybrid analytical-FEM technique. Int J Mach Tool Manu 46(6):651–658
81. Fuat K, Kubilay A, Adem Ç (2016) Prediction of cutting temperature in orthogonal machining of AISI 316L using artificial neural network. Appl Soft Comput 38:64–74
82. Özel T (2009) Computational modelling of 3D turning: influence of edge micro-geometry on forces, stresses, friction and tool wear in PcBN tooling. J Mater Process Technol 209(11):5167–5177
83. Segebade E, Kümmel D, Zanger F, Schneider J, Schulze V (2018) Influence of cutting edge asymmetry on grain refinement of Ti6Al4V. Procedia CIRP 71:232–237
84. Komanduri R, Hou ZB (2000) Thermal modeling of the metal cutting process: Part I—Temperature rise distribution due to shear plane heat source. Int J Mech Sci 42(9):1715–1752
85. Komanduri R, Hou ZB (2001) Thermal modeling of the metal cutting process—Part II: temperature rise distribution due to frictional heat source at the tool–chip interface. Int J Mech Sci 43(1): 57–88
86. Huang Y, Liang SY (2003) Modelling of the cutting temperature distribution under the tool flank wear effect. Proc Inst Mech Eng C J Mech Eng Sci 217(11):1195–1208
87. Huang XD, Zhang XM, Ding H (2016) A novel relaxation-free analytical method for prediction of residual stress induced by mechanical load during orthogonal machining. Int J Mech Sci 115-116:299–309
88. Yi K, Tr Ö (2008) Analytical and thermal modeling of high-speed machining with chamfered tools. J Manuf Sci E T ASME 130(1): 119–129

89. Karpat Y, Özel T (2008) Analytical and thermal modeling of high-speed machining with chamfered tools. J Manuf Sci Eng 130(1): 011001
90. Hua J, Shivpuri R, Cheng X, Bedekar V, Matsumoto Y, Hashimoto F, Watkins TR (2005) Effect of feed rate, workpiece hardness and cutting edge on subsurface residual stress in the hard turning of bearing steel using chamfer+hone cutting edge geometry. Mater Sci Eng A MAT SCI ENG A-STRUC 394(1-2):238–248
91. Klocke F, Brinksmeier E, Weinert K (2005) Capability profile of hard cutting and grinding processes. CIRP Ann 54(2):22–45
92. Tiffe M, Aßmuth R, Saelzer J, Biermann D (2019) Investigation on cutting edge preparation and FEM assisted optimization of the cutting edge micro shape for machining of nickel-base alloy. Prod Eng 13(3):459–467
93. Bassett E (2013) Belastungsspezifische auslegung und herstellung von schneidkanten für drehwerkzeuge. (PhD-Thesis) Leibniz Universita¨ t, Hannover
94. Fu XS, Zou B, Liu YN, Huang CZ, Yao P (2019) Edge micro-creation of Ti(C, N) cermet inserts by micro-abrasive blasting process and its tool performance. Mach Sci Technol 23(6):951–970
95. Zhou JM, Walter H, Andersson M, Stahl JE (2003) Effect of chamfer angle on wear of PCBN cutting tool. Int J Mach Tool Manu 43(3):301–305
96. Chen T, Song LX, Li SY, Liu XL (2019) Experimental study on wear characteristics of PCBN tool with variable chamfered edge. Chin J Mech Eng-EN 32(1):37
97. Wang W, Saifullah MK, Aßmuth R, Biermann D, Arif A, Veldhuis S (2020) Effect of edge preparation technologies on cutting edge properties and tool performance. Int J Adv Manuf Technol 106(5-6):1823–1838
98. Bouzakis KD, Michailidis N, Skordaris G, Kombogiannis S, Hadjiyiannis S, Efstathiou K, Erkens G, Rambadt S, Wirth I (2002) Effect of the cutting edge radius and its manufacturing procedure, on the milling performance of PVD coated cemented carbide inserts. CIRP Ann Manuf Technol 51(1):61–64
99. Zhang S, Zou B, Liu Y, Wang Y, Huang C, Liu Z (2018) Edge passivation and quality of carbide cutting inserts treated by wet micro-abrasive blasting. Int J Adv Manuf Technol 96(5-8):2307–2318
100. Chen T, Li SY, Han BX, Liu GJ (2014) Study on cutting force and surface micro-topography of hard turning of GCr15 steel. Int J Adv Manuf Technol 72(9-12):1639–1645
101. Davoudinejad A, Noordin MY (2014) Effect of cutting edge preparation on tool performance in hard-turning of DF-3 tool steel with ceramic tools. J Mech Sci Technol 28(11):4727–4736
102. Denkena B, Lucas A, Bassett E (2011) Effects of the cutting edge microgeometry on tool wear and its thermo-mechanical load. CIRP Ann Manuf Technol 60(1):73–76
103. Özel T, Karpat Y, Srivastava A (2008) Hard turning with variable micro-geometry PcBN tools. CIRP Ann Manuf Technol 57(1): 73–76
104. Varghese A, Maurya PK, Kulkarni V, Joshi SS (2018) Experimental investigation of the correlation between surface roughness and tool-life in micromilling. Adv Mater Process Technol 5(1):67–77
105. Gao P, Wang XB, Liang ZQ, Xiang JF, Xie JQ (2019) Effects of WC grain size and Co content on microscale wear behavior of micro end mills in aluminum alloy 7075 machining. Int J Adv Manuf Technol 104(11-12):2401–2413
106. Bozga MB, Popa MS, Sattel S, Tomoiag VB (2017) Influence of the cutting edge microgeometry on the tool life in austenitic stainless steel machining with carbide end mill. MATEC Web Conf 112:01016
107. Fulemová J, Řehoř J (2015) Influence of form factor of the cutting edge on tool life during finishing milling. Procedia Eng 100:682–688
108. Zetek M, Lvana E, Vojtěch V (2014) Increasing cutting tool life when machining Inconel 718. Procedia Eng 69:1115–1124
109. Denkena B, Koehler J, Rehe M (2012) Influence of the honed cutting edge on tool wear and surface integrity in slot milling of 42CrMo4 steel. Procedia CIRP 1:190–195
110. Cheung FY, Zhou ZF, Geddam A, Li KY (2008) Cutting edge preparation using magnetic polishing and its influence on the performance of high-speed steel drills. J Mater Process Technol 208(1-3):196–204
111. Liang XL, Liu ZQ, Wang B (2019) State-of-the-art of surface integrity induced by tool wear effects in machining process of titanium and nickel alloys: a review. Measurement 132:150–181
112. Ventura CE, Chaves HS, Rubio JCC, Abrão AM, Denkena B, Breidenstein B (2017) The influence of the cutting tool microgeometry on the machinability of hardened AISI 4140 steel. Int J Adv Manuf Technol 90(9):2557–2565
113. Özel T, Hsu TK, Zeren E (2005) Effects of cutting edge geometry, workpiece hardness, feed rate and cutting speed on surface roughness and forces in finish turning of hardened AISI H13 steel. Int J Adv Manuf Technol 25(3-4):262–269
114. Burhanuddin Y, Che Haron CH, Ghani JA (2011) The effect of tool edge geometry on tool performance and surface integrity in turning Ti-6Al-4V alloys. Adv Mater Res 264-265:1211–1221
115. Thiele JD, Melkote SN (1999) Effect of cutting edge geometry and workpiece hardness on surface generation in the finish hard turning of AISI 52100 steel. J Mater Process Technol 94(2–3): 216–226
116. Zhao T, Agmell M, Persson J, Bushlya V, Ståhl JE, Zhou JM (2017) Correlation between edge radius of the cBN cutting tool and surface quality in hard turning. J Superhard Mater 39(4):251–258
117. Maiss O, Grove T, Denkena B (2017) Influence of asymmetric cutting edge roundings on surface topography. Prod Eng 11(4-5): 383–388
118. Denkena B, Grove T, Maiss O (2015) Influence of the cutting edge radius on surface integrity in hard turning of roller bearing inner rings. Prod Eng 9(3):299–305
119. Karpat Y (2019) Influence of diamond tool chamfer angle on surface integrity in ultra-precision turning of singe crystal silicon. Int J Adv Manuf Technol 101(5):1565–1572
120. Khan SA, Umar M, Saleem MQ, Mufti NA, Raza SF (2018) Experimental investigations on wiper inserts' edge preparation, workpiece hardness and operating parameters in hard turning of AISI D2 steel. J Manuf Process 34:187–196
121. Coelho R, Silva L, Braghini A, Bezerra A (2004) Some effects of cutting edge preparation and geometric modifications when turning Inconel 718™ at high cutting speeds. J Mater Process Technol 148(1):147–153
122. Han J, Hao X, Li L, Wu Q, He N (2017) Milling of high volume fraction SiCp/Al composites using PCD tools with different structures of tool edges and grain sizes. Int J Adv Manuf Technol 92(5-8):1875–1882
123. Zhou JM, Bushlya V, Peng RL, Johansson S, Avdovic P, Stahl JE (2011) Effects of tool wear on subsurface deformation of nickel-based superalloy. Procedia Eng 19:407–413
124. Bushlya V, Zhou JM, Ståhl JE (2012) Effect of cutting conditions on machinability of superalloy Inconel 718 during high speed turning with coated and uncoated PCBN tools. Procedia CIRP 3: 370–375
125. Thiele JD, Melkote SN (2000) Effect of tool edge geometry on workpiece subsurface deformation and through-thickness residual stresses for hard turning of AISI 52100 steel. J Manuf Process 2(4):270–276

126. Li BX, Zhang S, Fang YJ (2019) Effect of edge hone radius on plowing-induced plastic deformation in hard milling: analytical modeling and experimental validation. Int J Adv Manuf Technol 105(7-8):3017–3029
127. Wyen C-F, Jaeger D, Wegener K (2012) Influence of cutting edge radius on surface integrity and burr formation in milling titanium. Int J Adv Manuf Technol 67(1-4):589–599
128. Bordin FM, Zeilmann RP (2014) Effect of the cutting edge preparation on the surface integrity after dry drilling. Procedia CIRP 13:103–107
129. Zeilmann RP, Ost CA, Fontanive F (2018) Characterization of edge preparation processes and the impact on surface integrity after milling of AISI P20 steel. J Braz Soc Mech Sci 40(9):421
130. Ulutan D, Ozel T (2011) Machining induced surface integrity in titanium and nickel alloys: A review. Int J Mach Tool Manu 51(3): 250–280
131. Yin QG, Liu ZQ, Wang B, Song QH, Cai YK (2020) Recent progress of machinability and surface integrity for mechanical machining Inconel 718: a review. Int J Adv Manuf Technol 109(1-2):215–245
132. Zhang XM, Chen L, Ding H (2016) Effects of process parameters on white layer formation and morphology in hard turning of AISI 52100 steel. J Manuf Sci E T ASME 138(7):074502
133. Zhang XM, Huang XD, Chen L, Leopold J, Ding H (2017) Effects of sequential cuts on white layer formation and retained austenite content in hard turning of AISI 52100 steel. J Manuf Sci E T ASME 139(6):064502
134. Thiele JD, Melkote SN, Peascoe RA, Watkins TR (2000) Effect of cutting-edge geometry and workpiece hardness on surface residual stresses in finish hard turning of AISI 52100 steel. J Manuf Sci E T ASME 122(4):642–649
135. Bashir K, Alkali AU, Elmunafi MHS, Yusof NM (2018) Experimental investigation into effect of cutting parameters on surface integrity of hardened tool steel. IOP Conf Ser: Mater Sci Eng 344:012020
136. Zhang WW, Zhuang KJ (2020) Effect of cutting edge microgeometry on surface roughness and white layer in turning AISI 52100 steel. Procedia CIRP 87:53–58
137. Ren XP, Liu ZQ (2018) Microstructure refinement and work hardening in a machined surface layer induced by turning Inconel 718 super alloy. Int J Miner Metall Mater 25(8):937–949
138. Thakur DG, Ramamoorthy B, Vijayaraghavan L (2009) Study on the machinability characteristics of superalloy Inconel 718 during high speed turning. Mater Des 30(5):1718–1725
139. Umbrello D (2013) Investigation of surface integrity in dry machining of Inconel 718. Int J Adv Manuf Technol 69(9-12):2183–2190
140. Xu X, Zhang J, Outeiro J, Xu BB, Zhao WH (2020) Multiscale simulation of grain refinement induced by dynamic recrystallization of Ti6Al4V alloy during high speed machining. J Mater Process Technol 286:116834
141. Zheng GM, Cheng X, Dong YJ, Liu HB, Yu YZ (2020) Surface integrity evaluation of high-strength steel with a TiCN-NbC composite coated tool by dry milling. Measurement 166:108204
142. Hughes JI, Sharman ARC, Ridgway K (2006) The effect of cutting tool material and edge geometry on tool life and workpiece surface integrity. Proc Inst Mech Eng B J Eng 220(2):93–107
143. Rotella G, Dillon OW, Umbrello D, Settineri L, Jawahir IS (2013) The effects of cooling conditions on surface integrity in machining of Ti6Al4V alloy. Int J Adv Manuf Technol 71(1-4):47–55
144. Wang B, Liu ZQ (2018) Influences of tool structure, tool material and tool wear on machined surface integrity during turning and milling of titanium and nickel alloys: a review. Int J Adv Manuf Technol 98(5-8):1925–1975
145. Arisoy YM, Özel T (2015) Prediction of machining induced microstructure in Ti–6Al–4V alloy using 3-D FE-based simulations: effects of tool micro-geometry, coating and cutting conditions. J Mater Process Technol 220:1–26
146. Jafarian F, Umbrello D, Jabbaripour B (2016) Identification of new material model for machining simulation of Inconel 718 alloy and the effect of tool edge geometry on microstructure changes. Simul Model Pract Theory 66:273–284
147. Gerstenmeyer M, Ort B-L, Zanger F, Schulze V (2017) Influence of the cutting edge microgeometry on the surface integrity during mechanical surface modification by complementary machining. Procedia CIRP 58:55–60
148. Segebade E, Zanger F, Schulze V (2016) Influence of different asymmetrical cutting edge microgeometries on surface integrity. Procedia CIRP 45:11–14
149. Dai X, Zhuang KJ, Pu DL, Zhang WW, Ding H (2020) An investigation of the work hardening behavior in interrupted cutting Inconel 718 under cryogenic conditions. Materials 13(9):2202
150. Hua Y, Liu ZQ (2018) Effects of cutting parameters and tool nose radius on surface roughness and work hardening during dry turning Inconel 718. Int J Adv Manuf Technol 96(5-8):2421–2430
151. Khan SA, Ahmad MA, Saleem MQ, Ghulam Z, Qureshi MAM (2016) High-feed turning of AISI D2 tool steel using multi-radii tool inserts: Tool life, material removed, and workpiece surface integrity evaluation. Mater Manuf Process 32(6):670–677
152. Montazeri S, Aramesh M, Veldhuis SC (2018) An investigation of the effect of a new tool treatment technique on the machinability of Inconel 718 during the turning process. Int J Adv Manuf Technol 100(1-4):37–54
153. Arısoy YM, Guo C, Kaftanoğlu B, Özel T (2016) Investigations on microstructural changes in machining of Inconel 100 alloy using face turning experiments and 3D finite element simulations. Int J Mech Sci 107:80–92
154. Zhang PR, Liu ZQ (2015) Effect of sequential turning and burnishing on the surface integrity of Cr–Ni-based stainless steel formed by laser cladding process. Surf Coat Technol 276:327–335
155. Hotz H, Kirsch B (2020) Influence of tool properties on thermomechanical load and surface morphology when cryogenically turning metastable austenitic steel AISI 347. J Manuf Process 52:120–131
156. Zhuang KJ, Hu C, Zhou JM, Peng RL (2020) Investigation on work hardening phenomenon in turning Inconel 718 with chamfered inserts considering thermal-mechanical loads. Procedia CIRP 87:47–52
157. Pawade RS, Joshi SS, Brahmankar PK (2008) Effect of machining parameters and cutting edge geometry on surface integrity of high-speed turned Inconel 718. Int J Mach Tool Manu 48(1):15–28
158. Kundrak J, Mamalis AG, Gyani K, Bana V (2010) Surface layer microhardness changes with high-speed turning of hardened steels. Int J Adv Manuf Technol 53(1-4):105–112
159. Sarnobat SS, Raval HK (2019) Experimental investigation and analysis of the influence of tool edge geometry and work piece hardness on surface residual stresses, surface roughness and work-hardening in hard turning of AISI D2 steel. Measurement 131: 235–260
160. Kurniawan D, Yusof NM, Sharif S (2010) Hard machining of stainless steel using wiper coated carbide: tool life and surface integrity. Mater Manuf Process 25(6):370–377
161. Bai W, Bisht A, Roy A, Suwas S, Sun R, Silberschmidt VV (2018) Improvements of machinability of aerospace-grade Inconel alloys with ultrasonically assisted hybrid machining. Int J Adv Manuf Technol 101(5-8):1143–1156
162. Agic A, Eynian M, Ståhl JE, Beno T (2018) Dynamic effects on cutting forces with highly positive versus highly negative cutting edge geometries. Int J Interact Des Manuf 13(2):557–565
163. Chen L, El-Wardany TI, Harris WC (2004) Modelling the effects of flank wear land and chip formation on residual stresses. CIRP Ann Manuf Technol 53(1):95–98

164. Huang ZY, He SJ, Zhuang KJ, Zhang XM, Ding H (2016) An analysis of cutting parameters, coated materials and nose radii on residual stresses when turning Inconel 718. Procedia CIRP 46: 368–371
165. Arunachalam RM, Mannan MA, Spowage AC (2004) Surface integrity when machining age hardened Inconel 718 with coated carbide cutting tools. Int J Mach Tool Manu 44(14):1481–1491
166. Yang D, Xiao X, Liang XL (2019) Analytical modeling of residual stress in orthogonal cutting considering tool edge radius effect. Int J Adv Manuf Technol 103(5-8):2965–2976
167. Schoop J, Ambrosy F, Zanger F, Schulze V, Jawahir IS, Balk TJ (2015) Increased surface integrity in porous tungsten from cryogenic machining with cermet cutting tool. Mater Manuf Process 31(7):823–831
168. Nespor D, Denkena B, Grove T, Böß V (2015) Differences and similarities between the induced residual stresses after ball end milling and orthogonal cutting of Ti–6Al–4V. J Mater Process Technol 226:15–24
169. Özel T, Ulutan D (2012) Prediction of machining induced residual stresses in turning of titanium and nickel based alloys with experiments and finite element simulations. CIRP Ann Manuf Technol 61(1):547–550
170. Guddat J, M ' Saoubi R, Alm P, Meyer D (2011) Hard turning of AISI 52100 using PCBN wiper geometry inserts and the resulting surface integrity. Procedia Eng 19:118–124
171. Paschoalinoto NW, Bordinassi EC, Bortolussi R, Leonardi F, Delijaicov S (2020) The effect of process parameters and cutting tool shape on residual stress of SAE 52100 hard turned steel by high speed machining. Proc Inst Mech Eng B J Eng 235(1-2):290–300
172. Hua J, Umbrello D, Shivpuri R (2006) Investigation of cutting conditions and cutting edge preparations for enhanced compressive subsurface residual stress in the hard turning of bearing steel. J Mater Process Technol 171(2):180–187
173. Shen Q, Liu ZQ, Hua Y, Zhao JF, Lv WY, Mohsan A (2018) Effects of cutting edge microgeometry on residual stress in orthogonal cutting of Inconel 718 by FEM. Materials 11(6):1015